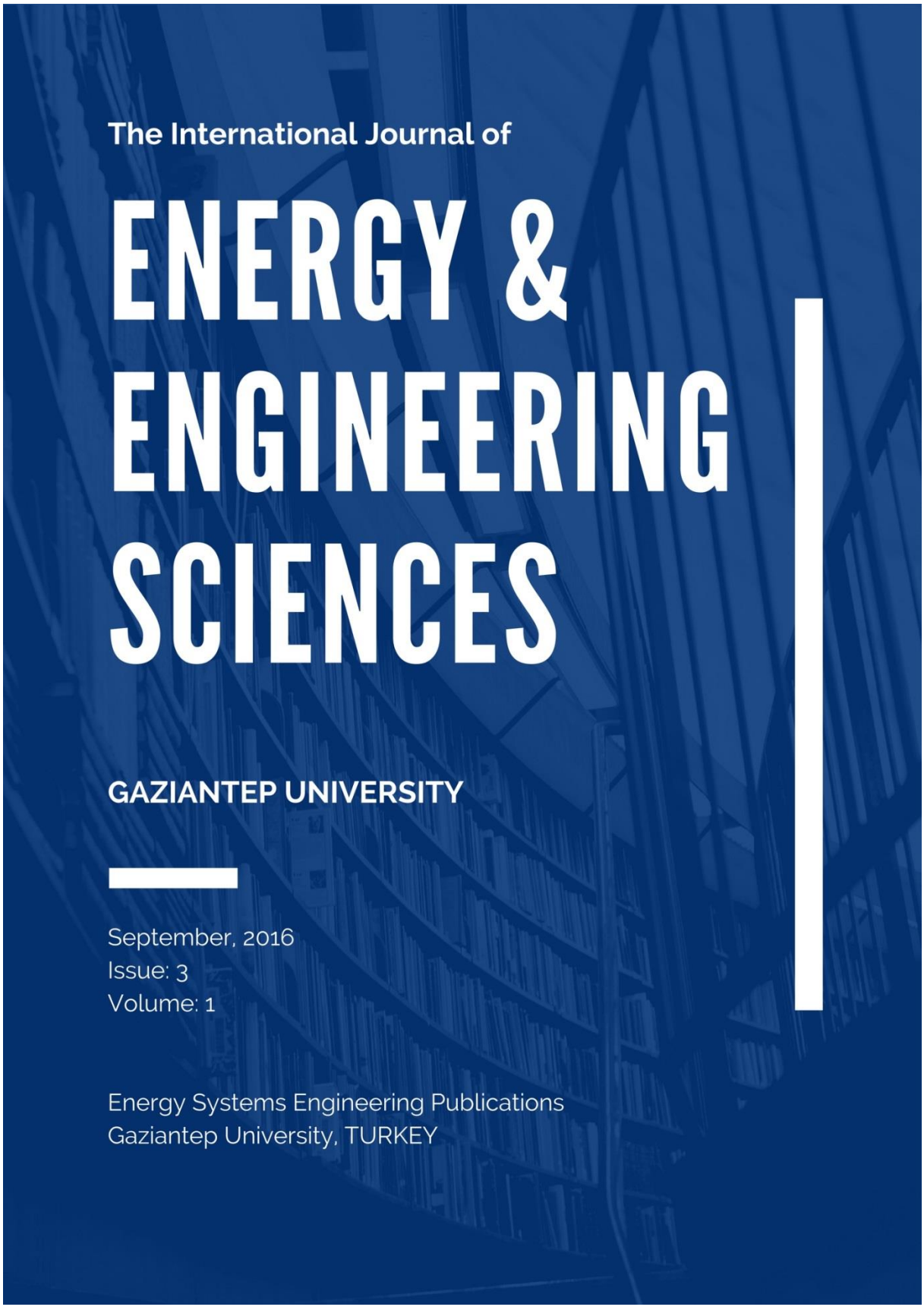
The International Journal of
ENERGY & ENGINEERING SCIENCES
GAZIANTEP UNIVERSITY
September, 2016
Issue: 3
Volume: 1
Energy Systems Engineering Publications
Gaziantep University, TURKEY

Gaziantep University Engineering Faculty
+90 342 360 12 00
+90 342 360 10 13
gaziantep.university.ijees@gmail.com
https://uemk-conferences.wixsite.com/ijees

Published by

Gaziantep university, Engineering Faculty, Energy Systems Engineering, Üniversite Bulvarı 27310 Şehitkamil - Gaziantep, TÜRKİYE

ISSN

Table of Contents

PWM CONTROLLED DC-DC BOOST CONVERTER DESIGN AND IMPLEMENTATION

Tolga ÖZER
Afyon Kocatepe University Electric-Electronic Engineering
tolgaozer@aku.edu.tr

Sinan KIVRAK
Ankara Yıldırım Beyazıt University Electric-Electronic Engineering
skivrak@ybu.edu.tr

Yüksel OĞUZ
Afyon Kocatepe University Electric-Electronic Engineering
yukseloguz@aku.edu.tr

ABSTRACT: In this study DC-DC boost converter circuit was designed and implemented. The converter input voltage range determined as 9V-30V DC and output voltage of boost converter is created as 48V DC. This converter has potential uses 48V compatible applications. In this circuit design, the implementation of a PWM DC/DC boost converter contains two subsystems – a conventional PWM boost converter and a control circuit. A PIC microcontroller is used to send the gating signals to a driver which drives the Metal-Oxide-Semiconductor Field Effect Transistors (MOSFET), allowing the converter's output to be kept steady at 48V and 220 W through pulse width modulation, even with a fluctuating input voltage. A switching frequency of 100 kHz was achieved, and PWM control method was used for switching. The use of a PWM boost converter allows for a variable input and constant output. The output is regulated by the control circuit which adjusts the duty cycle of the gating pulse to maintain a constant output.

Keywords: PWM, Microcontroller, Boost, Converter

INTRODUCTION

Increasing need for energy in today's world, limited existing energy sources and contamination of environment has made research lead to new and clean energy sources. Since increase of solar energy which is used as clean energy source, wind power and these kind of renewable sources increased the need for energy conversion, the use of DC-DC energy converters become widespread day by day.
In power sources such as solar panels energy obtained from energy resources at specific voltage value. Converters are used for to handle desired voltage value. With the inclining of energy markets to more environmental sources, practice of DC-DC voltage boost convertor type circuit has increased. In industrial practices, DC-DC boost convertors are used commonly. Most of researches which are about DC-DC

convertors have focused on putting forward the best switching method. In recent years, numerical control in power electronics has been used really intensively. Applying numerical control circuits to the power convertor circuits has increased circuit performance and the cost has decreased at the same time. Some typical practices of these types of convertors can be seen at auxiliary power sources practices of hybrid vehicles with fuel cells or practices involving sun panels. Electrical cars with the energy of fuel cell need energy storing devices for the first starting time. Under voltage battery packs are preferable for energy storing transaction .That's why, DC-DC converters are needed as an interface connecting under voltage battery packs and high voltage fuel cell systems.

When the literature is considering there can be seen studies which are related with DC-DC boost converter design. Çoruh N., Erfidan T., Ürgün S.(2008) are presented microcontroller boost convertor. Materialized power and controlled circuit at high switching frequency is worked for different charge situations and duty cycle rates. In the studies of Demirtaş M., Sefa İ., Irmak E., Çolak İ. (2008), a micro controlled based DA/DA boost convertor design and practice for solar energy systems is realized. A needed switching signal for the system to work is produced by microcontroller. In the practice in which sun panels are used to convert the energy taken from the sun to the electric energy, in order to make the system to work more efficiently, a micro controlled DA/DA boost convertor design and practice at 2600 W power is performed. Sathya P., Natarajan R. (2013) did a low cost, high performance and closed cycle DC-DC boost type convertor practice in their studies. HBLED led lamps are linked as charge to the converter output by making the input power to work as sun panel. All system is simulated by multisim program and fertility rate is 98,33%.System fertility is 95% when the same system is tested in laboratory. Thomas L., Midhun S., Mini P K, Thomas J.A., Krishnapriya M N (2014) did DC-DC voltage boost type converter practice circuit in their studies. The converter circuit that has the input voltage between 3V and 12V is designed as having 25V at the output. Şahin Y., Aksoy İ, Tınğ N. S (2015) presented a developed ZCZVT PWB DC DC boost convertor that has active compression cell.

A developed ZCZVT PWB DC DC convertor that has the capacity of gathering wanted features of resonance and overcoming unwanted features is presented by PWM study. Fathah A. (2013) did voltage boost voltage type circuit design whose input voltage 5V and output voltage 15V in his thesis paper. The converter yield is 94.16% in this practice by using MATLAP and PSPICE programs. Muthukrishnan P. and Dhanasekaran R. (2014) did DC-DC voltage boost circuit design which is formed by double inductors for sun panel practices in their studies. They did voltage gain by increasing the coiling number of the inductor they used. In the study, a converter whose input voltage is 60V, output voltage is 600V and power is 900W by using PSIM program. Hassan F. A. and Lanin V. L. (2012) did a dissipation less voltage boost type DC-DC converter for under voltage photovoltaic sun panels in their studies. The most significant advantage of this circuit topology is the low voltage tension at switching elements and high voltage rate is realized with low size and cost. Input voltage of circuit is 15V and output voltage of it is 130V.Fertility rate is

between 90% and 94% in 30kHz switching situation. Demirtaş M. and Şerefoğlu Ş. (2014) did ds-PIC controlled voltage boost type DC-DC converter practice for wind turbine system. In this practice, almost 35% efficiency increase is detected with the use of converter in the system. Tyagi P., Kotak V. C., Singh V. D. did from 30 to 50 high efficiency voltage boost type simulation circuit design with multiple coiling inductor with PSIM program. Especially it can be used to increase sun panels' under output voltage. Input voltage is 12V and output voltage is 360V which is fixed by PI controller.

In this study DC-DC voltage boost type circuit was designed and implemented. PWM controlled DC-DC converter design is made. Input voltage of the designed DC-DC voltage convertor circuit can change between 9V and 30V. Output voltage is fixed 48V. PWM signals are produced by 18f2550 PIC microcontroller. The converter output is fixed at 48V-240W by the produced PWM signals, even though there is fluctuation at the input.

METODOLOGY

Voltage boost type circuit having input voltage which is between 9-30V and output voltage which is fixed at 48V was designed. The maximum power of the circuit is designed as 240W. Circuit system mainly consists of two parts: power and control circuit. Firstly, control circuit will be designed and then design of power circuit starts. Since the circuit which will be designed is PWM controlled voltage convertor, PWM signal is necessary. PWM signal is formed by PC18f2550 microprocessor. Because of the features of microprocessor which will be used, PWM signals which are at different frequency values and duty cycles rates can be taken from metal pin. Additionally, since output voltage of voltage boost type circuit has to be at fixed 48V, output voltage of circuit will be applied to analog entrance of PIC18f2550 microprocessor. In this way, feedback can be provided and output voltage will be fixed at 48V in software. In software, output voltage will be fixed by increasing and decreasing duty cycle rate of PWM signal and adjusting it with the value taken from output of circuit. MikroC will be used as software language. After designing control card and getting right PWM signal, the design of power card starts and material choice according to the intended power value. Basically, voltage boost type circuit topology which will be applied is shown in Figure 1. According to this circuit topology, necessary elements will be chosen. MOSFET transistor will be used as switching element.

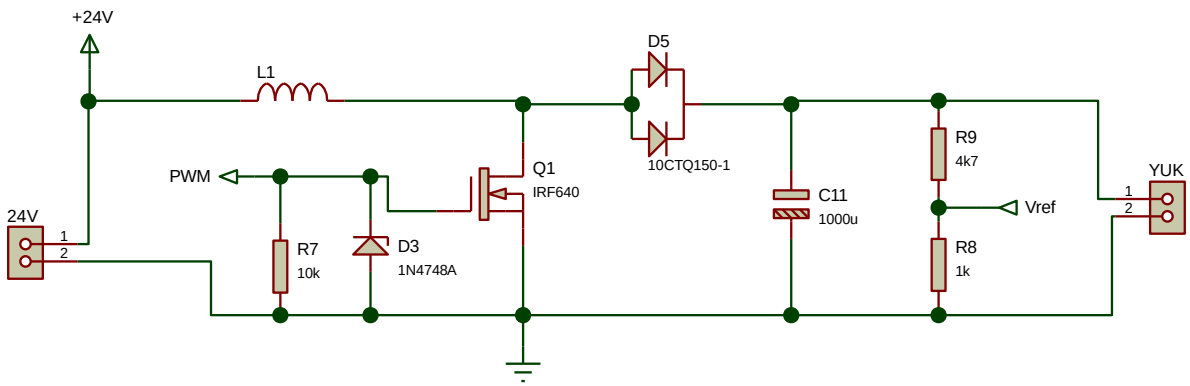

Figure 1: Conventional PWM Boost Converter

The components used for the boost converter, as shown in Figure 1, are as follows:

Power MOSFET Q1: STNF75NF

Schottkey Diode D5: MBL10100

Zener Diode D3

Caps/Resistors – values as shown on circuit diagram

Inductor L1– Wound with 3 turns using a core of material ETD 59/31/22.

The purpose of the control circuit is to provide to the MOSFET with gating pulses. The main components of the control circuit are the microprocessor, the optocoupler and the Mosfet drivers. The microprocessor used was the PIC18f2550.

The schematic of the control circuit can be seen below in Figure 2.

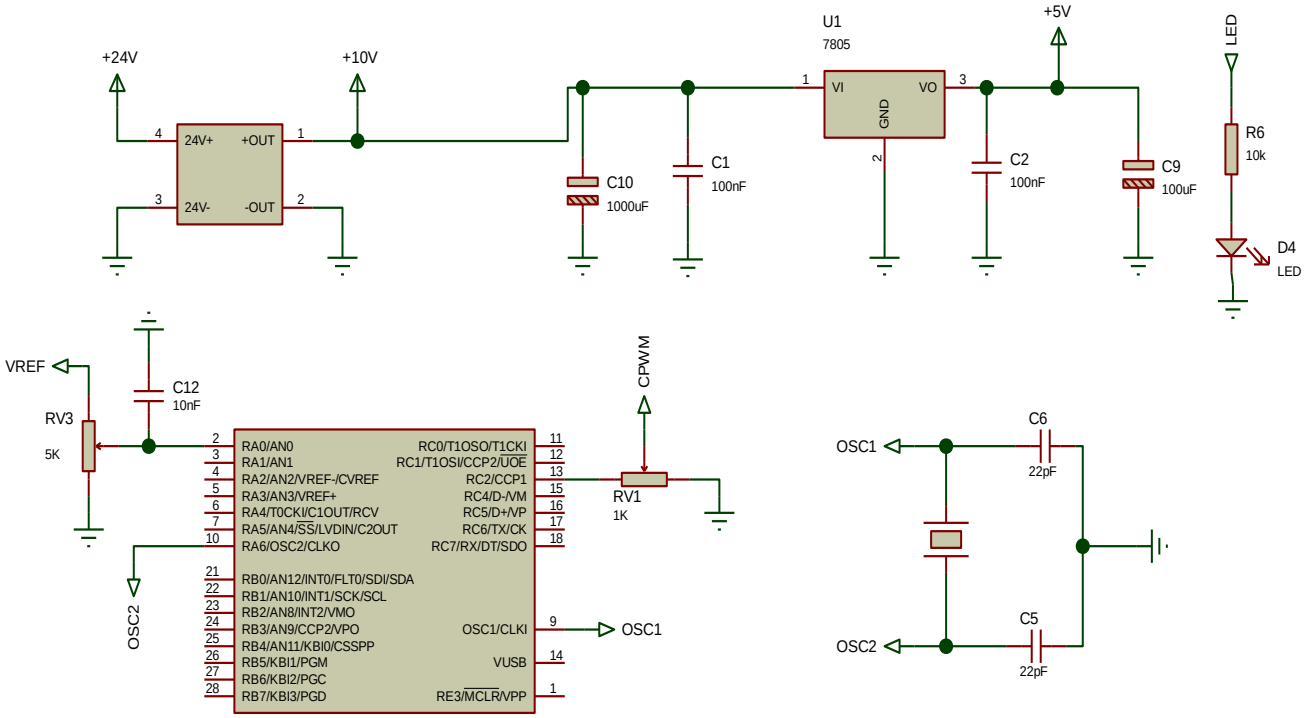

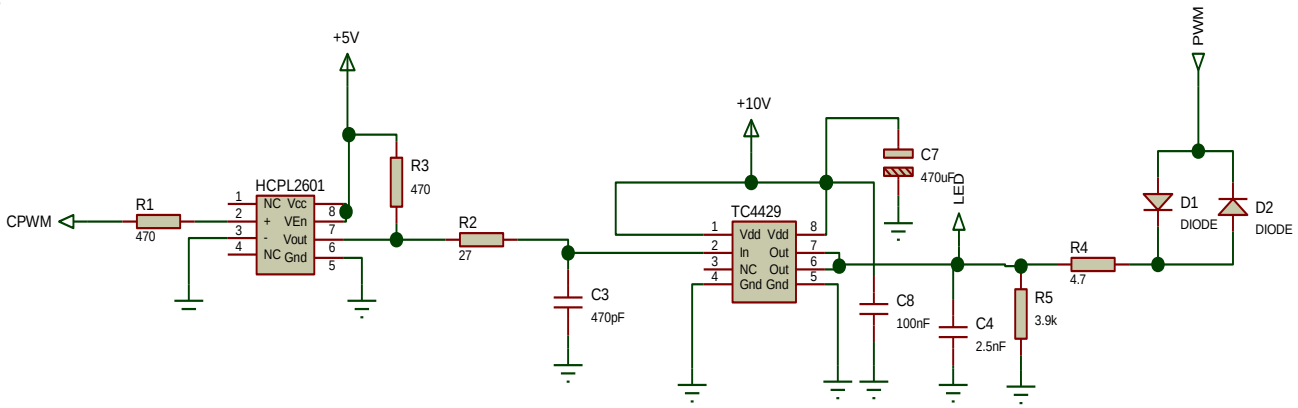

Figure 2: Control Circuit

The microprocessor was programmed to output two gating pulses. The circuit was tested effectively with a switching frequency of 100 kHz. Pulse is sent at a frequency of 100 kHz with an initial duty cycle of the Mosfet set to 50%.

A feedback loop is implemented to ensure a constant 48V is obtained at the output for 24VDC input voltage. The microprocessor is programmed to automatically adjust the duty cycle according to a comparison made between a reference voltage of 4.2V and a feedback signal from a voltage divider at the output. This comparison makes use of the 18f2550 analog to digital converter. The voltage divider (shown in Figure 1 as R8 and R9) is designed such that at the desired output of 48V the feedback signal is 4.2V and no adjustment of the duty cycle is made. If the output voltage is greater than 48V the duty cycle is decreased until the desired output voltage is obtained. If the output voltage is less than 48V the duty cycle is increased until the desired output is obtained. The microprocessor continuously loops through this code adjusting the output voltage according to the variance in the input voltage. After each loop the reference is checked again to ensure the output voltage is maintained.

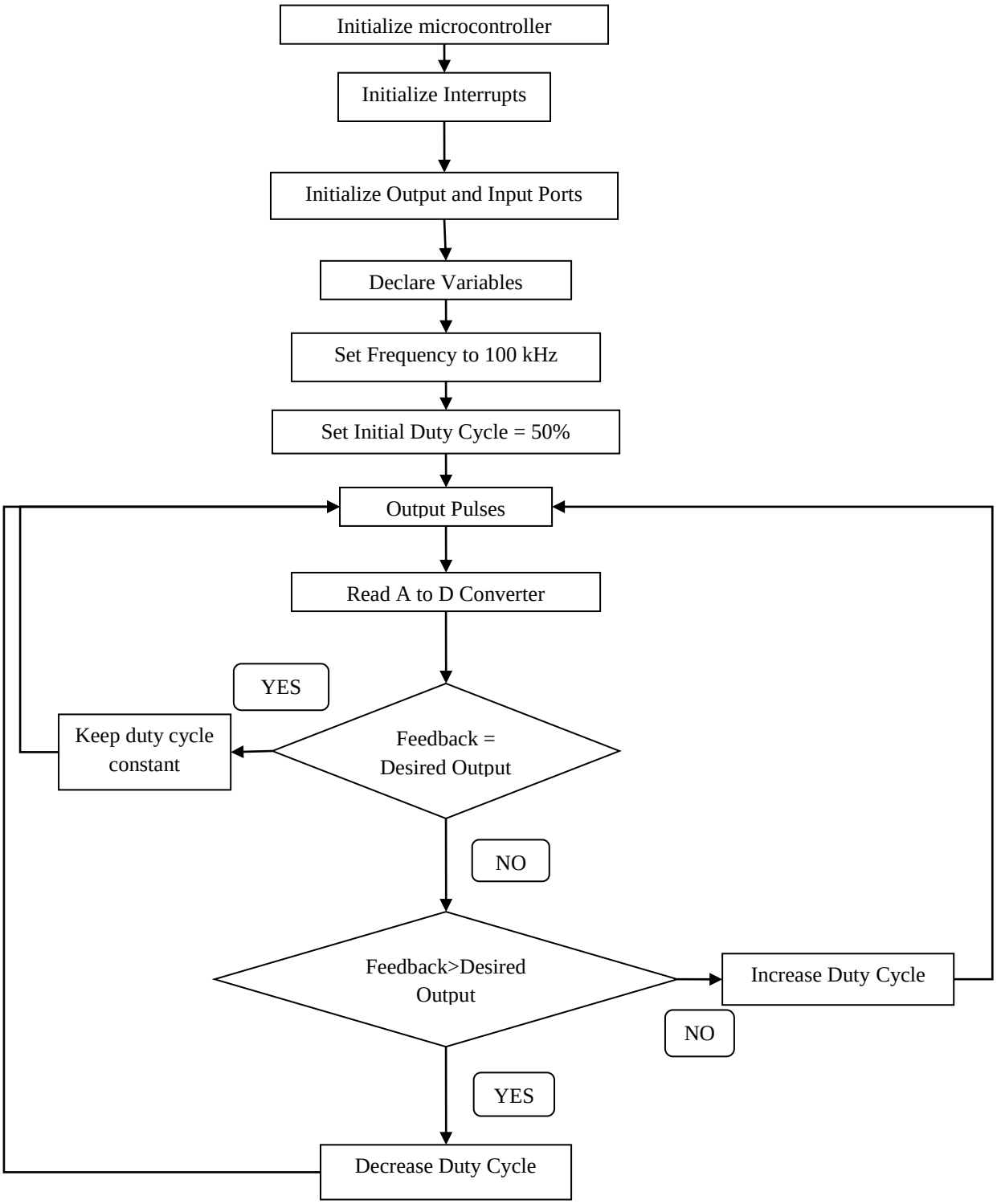

Figure 3: Microcontroller Flow Diagram

Experimental Results

The PWM DC/DC Boost Converter was built in the laboratory and the actual product resulted in the following specifications:
Input Voltage Range: 18-24VDC
Output Voltage: 48VDC

Output Power: 220W
Switching Frequency: 100kHz
Efficiency, η, of the PWM DC/DC Boost Converter can be determined as follows:

$$\eta = \frac{P_{out}}{P_{in}} = \frac{V_{out} I_{out}}{V_{in} I_{in}} \quad (1)$$

where V_{out}, V_{in}, I_{out} & I_{in} can all be measured in the laboratory.
Table 1 below details the Voltage and Current measurements taken in the laboratory at resistive loads, and the resulting efficiency calculations: Designed converter can be seen at Figure 4.

Table 1: Voltage and Current Measurements and Resulting Efficiency and Various Resistive Loads

V_{in} (V)	I_{in} (A)	V_{out} (V)	I_{out} (A)	η (%)
24	8	48.00	2.8	70.00
24	10	48.00	4.6	91.60

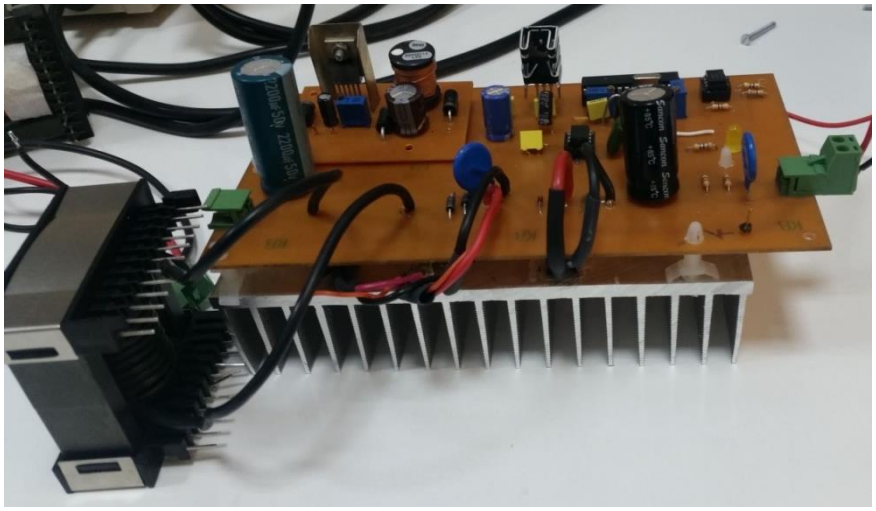

Figure 4:Designed Boost Converter

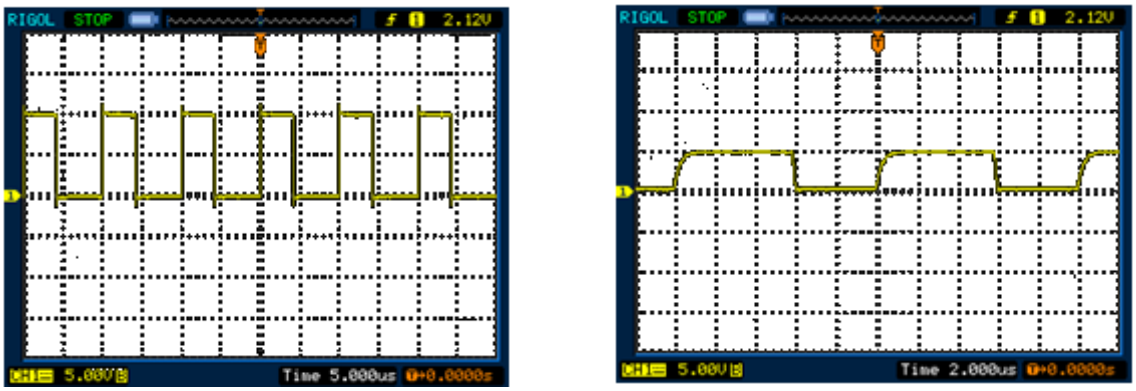

Figure 5. TC4429 and HCPL2601 PWM Output Signals

At Figure 5 there can be seen PWM signals. TC4429 was used as a MOSFET driver and HCPL2601 was used as an optocoupler. These PWM signals belong to

respectively TC4429 and HCPL2601 ICs. As a result of these IC PWM signal is not corrupted while 100 kHz signal applied.

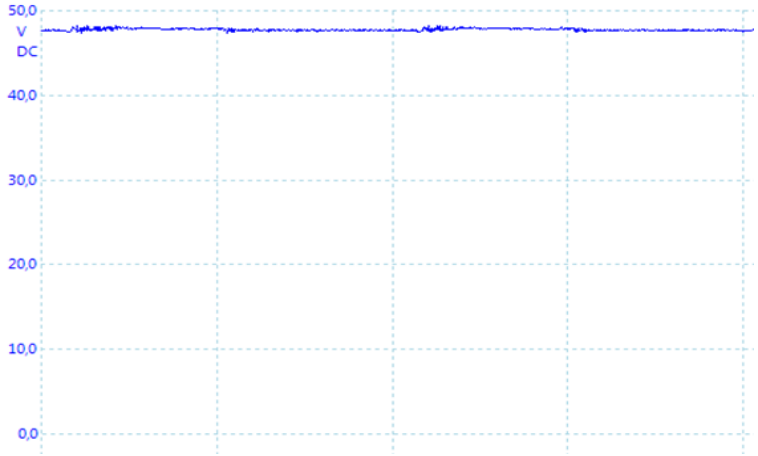

Figure 6 Boost Converter Output Voltage at DC Mode (5 µs)

According to Figure 6 the converter DC output value can be seen as 48 V. Figure 6 was taken from DC mode. And at Figure 7 boost converter output voltage is investigated at AC mode. And it is seen nearly 0.2-0.3 ripple voltage value at Figure 7.

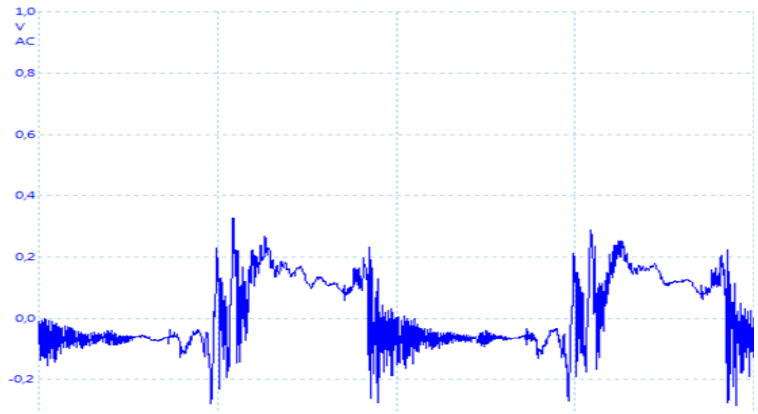

Figure 7 Boost Converter Output Voltage at AC Mode (5 µs)

Costs

The costs associated with the design and implementation of the PWM DC/DC boost converter were relatively low given the simple design of both the conventional boost converter. The per unit costs are detailed below in Table 2:

Table 2: Per Unit Costs for the PWM DC/DC Boost Converter

Component	Part Number	Unit Price (TL)	Quantity	Total Cost
FET Driver	AC419	8	1	8
Optoisolator	ICPL 2601	10	1	10
Power MOSFET	NF75NF	5	2	10
Schottkey Diode	BR10100	10	1	10
5V Regulator	LM7805C	3	1	3

Microcontroller	PIC18f2550	15	1	15
4 MHz Crystal Oscillator	4.0000M-C	5	1	5
PCB Board		20	1	20
Miscellaneous Parts	Capacitors/Resistors etc.			10
MOSFET Heatsink		20	1	20
Ferrit Core	ETD 59/31/22	20	1	20
	Total Per Unit Cost:			111 TL

CONCLUSION

The two subsystems of the PWM DC/DC Boost Converter – the conventional PWM boost converter and the control circuit were constructed and tested in the laboratory. The PWM boost converter proposed for this project was tested at a switching frequency of 100 kHz. This switching frequency is equal the project goal of 100 kHz. Theoretical calculations were made and used to select components for each of the subsystems. First each subsystem was test individually and then the subsystems were implemented and tested together.

The circuit was tested with resistive load and the circuit was confirmed to be functional at a minimum of 50W, and a maximum of 220W. The overall efficiency of the PWM DC/DC Boost converter was calculated though measurements taken in the laboratory to be %91.6. With this high efficiency and relative low per unit cost of 111 TL, this PWM DC/DC boost converter is suitable for applications such as solar battery storage systems or fuel-cell powered electric vehicles where a fixed out of 48VDC is required.

In future studies the PWM DC/DC converter can be implemented with digital programmable logic device such as an FPGA for a higher switching frequency with using a different type of Mosfet which Rds value lower than used in this article. Also soft switching techniques can be implemented to Mosfets for increasing circuit power and efficiency rate.

REFERENCES

Çoruh N., Erfidan T., Ürgün S.(2008). DA-DA Boost Tipi Dönüştürücü Tasarımı ve Gerçeklenmesi ,Elektrik-Elektronik-Bilgisayar Mühendisliği Sempozyumu , Eleco 2008, 1, 362-365

Demirtaş M., Sefa İ., Irmak E., Çolak İ. (2008). Güneş Enerjili Sistemler İçin Mikrodenetleyici Tabanlı Da/Da Yükselten Dönüştürücü, Gazi Üniv. Müh. Mim. Fak. Der. Cilt 23, No 3, 719-728

Sathya P., Natarajan R., (2013). Design and Implementation of 12V/24V Closed loop Boost Converter for Solar Powered LED Lighting System, International Journal of Engineering and Technology (IJET), Vol 5 No 1 Feb-Mar 2013

Thomas L., Midhun S., Mini P K, Thomas J.A., Krishnapriya M N, (2014). DC to DC Boost Converter for Custom Based Application, International Journal of Advanced

Research in Electrical, Electronics and Instrumentation Engineering, Vol.3 , Issue 2, February 2014
Şahin Y., Aksoy İ, Tınğ N. S. (2015). Geliştirilmiş Bir ZCZVT-PWM DC-DC Yükseltici Dönüştürücü, Sigma Mühendislik ve Fen Bilimleri Dergisi, 33 (4), 2015, 639-651
Fathah A. (2013). Design of a Boost Converter, Department of Electrical Engineering National Institute of Technology Rourkela-769008 (ODISHA), June-2013
Muthukrıshnan P., Dhanasekaran R. (2014). DC- DC Boost Converter For Solar Power Application, Journal of Theoretical and Applied Information Technology, Vol. 68 No.3
Hassan F. A., Lanin V. L. (2012), Loseless DC-DC Boost Converter With High Voltage Gain For PV Technology, Asian Transactions on Engineering (ATE ISSN: 2221 - 4267) Volume 02 Issue 04
Demirtaş M., Şerefoğlu Ş. (2014) Design and implementation of a microcontroller-based wind energy conversion system, Turkish Journal of Electrical Engineering & Computer Sciences, 22: 1582-1595
Tyagi P., Kotak V.C., Singh V. P. (2014). Design High Gain DC-DC Boost Converter With Coupling Inductor And Simulation in Psim, International Journal of Research in Engineering and Technology, Volume: 03 Issue: 04

THE STUDY OF THE EFFECT OF THE MOULD PARAMETERS ON THE MOULDING FORCE IN THE DEEP DRAWING PROCESS OF DP600 MATERIAL

Erhan KARA
Uludag University
erhankara@uludag.edu.tr

Çetin KARATAŞ
Gazi University
cetink@gazi.edu.tr

Sevinç ZAFER MUTLU
Uludag University
sevinczafer@uludag.edu.tr

ABSTRACT: The goal of this study is to determine the suitable die parameters which are used to shape the high strength sheet metal before die production, and to design and produce proper dies using these parameters and get cups with desired production quality economically.
In this study, the parameters affecting the deep drawing process were experimentally investigated. The experiments were carried out by using samples drawn from high-strenght DP600 quality of 0,9 mm thick. All the experiemnts were realized by using Hounsfield tension-compression test device. The effects of the die radius (2,3,4 and 6 mm) punch curve radius (2,3,4 and 6 mm), punch velocity (60, 150, 250 and 350 mm/min) and lubrication (without lubricant, stretch film and mineral oil) parameters on the moulding force were investigated. It was observed that the sheet material was wrecked in small die radius. Furthermore, it was observed that molding force decreased when the punch velocity and die radius increased. The same relationship was determined when the present lubricant is replaced with other oil. The smallest molding force was obtained when strech film was used.

Key words: Deep drawing, metal forming, plate materials, radius of punch.

INTRODUCTION

The drawing process has an important place for cold shaping of plate material. According to the statistical studies, drawing die (60%) and drawing punch (18,8%) are the most effective parameters on the drawing process of the radius (Colgan, 2003).

In drawing dies, various drawing methods are applied according to the process type, size and material. These methods are basically as follows (Güneş, 2005; Simith, 1990);

At the beginning of the drawing process with hold-down force, a certain force is applied to the lamella by the compression plate and the plate which will be drawn is jammed between the drawing die and the compression plate. The aim of this compression is to prevent wrinkles formed during the drawing process. This kind of drawing process is necessary to prevent the wrinkles formed when the thickness of the sheet material is low or the height of pull is high. The elements used for the drawingl with hold-down force are indicated in the figure 1 (Güneş, 2005; Simith, 1990).

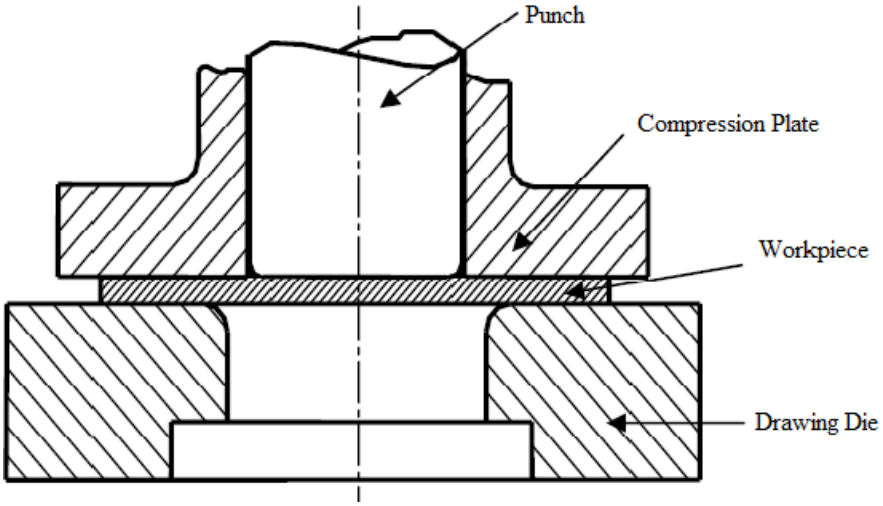

Figure 1. The Basic Elements Used For The Drawing Process With Hold-Down Force (Simith, 1990).

The operation order of the drawing with compression plate is indicated in Figure 2.

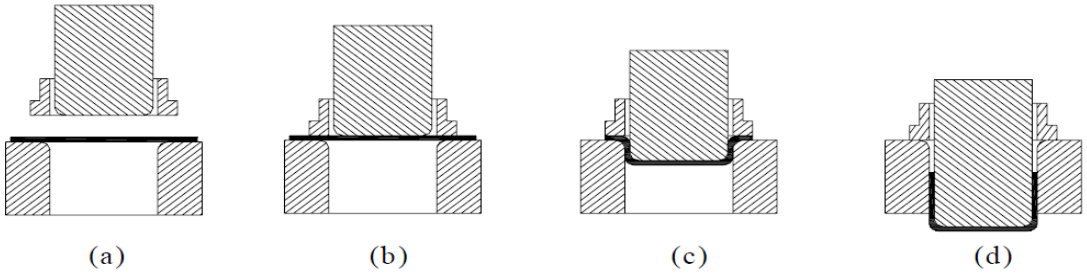

Figure 2. The Pull Operation With Compression Plate (Güneş, 2005).

The position of the sheet material
The apply of compression force
The beginning of drawing
The end of drawing
Various experimental studies were done to determine the effects of the mould parameters (drawing die curve, punch curve, feed rate and lubrication) affecting the forming of during the deep drawing process of high-strenght plates used more in

our day. At the end of the experiments, the suitable mould parameters are determined fort he moulding of high-strength plates.

The sheet Material

In this study, the DP600 quality plate of 0.9 mm, which has been used on new generation automotive parts and parts which require high-strenght (security and safety) was used . The characteristics of the sheet material used in this study are indicated in table 1.

Table 1. The Characteristics Of DP600 Quality Plate Material

Element	%	Element	%
Carbon (C)	0.086	Silicium (Si)	0.356
Mangan (Mn)	1.455	Aluminium (Al)	0.028
Phosphorus (P)	0.023	Copper (Cu)	0.018
Sulphur (S)	0.007	Niobium (Nb)	0.001
Mechanical Properties			
Tensile Strength		620 MPa	
Yield Strength		400 MPa	

METHODS

For the deep drawing methods, round plate material of 32 mm, 35 mm and 40 mm diameter were used. Thedrawing rates for the primitive lamella diameters are indicated in table 2. The compression plate, drawing die mould and surface roughness of drawing punch are indicated in table 3.

Table 2. Experimental Sample Diameters Depending On Draw Ratio (B)

Plate Diameter (mm)	Draw Ratio (β)
32	2
35	2,18
40	2,5

Table 3. Compression Plate, Drawing Die And Surface Roughness Of Drawing Punch

	Ra, µm	Rz, µm	Rt, µm
Compression Plate	0,3595	2,2725	3,3335
Drawing Die	1,7391	7,9981	8,4045
Punch	1,7439	10,5855	12,3372

Test Conditions

They were negative for all the mould parameters in the pull operations carried out for the 35 mm and 40 mm lamella diameters and all the drawed vessels were torn. The limit draw ratios of the high-strenght plates were not above 2 (Bozdok, 2008).

Therefore, the plate material of which lamella diameter was 32 mm was used in the tests. The test samples were prepared on eccentric press machine by using cut mould. The hold-down force (see figüre 3.) was 4378 N. The pulling force was counted as 29462 N. The single sided contraction cavity was counted as 1,11 mm and it was 1,15 on the mould manufacturing. The drawing die cavity was counted as 2,08 mm and the drawing die cavities were 2, 3, 4 and 6 mm. The feed-rate for these four punches were 60, 150, 250 and 350 mm/mn.

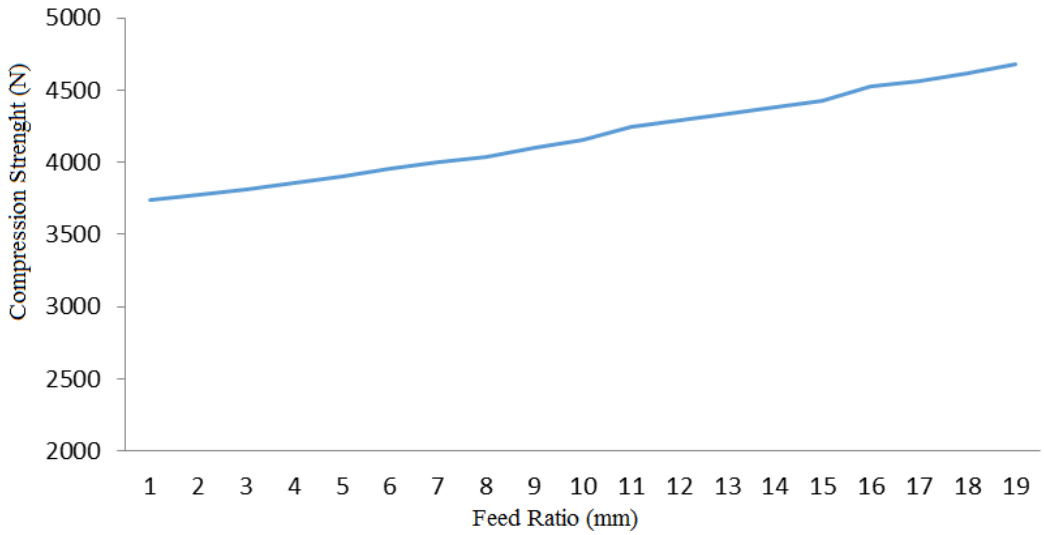

Figure 3. The Change Of Compression Strenght According The Pinch.

RESULTS AND FINDINGS

During the experimental studies, the control movement of the drawing punch and the forces taken place during the tests were recorded and saved on computer. The obtained forces were determined as moulding forces. The products obtained at the end of the tests are indicated in Figure 4.

Figure 4. The Products Obtained From The Experimental Studies

The results obtained from the tests done with cylindrical drawing dies, on DP600 steel plate material, by using different drawing die, punch cavities, lubricants and press speeds were interpreted.

The Effect Of The Feed Rate Of The Punch On The Moulding Force

The effects of the feed rate of the punch on the moulding force for DP600 plate material on the drawing die are indicated in Figure 5.

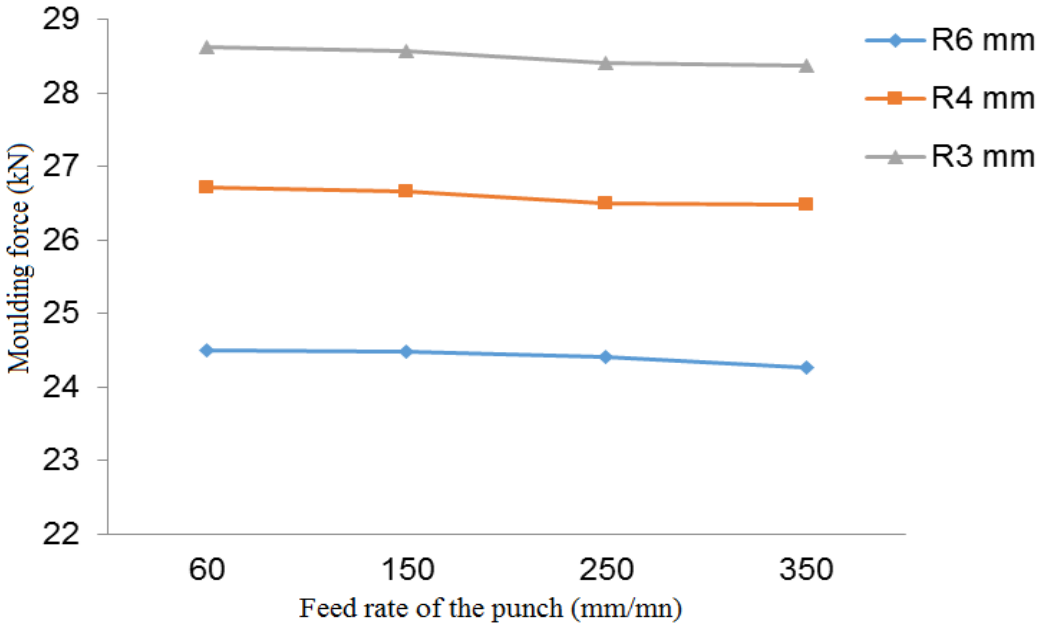

Figure 5. The Effect Of The Feed Rate Of The Punch On The Moulding Force For DP600 Plate

The drawing tests done on DP 600 material without lubricant showed that there was a decrease in the moulding forces when the feed rate of the punch increased. The highest moulding force was 28630 N for the drawing die of 3 mm and punch cavities and the lowest moulding force was 28350 N. The highest moulding force was 26710 N for the drawing die of 4 mm and punch cavities and the lowest moulding force was 26480 N. The highest moulding force was 24510 N for the drawing die of 6 mm and punch cavities and the lowest moulding force was 24270 N.

The Effect Of The Lubrication On The Moulding Force

The effects of the lubricants on the moulding force for the DP 600 sheet material at different punch feed rates on drawing dies are indicated in Figure 6.

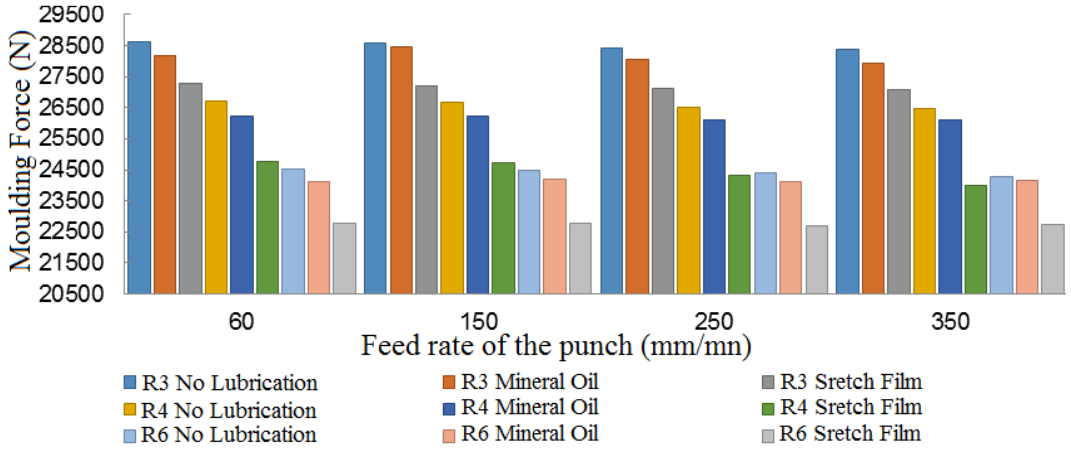

Figure 6. The Effects Of The Lubricants On The Moulding Force For the DP600 Material

When the results obtained from the tests were examined, it was seen that mineral lubricant decreased the friction between the plate material and mould cavity in proportion to the pull operation without lubricant and as a result, decreased averagely the moulding force at 1.7%. The strech film became more effective in decreasing the moulding force and it decreased the moulding force averagely 7,4% (Park and et a, 2002).

Lubrication decreases the moulding force. Dry film lubrication decreases effectively the moulding force (Allen, 2008; Kim, 2007).
The Effect Of The Feed Rate Of The Punch On The Moulding Force Depending On The Punch Speed

The 3 different die mould (3,4 and 6 mm) and punch cavity values were used in the tests. The mould cavities have important effects during the plate material's flux into the mould cavity. For a successful drawing, suitable mould cavities will be useful.

The effects of the drawing die and punch curve values on the moulding force of the punch feed rate for the DP 600 material are indicated in Figure 7.

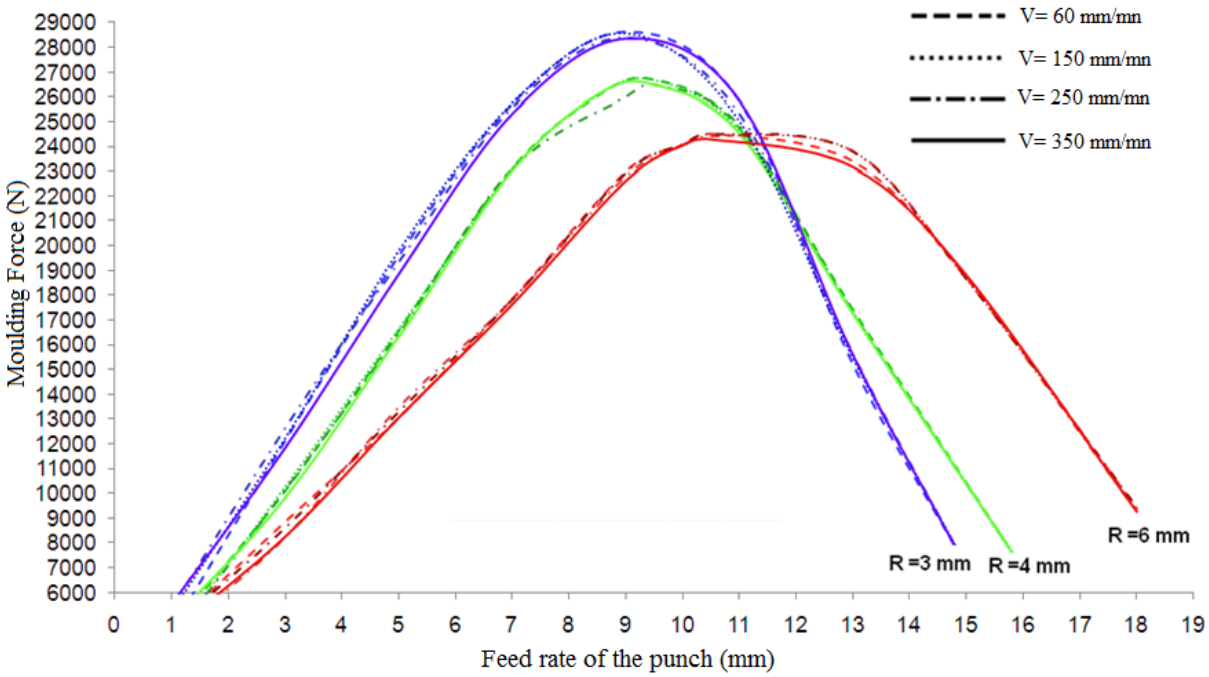

Figure 7. The Effect Of The Punch Feed Rate On The Moulding Force For The DP 600 Material

It was seen that there was a decrease in the moulding force when the drawing die cavity increased. The lowest pull force was on the mould cavities of 6 mm. It was also seen that there was a decrease when the pulling speed increased.

CONCLUSION

After having examined DP 600 sheet material experimentally, it can be inferred that its usage especially in automotive industry in a widespread manner will save up energy and fuel economy considerably since it is light and has high-strenght characteristics; as a result, since fuel consumption decreases, harmful substances will decrease in the environment.

Limit draw ratio in the shaping of high-strength sheets doesn't go beyond 2.
There has been a tearing in the drawing die of 2 mm and curve radius of drawing punch, in all the mould parameters when sheet material was used. The drawing die curve radius of 2 mm and the curve radius of the drawing punches are insufficient in shaping high-strength plates of 0,9 mm.
It was seen a decrease in the moulding force during shaping the part when the curve radius of the mould increased.
It was found that the drawing die radius was more effective than the punch radius to decrease the moulding force.
Increasing the feed rate of the punch didn't change the moulding force but it was seen a slight tendency of decrease in the moulding force.
The lubrication with strech film decreased the moulding force significantly.

RECOMMENDATIONS

The compression plate force and the effects of drawing cavity can be studied. This study was done with cold shaping. Another study can be done with warm and hot shaping. The effects of profile and rolling direction on the drawing process can be studied by using more different drawn profile. High-strenght materials of different thickness can be studied by using this method. The test results can be compared by using analyse programmes and suitable moulding parameters for different materials can be determined.

REFERENCES

Colgan, M., Monaghan, J., (2003). Deep Drawing Process Analysis and Experiment, Journal of Materials Processing Technology, 132: 35-41.

Kara, E. (2011). DP500 Ve DP600 Sac Malzemelerin Derin Çekilebilirliğinin İncelenmesi. Gazi Üniversitesi, Ankara,1-94.

Güneş, A.T. (2005). Pres İşleri Tekniği Cilt 2. Makine Mühendisleri Odası, Ankara, 1-207.

Bozdok, M. (2008). Advanced High-Strength Steel Product and Process, A Special Edition of In-Depth AHSS Case Studies Including Excerpts from the World Auto Steel AHSS Applications Guidelines, Auto/Steel Partnership, Michigan, 25.

Çapan, L. (2003). Metallere Plastik Sekil Verme 4. Baskı. Çağlayan Kitabevi, İstanbul, 1-180

Uzun, İ., Eriskin, Y. (2002). Sac Metal Kalıpçılığı. Milli Eğitim Bakanlığı Yayınları, Ankara. 1-360.

Takahashi, M. (2006). Development of High Strength Steels for Automobiles. Nippon Steel Technical Report, 88.

Shi, M. (2001). Formability Performance Comparison between Dual Phase and HSLA Steels. Iron & Steel Society, 39:165.

Power, W. F. (2000). Automotive Materials in the 21st Century. Advanced Materials and Processes, 210.

Deanna,S., (2001). Technology Transfer Dispatch No.6 Provides Valuable Information on the Selection of Advanced High-Strength Steels for ULSAB-AVC. Lorincz American Iron and Steel Institute, Detroiit, 76:84.

Kishor, N., Kumar, R. (2002). Optimization of initial blank shape to minimize earing in deep drawing using finite element method. Journal of Materials Processing Technology, 130-131: 20-30.

Simith, A.D.,"Die Design Handbook", Society of Manufacturing Engineers, Michigan, 10,1-12,43 (1990).

Park, D.H., Huh, Y.M., Kang, S.S., "Study on punch load of non-axisymmetric deep drawing product according to blank shape", Journal of Materials Processing Technology,130-131:89-94 (2002).

Kim, H., Sung, J.H., Sivakumar, R., Altan, T., "Evaluation of stamping lubricants using the deep drawing test" International Journal of Machine Tools and Manufacture, 47: 2120-2132 (2007).

Allen,S.J., Mahdavian, S.M., "The effect of lubrication on die expansion during the deep drawing of axisymmetrical steel cups", Journal of Materials Processing Technology,199: 102-107 (2008).

GRAIN DIFFUSION AND DISPERSION OF CLAYEY SOILS IN A CONSOLIDATION PHENOMENON

Barış MAHMUTLUOĞLU
Mersin University
bmahmutluoglu@mersin.edu.tr

Mehmet Arslan TEKİNSOY
Şırnak University
matekinsoy@sırnak.edu.tr

Baki BAĞRIAÇIK
Çukurova University
bbagriacik@cu.edu.tr

ABSTRACT: In this study, the phenomena of grain diffusion and dispersion were considered and the effects of time rates of settlement on consolidation were discussed. It was shown that time rates of settlement can be considered throughout the consolidation process of a soil in terms of grain diffusion and dispersion. For this reason, consolidation tests were performed on soil samples taken from a specific region in Adana Turkey in order to investigate and evaluate diffusive and dispersive characteristic of the region. By comparing the obtained experimental results to theoretical counterparts, it was seen that the results were in a very close aggreement to each other. These results were also compared to each other in order to observe the effect of plasticity of a clayey soil in grain diffusion and dispersion.

Keywords: grain diffusion, dispersion, consolidation, plasticity, clayey soil.

INTRODUCTION

In soil mechanics, as well as stress-strain relationships, deformation-time relationships are also important. For this reason, deformation-time relationship is explained by the theory of consolidation. The first theory on consolidation was given by Terzaghi and the change in pore water pressures as a result of the variations in hydraulic gradient was defined by the following equations given below as Equation 1.a and Equation 1.b (Özaydın 2005):

$$\frac{\partial u}{\partial t} = c_v \frac{\partial^2 u}{\partial z^2} \qquad (1.a)$$

$$c_v = \frac{K}{m_v \gamma_w} \qquad (1.b)$$

The independent variables in this differential equation are the coordinate z and time t. c_v and u represent the coefficient of consolidation and pore water pressure, respectively (Battaglio et al. 2003). Terzaghi's theory of consolidation is a linear theory which considers compaction and settlement of saturated and homogeneous soils. In this theory, the coefficient of consolidation was accepted to be a parameter as a result of small deformation amounts, compatible soil water permeability and compressibility values (Geng et al 2006). In addition, compressibility and permeability of a soil were considered to stay constant for a soil layer whereas aforementioned soil parameters differ according to the type and history of a soil (Battaglio et al 2005). On the other hand, the non-linear nature of a consolidation phenomenon and viscous property of soils cause a creep effect at the upper layers of a soil. Therefore, viscous effect is related to the continuous and slow deformations of a soil subjected to an external loading (Asch et al 1989). The aforementioned creep phenomenon is taken into consideration as a diffusion movement throughout a soil mass (Culling 1963). In all of the consolidation equations, the occurrence of laminar and transient flows and the validity of Darcy's Law have been accepted. It is also known that time rate of settlement and drainage decrease as a result of consolidation. Low time rates of settlement which occur under these conditions bring out the phenomena of hydrodynamic dispersion along with the viscous nature of fine grained soils. The term hydrodynamic dispersion stands as a process in which both grain diffusion and dispersion of a soil are considered. Consolidation process has also a profound effect on the transportation of contaminating particles throughout a compressed porous medium. It was observed that drainage of pore water is highly effective in the transportation of soluble particles inside of a soil mass by means of diffusion. Eventually, the random nature of pore structure of a soil mass and the transportation and spreading of contaminating particles in a soil brings out the diffusion problem. In addition, since courses and directions and so time rates of pore water differ vastly during the application of a loading as a result of random pore geometries, the phenomenon of dispersion also comes into question. Hydrodynamic dispersion, in general, defines the combined effect of orientation of particles to form a more disperse structure and grain diffusion occurring as a result of very low time rates of settlement. On the other hand, hydrodynamic dispersion is a phenomenon which occurs in micro pores and at the outside of a solid-liquid intersection as a result of low flow velocities (Tekinsoy 2013). Also, according to performed studies, dispersion is a physical phenomenon that occurs between solid and liquid phases as a result of low time rates of settlement. Variations in time rates of settlement occur in relation to the changes in pore water pressures (Nielsen et al. 1972). However, dispersion and grain diffusion were only studied by the writers of this study in an aspect of soil mechanics. Besides of soil mechanics point of view, the only study about the subject was in the transportation of melted particles in homogeneous soils as a result of a concentration gradient (Nielsen et al. 1972). In this study, the phenomena of dispersion and grain diffusion in the consolidation of clayey soils are studied and effects of time rates of settlement in a consolidation phenomenon are discussed. Obtained data are given in an aspect of hydrodynamic dispersion and some contributions are presented.

METHODS

Consolidation tests are generally performed on fine grained and plastic soils. Therefore, soil samples taken from different regions of Adana with various dry unit weights and plasticity properties are used in this study. Results of these experiments are both compared to theoretical counterparts and to each other. Physical properties of the soil samples are given in Table 1.

Table 1. Index Properties of Soil Samples (Mahmutluoğlu ve Tekinsoy, 2015)

Sample No.	Samp.1	Samp.2
Drilling Depth (m)	1.6	8.4
Liquid Limit (w_L) (%)	45	82
Plastic Limit (w_p) (%)	19	24
Finer than No.200 Sieve (%)	96	96
Activity	0.271	0.604
Natural Water Content (w_n) (%)	26	28
Dry Unit Weight (γ_k) (gr/cm^3)	1.319	1.284
Unit weight of Grains (γ_s) (gr/cm^3)	2.520	2.520
Natural Unit Weight (γ_n) (gr/cm^3)	1.662	1.644
Plasticity İndex (I_p) (%)	26	58

Note: Samp.1 and Samp.2 represent the soil samples which were taken from Adana Kayışlı District from depths of 1.6 m and 8.4 m, respectively.

Initially, the phenomenon was studied statistically and it was realized that dry unit weight is the primary variable in dispersion (Mahmutluoğlu 2014). As a result of the performed regression analyses, the most compatible equations to the phenomena were constructed and eventually Equation 2 was given as the dispersion differential equation (Mahmutluoğlu 2014):

$$\frac{\partial u}{\partial t} = v_z \frac{\partial u}{\partial z} + c_v \frac{\partial^2 u}{\partial z^2} \qquad (2)$$

The equation of dispersion given as Equation 2 is an equation which includes convective flow relative to time rates of settlement along with the conventional consolidation term. Since dry unit weight is the primary parameter in hydrodynamic dispersion, based on the equation given in Equation 2, the following differential equation can be derived as the dispersion differential equation with respect to dry unit weight (Mahmutluoğlu 2014):

$$\frac{\partial \gamma_k}{\partial t} = v_z \frac{\partial \gamma_k}{\partial z} + D_s \frac{\partial^2 \gamma_k}{\partial z^2} \qquad (3)$$

where, γ_k is dry unit weight, v_z is time rate of settlement and D_s is diffusivity coefficient.

Diffusivity coefficient and the other hydrodynamic dispersion parameters were obtained by solving the differential equation given as Equation 3 (Mahmutluoğlu 2014). These solutions were used in this study to obtain diffusion and dispersion parameters of a specific region in Adana Turkey and to show the effect of plasticity on the phenomena by comparing clayey soils of low and high plasticity properties. The equations for diffusion and dispersion parameters which were found by solving dispersion differential equation are given by Equation 4, Equation 5, Equation 6, Equation 7, Equation 8 and Equation 9 in the following pages of the study (Tekinsoy 2013; Mahmutluoğlu 2014).

RESULTS AND FINDINGS

Results of the performed consolidation tests on CL group soil samples can be seen in Table 2. Based on the results given in Table 2, diffusive and dispersive parameters are obtained and presented in Table 3.

Table 2. Effective Stress Variations relative to Dry Unit Weights for the CL group Sample taken from Kayışlı District (Mahmutluoğlu ve Tekinsoy, 2015)

Total Press. p (kg/cm^2)	Samp. Height H (mm)	Void Ratio e (%)	Pressure Increment Δp (kg/cm^2)	Dry Unit Weight γ_k (gr/cm^3)	Coeff. Of Volume Comp. m_v (cm^2/kg)	Efective Stress Increment σ' (kg/cm^2)
0.00	20.000	91.10	-	1.319	-	-
0.13	19.898	90.10	0.13	1.326	0.041	0.129
0.25	19.858	89.80	0.13	1.328	0.016	0.094
0.51	19.756	88.80	0.25	1.335	0.021	0.250
1.02	19.510	86.40	0.51	1.352	0.025	0.506
2.04	19.047	82.00	1.02	1.385	0.024	1.005
4.07	18.392	75.70	2.04	1.434	0.018	1.932
8.15	17.568	67.90	4.07	1.501	0.011	4.151
4.07	17.688	69.00	-4.07	1.491	0.002	-3.342
2.04	17.850	70.60	-2.04	1.477	0.004	-2.359
1.02	18.029	72.30	-1.02	1.463	0.010	-0.952

Table 3. Dispersion Results of CL Group Soil Sample taken from Kayışlı District (Mahmutluoğlu ve Tekinsoy, 2015)

Total Press. p (kg/cm^2)	Dry Unit Weight γ_k (gr/cm^3)	Dif. Coeff. $D_s \times 10^{-4}$ (cm^2/dk)	Disp. Vrb. x -	Disp. Flux J_s (gr/cm^2dk)	Dispers. Soil Amount ΔW_s (gr)	Total Comp. Soil ΔW_t (gr)
0.00	1.319	-	-	-	-	-

0.13	1.326	0.03515	13.984	2.307×10^{-92}	6.525×10^{-88}	0.0014
0.25	1.328	0.04878	11.847	3.287×10^{-68}	9.296×10^{-64}	0.0025
0.51	1.335	0.08318	9.026	2.851×10^{-42}	8.063×10^{-38}	0.0077
1.02	1.352	0.16392	6.349	6.191×10^{-24}	1.751×10^{-19}	0.0318
2.04	1.385	0.30751	4.526	6.908×10^{-15}	1.954×10^{-10}	0.1235
4.07	1.434	0.49223	3.454	7.904×10^{-11}	2.235×10^{-6}	0.3632
8.15	1.501	0.69471	2.777	1.009×10^{-8}	2.854×10^{-4}	0.8693
4.07	1.491	0.66726	2.853	0.609×10^{-8}	1.722×10^{-4}	0.7810
2.04	1.477	0.62911	2.965	0.283×10^{-8}	8.004×10^{-5}	0.6672
1.02	1.463	0.58548	3.105	0.107×10^{-8}	3.026×10^{-5}	0.5574

Note: Since consolidation stops at the end of each pressure increment, the time rate of settlement v_z was taken as $v_z=0$.

Table 4. Effective Stress Variations relative to Dry Unit Weights for the CH group Sample taken from Kayışlı District (Mahmutluoğlu ve Tekinsoy, 2015)

Total Press. p (kg/cm^2)	Samp. Height H (mm)	Void Ratio e (%)	Pressure Increment Δp (kg/cm^2)	Dry Unit Weight γ_k (gr/cm^3)	Coeff. Of Volume Comp. m_v (cm^2/kg)	Efective Stress Increment σ' (kg/cm^2)
0.00	20.000	96.2	-	1.284	-	-
0.13	19.970	95.9	0.13	1.286	0.012	0.130
0.25	19.801	94.3	0.13	1.297	0.067	0.127
0.51	19.578	92.1	0.25	1.312	0.046	0.250
1.02	19.278	89.1	0.51	1.333	0.030	0.529
2.04	18.825	84.7	1.02	1.364	0.023	1.000
4.07	18.197	78.5	2.04	1.412	0.017	2.034
8.15	17.448	71.2	4.07	1.472	0.010	4.162
4.07	17.536	72.0	-4.07	1.465	0.001	-4.767
2.04	17.592	72.6	-2.04	1.460	0.002	-1.709
1.02	17.700	73.6	-1.02	1.452	0.006	-0.916

Table 5. Dispersion Results of CH Group Soil Sample taken from Kayışlı District (Mahmutluoğlu ve Tekinsoy, 2015)

Total Pressure p (kg/cm^2)	Dry Unit Weight γ_k (gr/cm^3)	Dif. Coeff. $D_s\times10^{-4}$ (cm^2/dk)	Disp. Vrb. x -	Disp. Flux J_s (gr/cm^2dk)	Dispersive Soil Amount ΔW_s (gr)	Total Compacted Soil ΔW_t (gr)
0.00	1.284	-	-	-	-	-
0.13	1.286	0.1039	25.814	0	-	0.0001
0.25	1.297	0.6807	10.000	1.88×10^{-50}	5.32×10^{-46}	0.0051
0.51	1.312	1.4191	6.848	6.75×10^{-27}	1.91×10^{-22}	0.0232
1.02	1.333	2.3723	5.215	5.48×10^{-18}	1.55×10^{-13}	0.0695

2.04	1.364	3.7251	4.064	4.88×10^{-13}	1.38×10^{-8}	0.1846
4.07	1.412	5.4312	3.253	3.56×10^{-10}	1.01×10^{-5}	0.4533
8.15	1.472	7.2148	2.707	1.56×10^{-8}	4.41×10^{-4}	0.9423
4.07	1.465	7.0192	2.758	1.12×10^{-8}	3.17×10^{-4}	0.8759
2.04	1.460	6.8928	2.792	0.89×10^{-8}	2.52×10^{-4}	0.8324
1.02	1.452	6.6448	2.861	0.57×10^{-8}	1.61×10^{-4}	0.7589

Note: Since consolidation stops at the end of each pressure increment, the time rate of settlement v_z was taken as v_z=0.

The same calculations were performed in order to obtain both the consolidation and dispersion parameters of the CH group samples. On the other hand, dispersive and diffusive properties of CL and CH group samples and their comparisons were discussed by graphics and comments. As can be seen from Table 2 and Table 4, the effective stress increment values in the final columns which were found theoretically (σ′) are very close to the experimental counterparts (p) in the first columns both for CL and CH group soil samples. These theoretical values were reached by using Equation 4 below which is given for effective stresses and this equation, as mentioned previously, was obtained by solving the differential equation in Equation 3 (Tekinsoy 2013; Mahmutluoğlu 2014).

$$\sigma' = \frac{1}{m_v} \ln \frac{\gamma_{k2}}{\gamma_{k1}} \quad \text{((Mahmutluoğlu ve Tekinsoy, 2015))} \qquad (4)$$

where, m_v is the coefficient of volume compressibility, γ_{k1} and γ_{k2} are the initial and final dry unit weights for any pressure increment, respectively. The obtained values and graphics show the effectiveness of dry unit weight on effective stress variations in a soil. Comparison of effective stress variations obtained both theoretically and experimentally can be seen in the graphics given in Figure 1 and Figure 2 for CL and CH group soil samples, respectively.

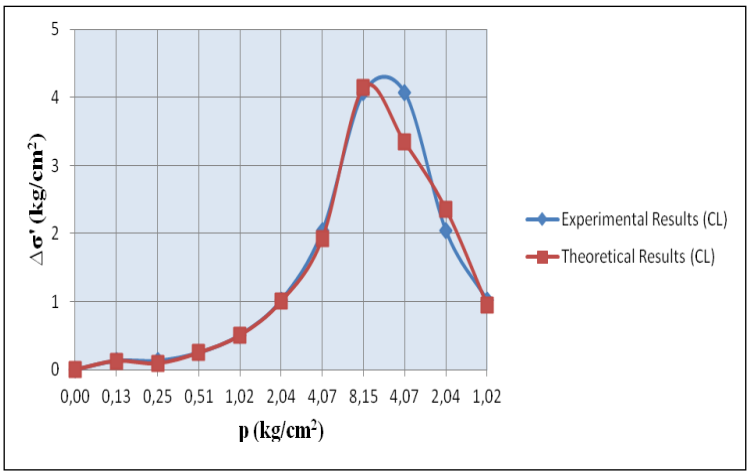

Figure 1. The Relationship between Theoretical (Δσ') and Experimental (p) Effective Stress Increments for CL Group Soil (Mahmutluoğlu ve Tekinsoy, 2015)

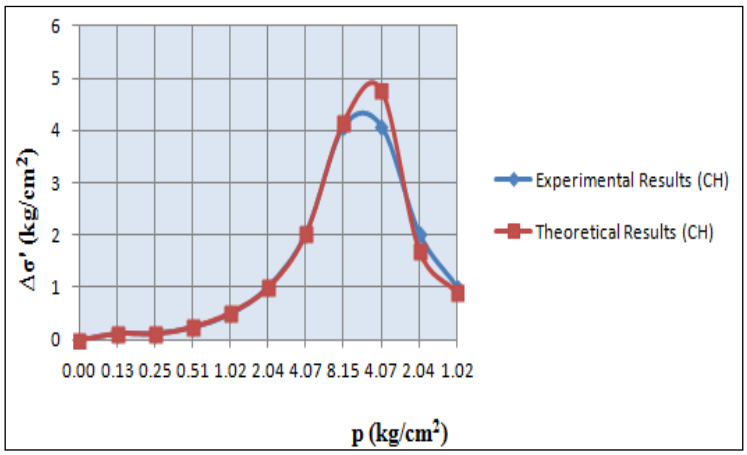

Figure 2. The Relationship between Theoretical (Δσ') and Experimental (p) Effective Stress Increments for CH Group Soil (Mahmutluoğlu ve Tekinsoy, 2015)

A similar relationship can be observed between theoretical and experimental effective stress increments for CH group soil sample, as well. Additionally, if Table 3 and Table 5 are considered, it can be seen that the values for diffusivity coefficients in column 3 for CL group sample are lower than that for CH group except for the first pressure increment value on which pre-consolidation pressure has an effect. These values were obtained by using the equation given below as Equation 5:

$$D_s = \frac{z^2}{4t} \ln \frac{z_i}{z} \qquad (5)$$

where, z_i ve z are the initial and any sample heights, respectively, $z^2/4$ is the squared power of the drainage path (z/2) and t is time.

The relationship between diffusivity coefficients of CL and CH group samples can be clearly seen from the graphic given in Figure 3 below:

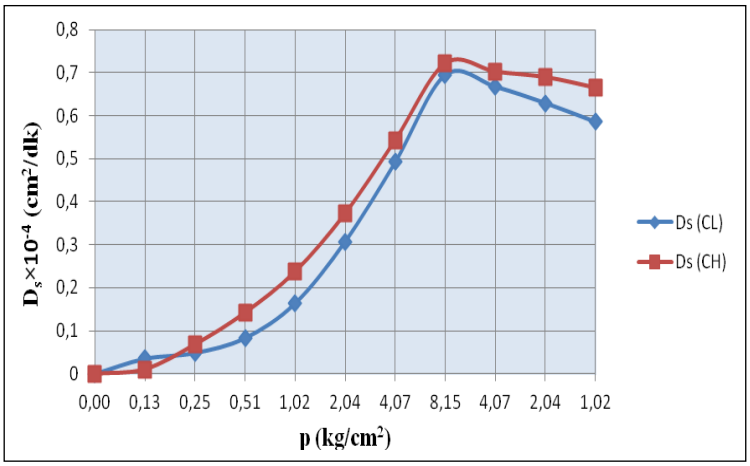

Figure 3. The Relationship of Diffusivity Coefficients ($Ds\times10^{-4}$) of CL and CH Group Samples relative to Pressure Increments (p) (Mahmutluoğlu ve Tekinsoy, 2015)

The values for flux (J_s) and dispersive variable (x) were found by using the equations below as Equation 6.a and Equation 6.b, respectively:

$$J_s = \sqrt{\frac{D_s}{\pi t}} \cdot \left(\gamma_{kf} - \gamma_{ki}\right) e^{-x^2} \quad (6.a)$$

$$x = \frac{z + v_z t}{2\sqrt{D_s t}} \quad (6.b)$$

where, D_s is the diffusivity coefficient, γ_{ki} and γ_{kf} are the initial and final values for dry unit weights, respectively, v_z is the time rate of settlement, z is sample height at any instant and t is time.

The occurrence of v_z in the equations includes the effects of time rates of settlement to the phenomena. The values for time rates of settlement can be obtained by using the equation below, theoretically:

$$v_z = \frac{z}{2t} \ln \frac{z}{z_i} \quad (7)$$

where, z_i and z are the initial and any sample deformation heights, respectively and t is time.

The amount of soil which fills into macro pores and diffuses inside the soil matrix were found by using Equation 8 below:

$$\Delta W_s = J_s A \Delta t \quad (8)$$

where, J_s is flux, A is the cross sectional area of the sample and t is time. Since variables of both time and location exist in Equation 8, the amount of dispersive soil can be obtained at any pressure increment or for any instant throughout a consolidation process.

In the last columns of Table 3 and Table 5, total compacted soil amounts (ΔW_t) are given for CL and CH group samples, respectively. These values were obtained by using Equation 9 below:

$$\Delta W_t = A \Delta z \Delta \gamma_k \quad (9)$$

where, A is the cross sectional area, z is the deformational height, γ_k is dry unit weight and this equation represents total compaction. If the total compacted amounts of the CL and CH group soil samples are compared, it can be seen that all of the values are larger in CH group except for the first value on which pre-consolidation pressure is effective. This relationship can be observed in the graphic given in Figure 4.

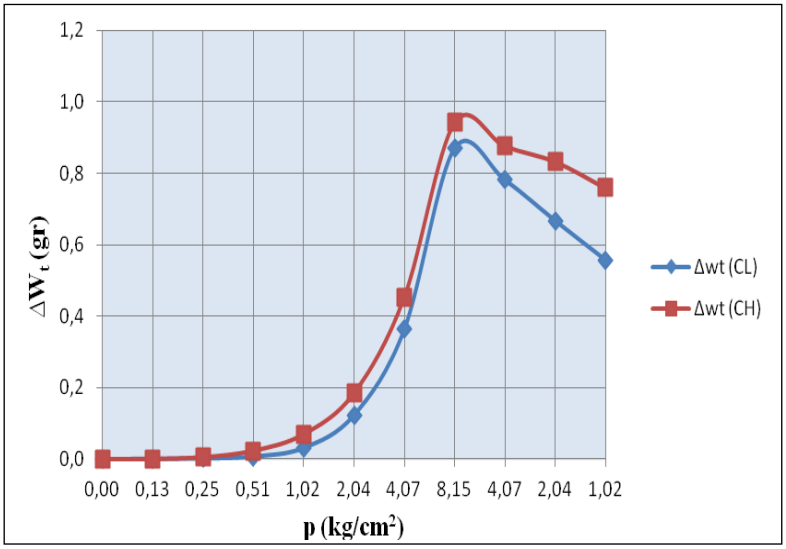

Figure 4. Total Compacted Soil Amounts (ΔW_t) for CL and CH Group Soil Samples with respect to Pressure Increments (p) (Mahmutluoğlu ve Tekinsoy, 2015)

As can be seen from the graphical relationship given in Figure 4, the total amount of compacted soil for CH group soil sample is greater than that for CL group throughout the consolidation process. Therefore, CH group soil sample is compacted more than CL group sample and more soil particles are transported, oriented and compacted in terms of grain diffusion and dispersion.

CONCLUSION

In this study, an approach is presented in which time rates of settlement and their effect on consolidation are studied in terms of dispersion and grain diffusion along with the effects of pore water pressure. A result of this study is that it enables to acknowledge information on the subjects of grain diffusion and dispersion in a consolidation phenomenon. In this aspect, values for variations in effective stresses, diffusivity coefficients, dispersive flux, dispersive and total compacted soil amounts were obtained by solving the differential equation given as Equation (3) being related to dispersion in terms of dry unit weight variations. This equation which was obtained theoretically gives results that are in a very close agreement to the experimental counterparts.

On the other hand, diffusive and dispersive characteristic of a specific region in Adana Turkey is studied and the effects of dry unit weight and plasticity are discussed to shed some light to the phenomena for the first time. By considering the phenomenon of consolidation in an aspect of hydrodynamic dispersion, a great deal of information can be obtained about time rates of settlement. Consequently, viscous properties of a soil could be considered as a result of using the presented theory. Viscous properties of soils are of great importance in the examination and solution of slope stability problems. Eventually, it can be pointed out that the presented theory enables a more clear understanding and perspective in the subject.

SPECIAL THANKS

For the valuable aid and support that was anabled during the experimental stages of the study, special thanks have been presented to the soil mechanics laboratory and staff of Mersin University.

REFERENCES

Özaydin, K. (2005). Zemin Mekaniği., Birsen Yayınevi, 165-167.

Battaglio, M., Bellomo, N., Bonzani, I., Lancellotta, R. (2003). Non-Linear Consolidation Models of Clay Which Change Type. Int. J. of Non-Linear Mechanics, 30, 493-500.

Geng, X., Xu, C., Cai, Y. (2006). Non-Linear Consolidation Analysis of Soil with Variable Compressibility and Permeability under Cyclic Loading. International Journal of Numerical Analysis Methods in Geomechanics, 30, 803-821.

Battaglio, M., Bonzani, I., Campolo, D. (2005). Non-Linear Consolidation Models of Clay with Time Dependent Drainage Properties. Mathematical and Computer Modelling. 42, 613-620.

Asch, W. J. V., Deimel, M. S., Haak, W. J. C. (1989). The Viscous Creep Component in Shallow Clayey Soil and the Influence of Tree Load on Creep Rates. Special Issue: Proceedings of the Fourth Benelux Colloquium on Geomorphological Processes IGU-COMTAG Meeting, 14, 557-564.

Culling, W. E. H. (1963). Soil Creep and the Development of Hillside Slopes. The Journal of Geology, 71-2, 127-161.

Tekinsoy, M. A. (2013). Theoretical Soil Mechanics, Soil Behavior in K_0 Condition. DaisyScience International Publishing House, 125-126; 334-340.

Nielsen, D. R., Jackson, R .D., Cary, J. W., Evans, D. D. (1972). Soil Water. American Society of Agronomy, Soil Science Society of America, 31-39.

Mahmutluoğlu, B., (2014). Hidrodinamik Dispersiyonun Konsolidasyona Olan Etkisi. PhD Thesis, Çukurova University Institution of Natural and Applied Sciences, Adana, 268.

Mahmutluoğlu, B. Tekinsoy, M. A. (2015), Hidrodinamik Dispersiyon' un Konsolidasyona Olan Etkisi, Çukurova Üniversitesi Fen ve Mühendislik Bilimleri Dergisi, Cilt:32/3.

PITTING CORROSION BEHAVIOUR OF ST 37 STRUCTURAL STEEL IN SEVERAL CORROSIVE ENVIRONMENTS

Taha Yasin EKEN
Ankara Yildirim Beyazit University
Materials Engineering Department
tahayasineken@gmail.com

Kafiye KARDELEN
DSI (Devlet Su Isleri)
kafiyekardelen@gmail.com

Nuray CELEBI
Ankara Yildirim Beyazit University
Materials Engineering Department
ncelebi@ybu.edu.tr

Mehmet Fatih OKTEM
Ankara Yildirim Beyazit University
Materials Engineering Department
fatihoktem@hotmail.com

ABSTRACT: St37 is constructional steel having maximum 0.17 % carbon ratio, and its fracture strength is between 360-510 MPa. It is used to increase the mechanical properties as rebar material in composite concrete systems. Pitting corrosion is one of the most dangerous detrimental mechanisms for the reinforcing rebar because it is widespread, difficult to control and it has degrading effects in the material. For these reasons, the pitting corrosion behavior of St37 is investigated with respect to the salinity rate of the Black Sea and the Mediterranean Sea to observe the influence of salt to the reinforcing rebars of buildings used in these regions. Several standards such as EN, ASTM or ISO could be used for the pitting corrosion experiments but the authors have decided to develop their own procedure to become as standard protocol for this research. Cutting from plate, St37 dogbone specimens are prepared two for pristine, two for 3.5 % NaCl solution and two for 1.8 % NaCl solution and they are sanded with sandpapers to obtain clean surfaces. To observe corrosion distinctly and giving ID numbers to the pits, the corrosion exposed area is adjusted to 1 mm^2 and the rest of the specimens are painted with nail polish. 1.8 % and 3.5 % are the salinity rates of the Black Sea and the Mediterranean Sea respectively, two different solutions are prepared and the dogbone specimens are immersed into these solutions based on the determined corrosion protocols. Pre-corroded specimens are then investigated under optical microscope to identify and measure the corrosion pits and these specimens are put to tensile test to obtain the stress-strain curves of the same specimens. The surfaces of the specimens are characterized by using Scanning Electron Microscope (SEM) to identify where the fracture originated from. The %3.5

salinity rate results more pits on the surface, deeper pits from the surface and the 1.8 % salinity rate results less pits on the surface and shallower from the surface. Moreover, it is observed that increase in salinity rate decrease the mechanical properties after tensile testing results.

Key words: Construction, Steel, Salinity, Pitting Corrosion

INTRODUCTION

Due to the low cost and availability of materials, steel-reinforced concrete composites are the most commonly used structural materials. The most important parts of these composite systems are reinforced steel rebars because of their load carrying capabilities. The steel is selected from structural steels and the most used one is St37. In this paper, pitting morphology and mechanical strength of St37 steel is investigated with respect to the salinity rate of the solution. The mechanical properties of steel rebars are strong, but the service problems influence negatively to the permanency of them. For example, due to the wear of concrete, steel rebars may contact with air and they can corrode. Similarly, storing of steel rebars for a long time may result corrosion before servicing of them. According to the ASTM, chemical or electrochemical reaction between a metal and its environment produces a deterioration of material and its properties and this is called corrosion [1]. Pitting corrosion is localized accelerated dissolution of the metal which occurs result of a breakdown of the protective passive film on the metal surface. The metal is not corroded uniformly, but deep pits are produced and these pits reduce the surface area and enhance the stress concentration. The most destructive environments for the pitting corrosion of the structural steels are coastal areas because the structures are subjected to extreme exposure to saline water and this results intrinsic tensions and crackings [2-4]. However, due to the high alkaline properties and passive film layer on metal surface, reinforced steel can bear to the corrosion for a long time. Furthermore, a well pressed concrete has lower permeability and the compounds which are the reason of the corrosion (oxygen, water and chloride) cannot penetrate into the concrete and so cannot reach to the rebars. When the alkalinity level starts to decrease, the material is exposed to the corrosive environment in a higher degree.

The corrosion pits decrease the effective area of the surface that sustain the loads and due to the stress concentration at the bottom of the pits, the cracks will possibly form from these regions. The volume of the corroded rebar expands and makes the reason for the parallel cracks on the rebars inside the concrete. Once these cracks and voids form, concrete is more exposed to atmospheric conditions and the structural member complete its life very rapidly [5-7].

The most important reason of the corrosion of the steel rebar is the penetration of the chloride ions to the concrete. The chloride ions can penetrate to the concrete with the salt inside the sea water or the salt that concrete contains. Although the material loss is very low comparing to the other homogenous corrosion types, the parts of the material may become unusable very rapidly. The pitting corrosion is one the most

dangerous corrosion types because detection and prediction of it is very difficult [8-10].

The main purpose of this work is to analyze the effect of the salinity to the corrosion formation of St37 metal.

In the scope of this research project, some specimens are subjected to NaCl solutions with different concentration levels and some pristine specimens are used for comparison reason. The solutions used in this study include 1,8 % NaCl concentration and 3.5 % NaCl concentration respectively. The 1,8 % NaCl concentration represents the salinity rate of Black Sea and the 3.5 % NaCl concentration represents the salinity rate of Mediterranean Sea. After specimens immersed to the solutions, the specimens are taken out to investigate pitting morphology of them. Then, tensile tests are applied to compare the strength of the pre-corroded specimens with the pristine specimens. Lastly, fractured specimens are observed under Scanning Electron Microscope (SEM) to detect the crack initiation points.

METHODS

General Design Considerations

To make this research some standards are obtained such as TS 5731 EN ISO 8044 (corrosion of metals and alloys - basic terms and definitions), TS EN ISO 11130 (corrosion of metals and alloys - alternate immersion test in salt solution), TS EN ISO 11463 (corrosion of metals and alloys - evaluation of pitting corrosion) and TS ISO 11845 (corrosion of metals and alloys- general principles for corrosion testing). However, in this research in house developed protocols have become standards benefitting from these international standards with the decision of the authors to develop their own procedure for the time and labor savings. Therefore, the corrosion procedure of this study was developed by the master students and assistant professors at the Ankara Yildirim Beyazit University Department of Materials Engineering.

St 37 sheet metal was obtained and cut according to the ASTM standards as dogbone specimen shape. Then, the specimens were sanded with sandpapers 120,240,400 and 800 meshes to get smooth surface. After that, they were cleaned with the acetone in the ultrasonic cleaner and designated with ID numbers. In figure 1 (a), the sanded then ultrasonic bathed specimens are showed. The designations of the specimens with the ID numbers are illustrated in figure 1 (b). Some pilot tests were done before the final protocol was established. Six specimens were used firstly, two for 1.8 % salinity rate, two for 3.5% salinity rate and two specimens as pristine. Two pristine specimens were machined and put to the tensile test to compare the mechanical strength with the pre-corroded specimens. The weight of other four specimens was measured to observe the corrosion effect on weights. The specimens were measured

with caliper and 1 mm^2 areas were marked at the center of the specimens, representatively showed in figure 2. Except the 1 mm^2 center, the cleaned specimens were applied nail polish.

The reason is to have the corrosion only at the center for examining easily. Oktem [3] and Frantziskonis et al. [11], used the nail polish for the pitting corrosion detection, they made an area which was corroded and remain parts were polished. This shows that nail polish is used in scientific studies to protect the material from corrosion. Polish was applied three layers with 20 minutes drying periods. Drying of the specimens is illustrated in figure 3. Afterward, the solutions were prepared with the precision scales. To immerse four specimens in different beakers, four solutions were prepared, two of them with 3.5 % NaCl and the other two with 1.8 % NaCl. The solutions with 3.5 % NaCl were prepared using 250 ml of distilled water with 15 % H_2O_2 (hydrogen peroxide). The solutions with 1.8 % NaCl were prepared using 250 ml of distilled water with 15 % H_2O_2. The solution pH could change with the specimen corrosion. Hence, the pH values of the solutions were measured before the specimens were immersed.

Next, the specimens were immersed to these solutions 15 minutes periods, after each period the specimens were observed with optical microscope and the process was repeated three times. The immersion procedure and the corroded area are showed in figure 4. End of the process, the pH values of solutions were measured. Then, the specimens put to the ultrasonic cleaner and the nail polish was removed from the specimens. The weight of each cleaned specimen was measured after process. Cleaned four specimens observed with optical microscope. After the solution process, four corroded specimens and two pristine specimens were applied tensile test. Tensile test was applied to them with 2500 N capacity, 0.1 N precision calibrated universal tester. The specimens were pulled with 1 mm/min velocity and the data were recorded. Then, the four fractured specimens were investigated with Scanning Electron Microscope. The relation between the pits and the fracture points were examined by this way. A summary for the experimental procedure is showed in table 1.

Table 1. A Summary of the Experimental Procedure in This Study.

Experiments	Specimen ID	Explanations
Pit Morphology Observation-1	1.8 ID 1	Pitting Morphologies Observed with Optical Microscope in the First Part of The Study.
	1.8 ID 2	
	3.5 ID 1	
	3.5 ID 2	
Tensile Test	PS ID 1	Four Corroded and Two Pristine Specimens were
	PS ID 2	

	1.8 ID 1	Applied Tensile Tests. The Reason is to Investigate The Effect of Corrosion to the Strength.
	1.8 ID 2	
	3.5 ID 1	
	3.5 ID 2	
Scanning Electron Microscope Observation	1.8 ID 1	Four Corroded Specimens were Observed with Scanning Electron Microscope. The reason is to Investigate the Relation of Fracture Points with the Pits.
	1.8 ID 2	
	3.5 ID 1	
	3.5 ID 2	

In table 1, specimen ID designations and experiments with explanations are given. According to the table 1, the 1.8 ID 1 and 1.8 ID 2 are the specimens immersed to 1.8 % NaCl solution and 3.5 ID 1 and 3.5 ID 2 specimens are the specimens immersed to 3.5 % NaCl solution. The PS ID 1 and PS ID 2 specimens are the pristine specimens for tensile test comparisons.

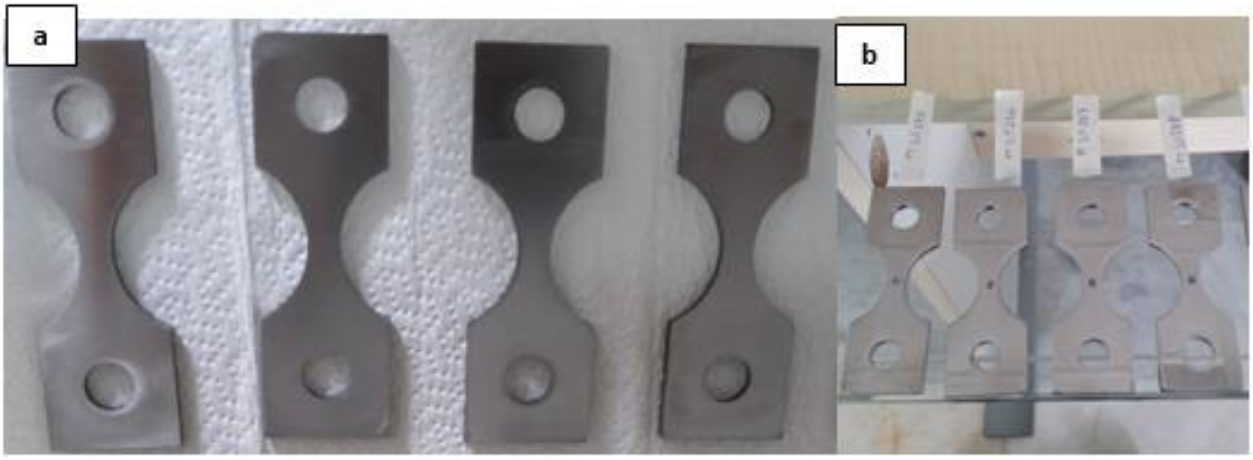

Figure 1. (a) Sanded and Ultrasonic Bathed Specimens (b) ID Numbered Specimens For 3.5 % Salinity Rate Solution

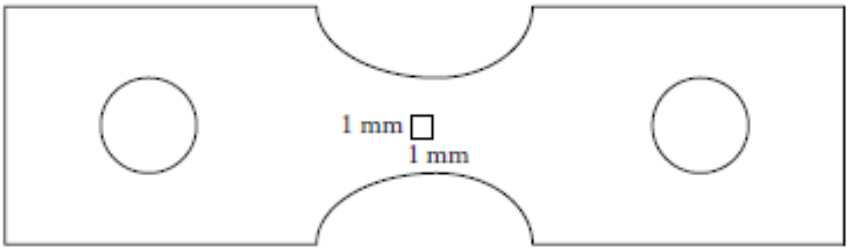

Figure 2. Representative Schematic Specimen and 1 mm² Area at the Center

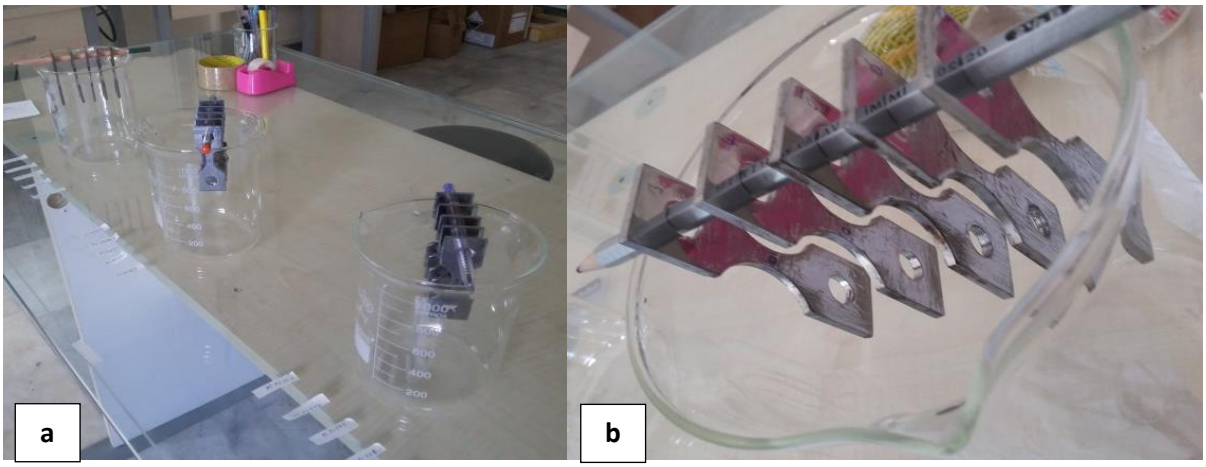

Figure 3. (a) Polished With Nail Polish and Dried Specimens (b) Zoom in Image

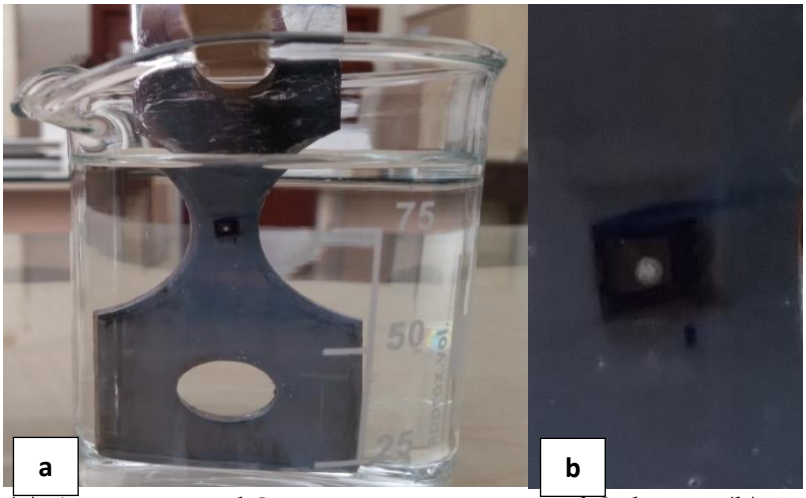

Figure 4. (a) An Immersed Specimen in a Prepared Solution (b) Zoom of the Corroded Area

RESULTS AND FINDINGS

Effect of Pitting Corrosion on Weight

The effects of the pitting corrosion on the reinforced steel St37 are investigated and experiments explained in the methods. The pitting corrosion is a localized corrosion and they are seen on the optical microscope as small hollows. These hollows are progressed to vertical direction to the material inside. Pitting corrosion can propagate until out of service and it may not be even noticed. As mentioned in methods section, there were only four specimens for solutions and two specimens for pristine. For these four specimens material loss was investigated. The table 2 shows

this material loss study. According to the table 2, the material loss is almost zero, which means very low material loss, was observed. Thus, there is no possibility to comment this result for pitting corrosion formation. Angst et al. [12] made the weight loss in their article and they also stated that to detect the mass difference, a significant amount of pitting corrosion should be already taken place.

Table 2. Material Losses of Specimens as Percentage

Specimen	% Loss
1.8 ID 1	0,0009
1.8 ID 2	0,0006
3.5 ID 1	0,0006
3.5 ID 2	0,0025

Effect of Pitting Corrosion on Solution pH

One of another factor that can affect the pitting corrosion is the pH value. The change of the pH value was also investigated in this study. The structural metal St37 was immersed to the solutions and pH value difference of the solutions were observed after the specimens were corroded. In table 3, the pH values are illustrated and according to this table there is no significant change of the pH values. Glass et al. [13] have reported that the inhibitive properties of the concrete cannot be expressed only by the OH^- concentration because also a lot of other factors such as alkaline reserves affect to the concrete. Moreover, Page et al. [14] also stated that the chloride relation with pH is not a reliable parameter since the effect of the other factors may change the pH. Hence, the pH change may not be a significant parameter on the pitting corrosion. However, the reason of the little change may be the short immersion time of specimens.

Table 3. pH Change of Specimens Before and After Corrosion

Specimen	Before Corrosion	After Corrosion
1.8 ID 1	3,94	3,92
1.8 ID 2	3,94	4,00
3.5 ID 1	3,97	4,03
3.5 ID 2	3,97	4,02

Pitting Morphology Observations

After specimens immersed to the solutions, they were taken out each 15 minutes period. They were observed under optical microscope whether pits occurred or not. Then, for each period images were captured until the specimens cleaned with acetone. Lastly, the cleaned specimens again observed with optical microscope to detect whether the pits continued or not. Hence, the pitting morphology figures include the pits at 15 minutes, 30 minutes, and 45 minutes and cleaned with acetone. They were zoomed to a pit and the growing of this pit was observed.

From figure 5 to figure 8 shows the pit morphologies of the specimens used in this study. Each 15 minutes the pits in the corroded area grows. These figures cropped from the whole images to show the pits only. Especially pits grow with first 15 minutes for all specimens. However, after first 15 minutes the depths of pits increase instead of the size of them. This means that the sizes of the pits are almost same after 15 minutes. In addition, the pits are tending to be more circular.

The size of the pit in figure 5 (a) is 7096 μm^2, in figure 5 (b) is 10752 μm^2, in figure 5 (c) is 12584 μm^2 and in figure 5 (d) is 11650 μm^2. The reason of decrease in figure 5 (d) is due to the acetone addition.

The size of the pit in figure 6 (a) is 12150 μm^2, in figure 6 (b) is 12520 μm^2, in figure 6 (c) is 12864 μm^2 and in figure 6 (d) is 13650 μm^2. Thus, the size of pit increases with time.
The size of the pit in figure 7 (a) is 6315 μm^2, in figure 7 (b) is 7562 μm^2, in figure 7 (c) is 8624 μm^2 and in figure 7 (d) is 9150 μm^2. In this pit, these size belong figure 7 (a). Figure 7 (b), figure 7 (c) and figure 7(d) has two more circular pits. This shows that these two new pits were formed and they were grown.

The size of the pits in figure 8 (a) is 8132 μm^2, in figure 8 (b) is 9545 μm^2, in figure 8 (c) is 10584 μm^2 and in figure 8 (d) is 10225 μm^2. The reason of decrease in figure 8 (d) is due to the acetone addition. In this figure there is more than one pit.

Specimen 1.8 ID 1

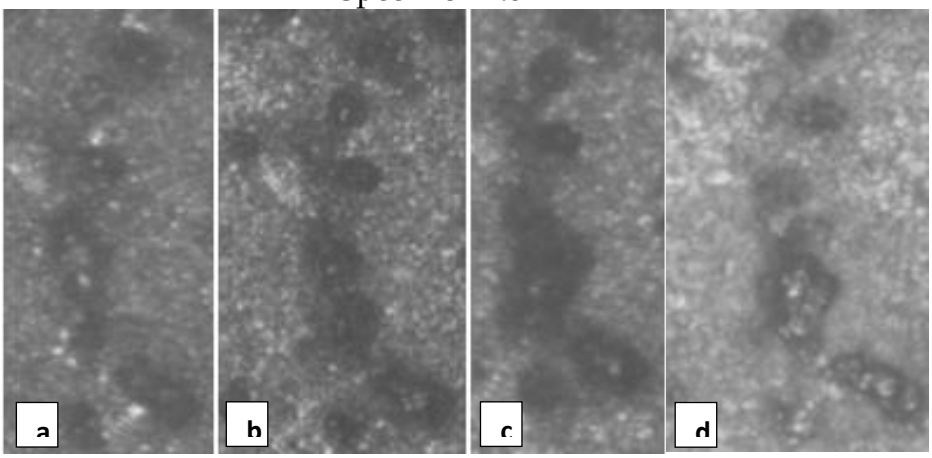

Figure 5. The Change in the Pit Morphology of Specimen 1.8 ID 1 at (a) 15 min. (b) 30 min. (c) 45 min. (d) Cleaned with Acetone

Specimen 1.8 ID 2

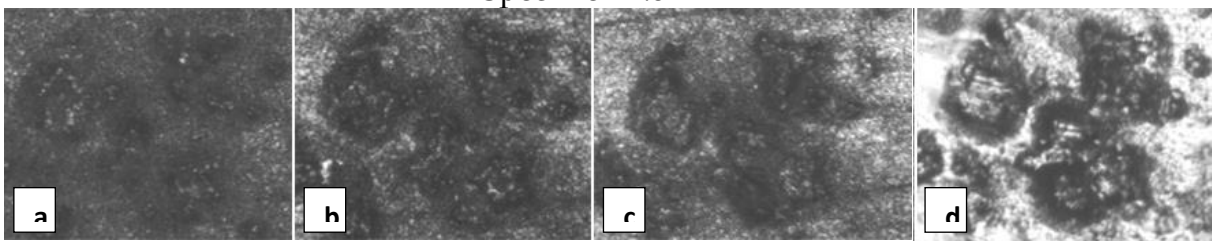

Figure 6. The Change in the Pit Morphology of Specimen 1.8 ID 2 at (a) 15 min. (b) 30 min. (c) 45 min. (d) Cleaned with Acetone

Specimen 3.5 ID 1

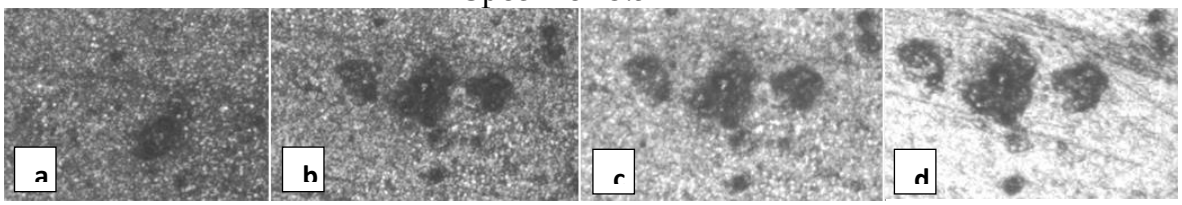

Figure 7. The Change in the Pit Morphology of Specimen 3.5 ID 1 at (a) 15 min. (b) 30 min. (c) 45 min. (d) Cleaned with Acetone

Specimen 3.5 ID 2

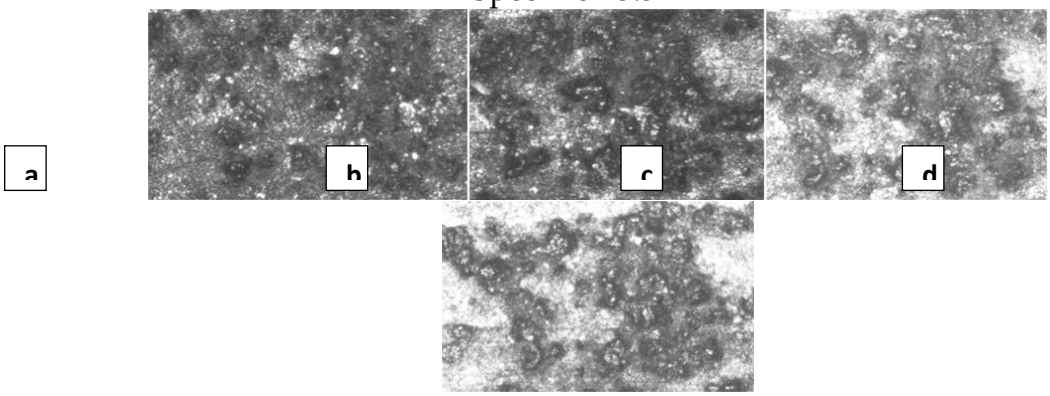

Figure 8. The Change in the Pit Morphology of Specimen 3.5 ID 2 at (a) 15 min. (b) 30 min. (c) 45 min. (d) Cleaned with Acetone

Tensile Test Results

Tensile test is used to observe the durability of the material under static forces and other mechanical properties. The studies shows that the tensile test applied on metallic materials, the physical detriments such as scratches or cracks of the materials affect negatively the strength. The maximum tensions concentrate to the small thicknesses, the notches or holes that locate on the materials; this is valid for the St 37 metal. [15]

From figure 9 to figure 14 are the tensile test graphs and the results of the tensile tests are showed in table 4. According to the results, the specimens immersed to the 1.8 % NaCl solution showed higher strength than the specimens immersed to the 3.5 % NaCl solution as expected. The reason of this result is that the specimens immersed to the 1.8 % solution have lower number of pits on their surfaces after they were corroded and the pits were formed on surface, they were not deep. In other words,

the specimens immersed to 3.5% solution have deeper pits and this result decrease the strength of them. Furthermore, strain rates are close to each other and this is unexpected. The reason may be the increase of brittleness in the material because of test conditions or a fault in the test machine about placing the specimen or measuring the strain of it. Nakai et al. [16] stated that increase pitting corrosion decrease the tensile strength and total elongation drastically. The results of pristine specimens are between the literature intervals and they are enough to compare.

Table 4. Results of the Tensile Tests

Specimen	Tensile Strength [N/mm²]	Fracture Strength [N]	Strain Rate [%]
PS ID 1	486,28	6291,5	26,7
PS ID 2	521,60	6853,4	25,8
1,8 ID 1	483,14	6389,7	26,3
1,8 ID 2	513,64	6275,5	26,0
3,5 ID 1	470,64	6227,6	25,8
3,5 ID 2	435,64	5982,9	26,5

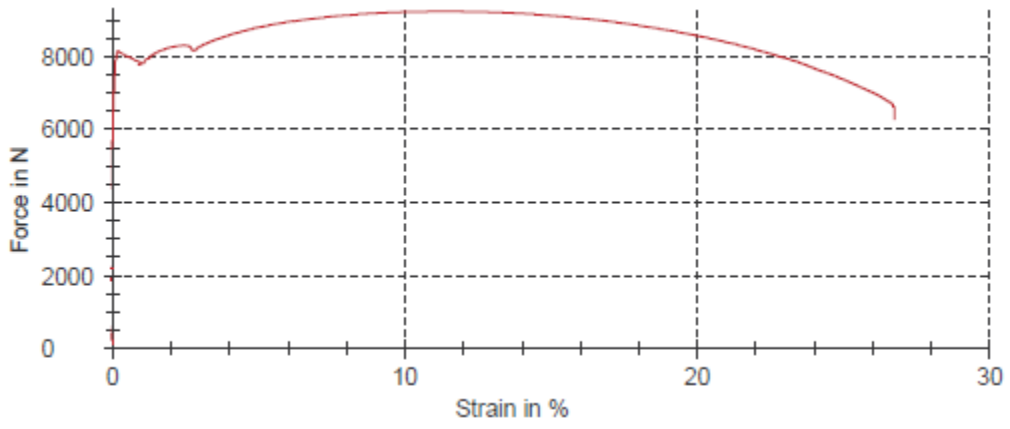

Figure 9. The Tensile Test Graph of PS ID 1 as Force (N) to Strain (%).

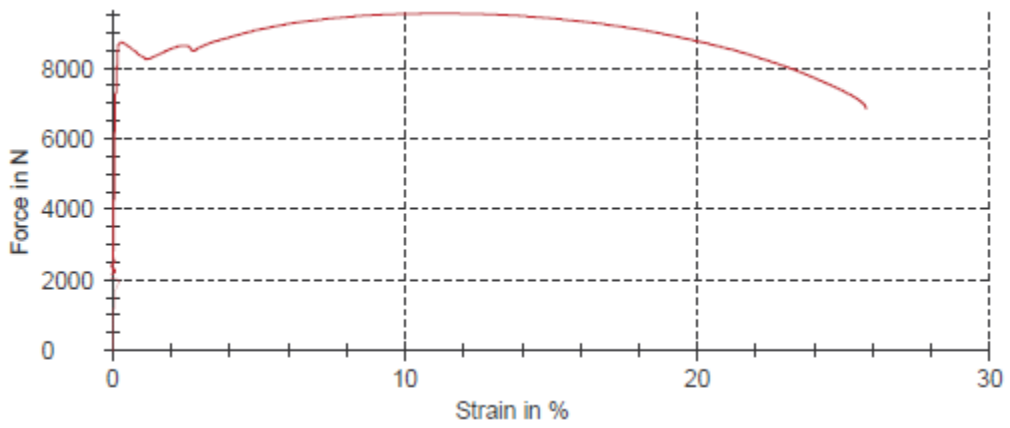

Figure 10. The Tensile Test Graph of PS ID 2 as Force (N) to Strain (%).

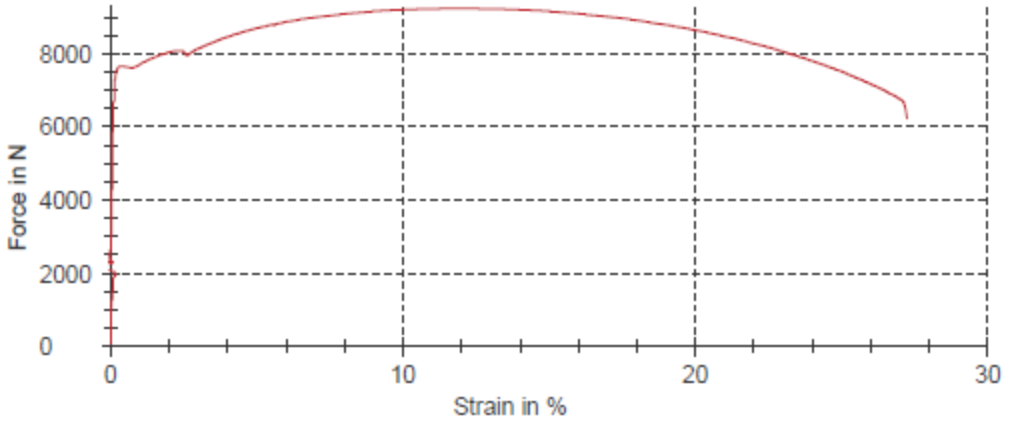

Figure 11. The Tensile Test Graph of 1.8 ID 1 as Force (N) to Strain (%).

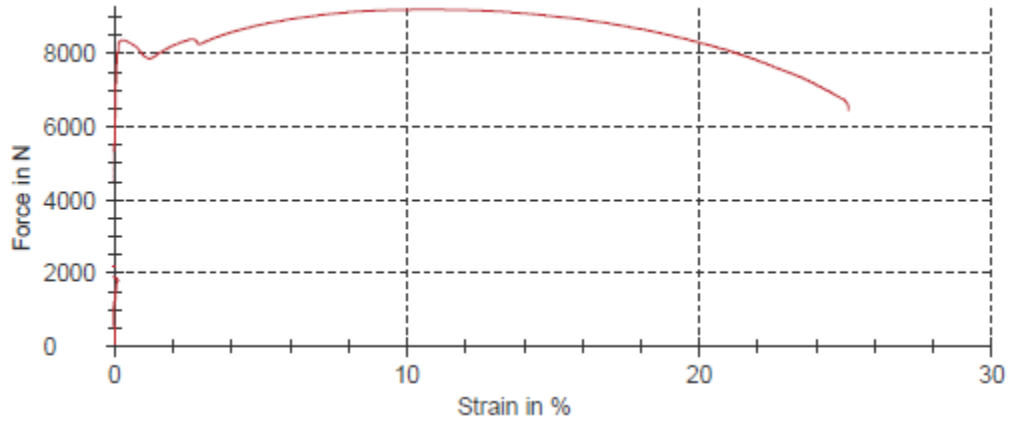

Figure 12. The Tensile Test Graph of 1.8 ID 2 as Force (N) to Strain (%).

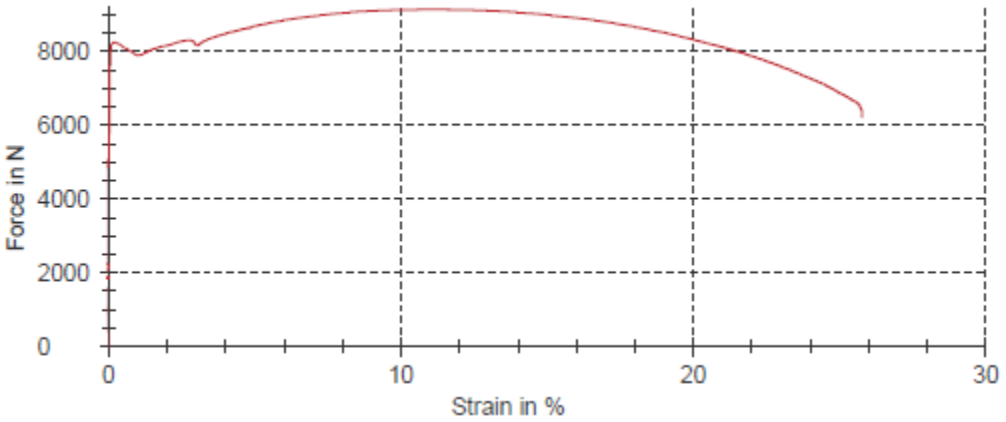

Figure 13. The Tensile Test Graph of 3.5 ID 1 as Force (N) to Strain (%).

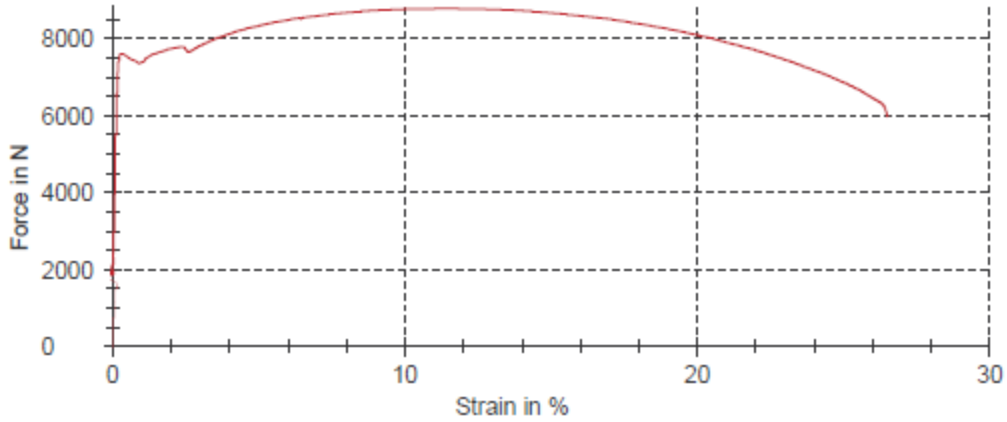

Figure 14. The Tensile Test Graph of 3.5 ID 2 as Force (N) to Strain (%).

Scanning Electron Microscope (SEM) Results

When we observe the images of the Scanning Electron Microscope, the specimens immersed to the 3.5 % NaCl solution have corroded pits wider area on the surface than the specimens immersed to the 1.8 % NaCl solution. Moreover, in cross-sectional view of the specimens immersed to 3.5% NaCl solution have deeper pits than the specimens immersed to the 1.8 % NaCl solution. The figure 15 shows the pits on the surface and the figure 16 shows the pits on cross-section to detect the depth of them.

However, the corroded pits were formed in a narrower area for the specimens immersed to 1.8 % NaCl solution. Moreover, they did not propagate along cross-section. When Fong Yuan Ma [9] observed in his study the corrosive effects of chloride on metals, he also used the Scanning Electron Microscope to determine the pitting corrosions.

In this study, the purpose of using the Scanning Electron Microscope is to determine whether the fractures started from the pits or not.

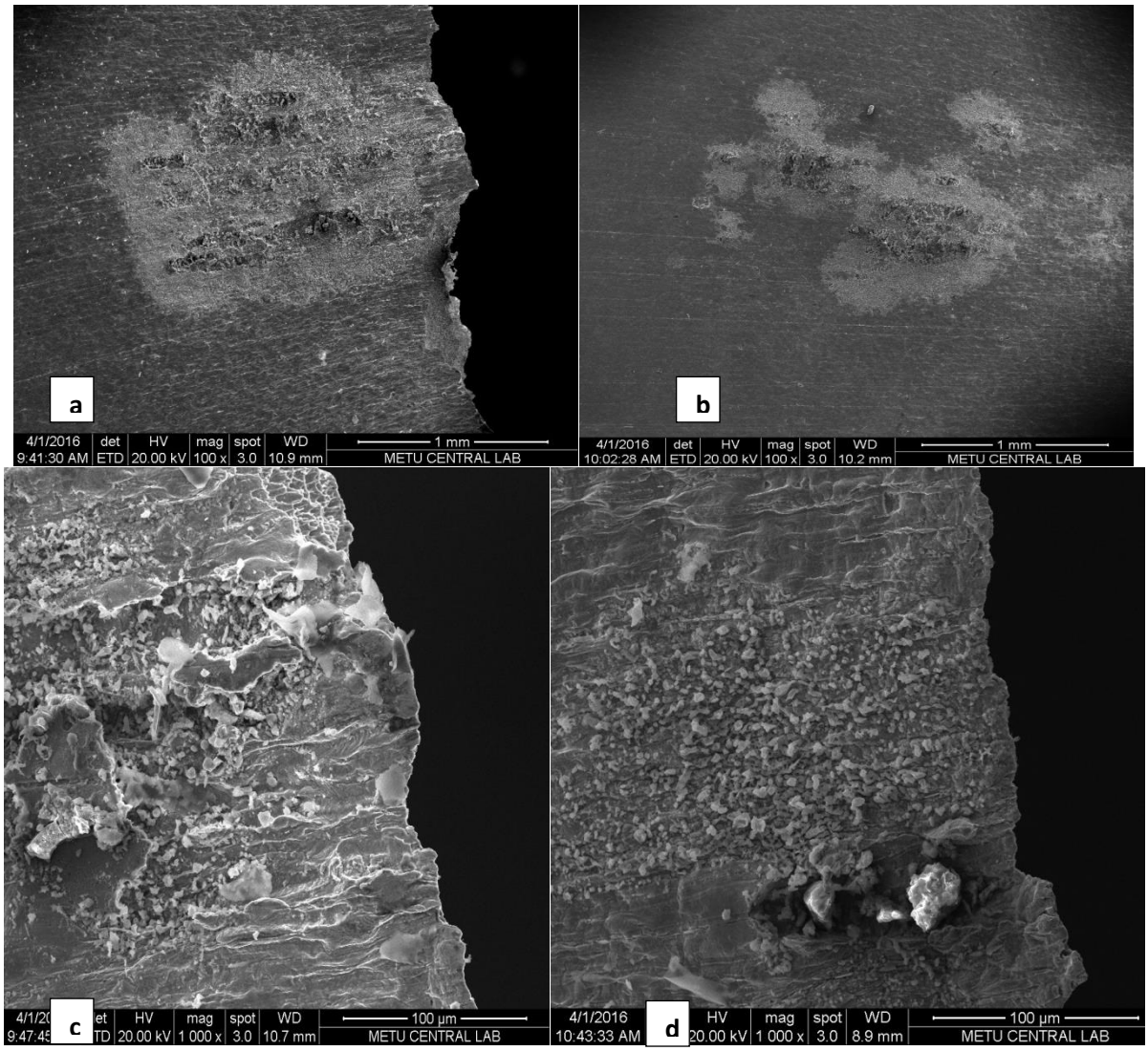

Figure 15. From Surface View SEM Micrographs Of Specimens Immersed to the (a)&(c) 3.5 % NaCl and (b)&(d) 1.8 % NaCl solutions

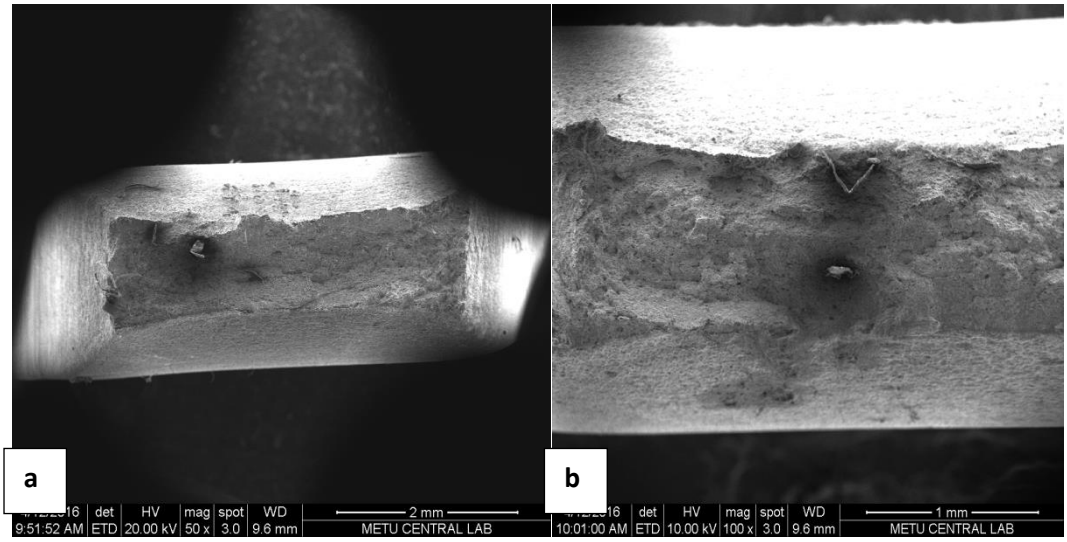

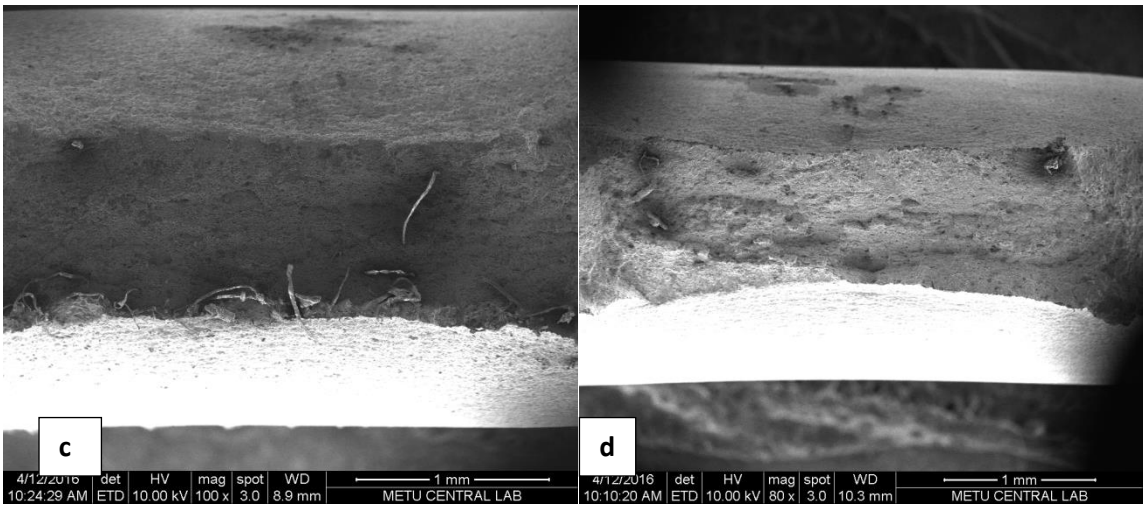

Figure 16. From Cross-Sectional View SEM Micrographs Of Specimens Immersed to the (a)&(b) 3.5 % NaCl and (c)&(d) 1.8 % NaCl solutions

CONCLUSIONS

Pitting corrosion behavior of structural steel St37 with several corrosive environments have been investigated in this study. Mainly, the effects of salinity rates are observed using two different solutions. According to this study, to detect the weight difference, a significant amount of pitting corrosion should be occurred. Thus, the weight of specimens did not change enough. The pH of solution did not change with specimen immersion.

The reason may be the short time immersion of the specimens. The corrosion pits form firstly circular and then they grow on surface with 15 minutes in the solution. After 15 minutes, the pits tend to be deeper, but the size of them tends to be stable. The tensile test results are decrease with increase of salinity as expected. Hence, the more the salinity rate the less the tensile strength of the St37 metal. Scanning electron microscope results show that the more the salinity rate, the deeper the corrosion pits. Also, the more the salinity rate means the more the surface corrosion pits.

RECOMMENDATIONS

The metal St 37, used for several structures, was investigated according to the corrosion resistance with experiments and to determine the most suitable environmental conditions was the main purpose. This purpose was tried to explain with some studies and supported with literature searches. Thus, selecting the material and environment conditions properly causes to increase the lifetime that results to decrease the effect of corrosion to the structural metals. Therefore, these precautions will contribute to the national economy. Similarly, avoiding the expensive repairs, economy can make savings from the labor force. To investigate pitting corrosion resistance, more specimens should be used; the pitting morphology of these specimens should be observed carefully. The depth of the pits should be

measured separately. The relation of these pits and the fracture points should be evaluated with scanning electron microscope. To sum up, how the pitting corrosion can be prevented or how the lifetime of the structural reinforced bars can increase should be studied.

ACKNOWLEDGEMENTS

This study is supported by Ankara Yildirim Beyazit University Office of Scientific Research (BAP). This study will continue with concentration on pitting corrosion with regard to salinity rate.

REFERENCES

[1] "ASTM G15-99b: Standard Terminology Relating to Corrosion and CorrosionTesting", 1999, ASTM, Philadelphia.

[2] Frankel, G. S. (1998). Pitting Corrosion of Metals. Corrosion, 145(6), 2186–2198.

[3] Oktem, M. F. (2005). Pit Morphology and Effect of Prior Pitting Corrosion on Fatigue, (May).

[4] Mohamed, N., Boulfiza, M., & Evitts, R. (2013). Corrosion of carbon steel and corrosion-resistant rebars in concrete structures under chloride ion attack. Journal of Materials Engineering and Performance, 22(3), 787–795.

[5] Zhao, Y., & Jin, W. (2016). Damage Analysis and Cracking Model of Reinforced Concrete Structures with Rebar Corrosion. Steel Corrosion-Induced Concrete Cracking, 55–77.

[6] Shi, X., Xie, N., Fortune, K., & Gong, J. (2012). Durability of steel reinforced concrete in chloride environments: An overview. Construction and Building Materials, 30, 125–138.

[7] Ann, K. Y., & Song, H. W. (2007). Chloride threshold level for corrosion of steel in concrete. Corrosion Science, 49(11), 4113–4133.

[8] Thomas, M. (1996). Chloride thresholds in marine concrete. Cement and Concrete Research, 26(4), 513–519.

[9] Ma, F. (2012). Corrosive Effects of Chlorides on Metals. Pitting Corrosion, 139–178.

[10] Kolotyrkin, J. (1963). Pitting corrosion of metals. Corrosion. Retrieved from http://www.corrosionjournal.org/doi/pdf/10.5006/0010-9312-19.8.261.

[11] Frantziskonis, G. N., Simon, L. B., Woo, J., & Matikas, T. E. (2000). Multiscale characterization of pitting corrosion and application to an aluminum alloy. European Journal of Mechanics, A/Solids, 19(2), 309–318.

[12] Angst, U., Elsener, B., Larsen, C. K., & Vennesland, Ø. (2009). Critical chloride content in reinforced concrete - A review. Cement and Concrete Research, 39(12), 1122–1138.

[13] Glass, G. K., & Buenfeld, N. R. (1997). The presentation of the chloride threshold level for corrosion of steel in concrete. Corrosion Science, 39(5), 1001–1013.

[14] Page, C. L., & Havdahl, J. (1985). Electrochemical monitoring of corrosion of steel in microsilica cement pastes. Materials and Structures, 18(1), 41–47.

[15] Souza, J. B. de, & Deus, E. P. de. (2014). Damage Mechanics Applied for Steel Reinforcements in Concrete Structures under Corrosion. Procedia Materials Science, 3, 2000–2005.

[16] Nakai, T., Matsushita, H., & Yamamoto, N. (2004). Effect of pitting corrosion on local strength of hold frames of bulk carriers (2nd Report) - Lateral-distortional buckling and local face buckling. Marine Structures, 17(8), 612–641.

OPTIMIZATION OF SPACING BETWEEN STAGGERED METAL HYDRIDE TANKS INTEGRATED FUEL CELL SYSTEM

İsmail HİLALİ
Harran University
ihilali@harran.edu.tr

Refet KARADAĞ
Harran University
refetkaradag@yahoo.com

Hüsamettin BULUT
Harran University
hbulut@harran.edu.tr

ABSTRACT: The sufficient hydrogen flow for requirements depends not only on the quantity contained in the metal hydride tanks, but also on other dynamic factors such as the ambient conditions, metal hydride kinetics and heat transfer mechanisms. In this study, the effects of dynamic factors on optimum spacing between metal hydride (MH) Hydrogen storage tanks are researched theoretically. A new approaching is presented for defining the optimum spacing between tanks according to different operating conditions. As MH alloys, AB5 type alloy (LaNi5) is selected. The analysis takes into account the effect of dynamic factors. The spacing is calculated by maximizing the heat transfer by means of accurate correlations. The results show that there exists an optimum spacing between the MH tanks for which the heat transfer is maximum and it should be considered to size the MH-Fuel cell system without extra cost.

Keywords: Hydrogen Storage, Metal Hydrides, Forced Convection

INTRODUCTION

Hydrogen storage systems must be efficient in order to show advantages of fuel cells. The hydrogen storage methods are generally classified into compression, liquefaction, metal hydride. Metal hydride is regarded as more convenient than the other Hydrogen storage methods. It has the advantages of safety, hydrogen storage capacity and reliability. Metal hydride process involves exothermic and endothermic reactions according to charging/discharging and requires thermal management for controlling process temperatures and enhancing process efficiencies. Thermal management is important for effective using of Hydrogen in Metal Hydride tanks. To supply sufficient hydrogen from tank to fuel cell system, the heat transfer capability has to be improved. Because thermal poorness is a serious disadvantage of the metal hydride, thus optimal design of the metal hydride tank is a crucial issue in relevant studies. Many researchers have established mathematical models to analyze

heat and mass transfer characteristics of metal hydride tanks. Jemni and Nasrallah (1995) formulated a mathematical model for the two-dimensional transient heat and mass transfer within a metal hydride tank. Aldas et al. (2002) studied heat and mass transfer in a metal hydride bed. Bao et al. (2013) developed a model optimize the design parameters of the metal hydride tank. Cho et al. (2013) presented a modeling to simulate and control the dynamic processes of hydrogen discharge from a metal hydride tank in various operating conditions. Minko et al. (2014) presented to analyze heat and mass transfer processes in porous medium. Ma et al. (2014) presented the optimization of heat transfer fins for a finned multi-tubular metal hydride tank and derived the heat transfer equations of tank with various configuration fins (radius, thickness and number). Nakano et al. (2015) developed a metal hydride tank with the aim of recovering the reaction heat of a metal hydride with double coil type heat exchanger.

Dhaou et al. (2011) investigated heat transfer characteristics of a Metal hydride vessel based on spiral heat exchangers with and without fins. Raju and Kumar (2012) presented a systematic study to o optimize the heat exchanger design that influences the storage capacity, gravimetric hydrogen storage density, and refueling time for automotive on-board hydrogen storage systems. Satya et al. (2015) developed a 3D numerical model of heat-and-mass transfer in MH beds for the comparison of hydrogen uptake performance for four cooling layouts: straight pipe (I) and helical coil (II) internal heat exchangers, and external cooling of the MH powder without (III) and with (IV) transversal fins. Also, many studies on the performance analysis of a metal hydride subsystem which serves as a part of an integrated fuel cell system have been demonstrated by researchers. Førde et al. (2009) experimentally investigated hydrogen supply capacity of a metal hydride storage unit which is thermally integrated with a fuel cell. Rizzi et al. (2015) focused on development of the metal hydride tank and to its integration with the fuel cell for improving heat exchanges between the thermal fluid and the tank. Tetuko et al. (2016) presented a mathematical model to study opportunities for simultaneous passive thermal management of an integrated PEM fuel cell and metal hydrogen (MH) storage system by thermal bridging of these two components, using heat pipes. Jiang et al. (2005) studied the dynamic behavior of a thermally coupled hydrogen storage and fuel cell system using experimentally validated models of a metal-hydride hydrogen storage system and a proton exchange membrane (PEM) fuel cell stack.

Although the metal hydride hydrogen storage have been intensively researched, only that developed by Hilali (2015) investigated effect of arrangements of tanks on discharge performance in natural convection. Therefore, the placement of Metal Hydride tanks in the Fuel system have to optimize according to demand of hydrogen. The optimization was based on correlations to find optimum spacing and purpose was either maximum heat transfer or optimum volume. Generally, such the optimization technique is used to remove electric power dissipated in the electronics (Stanescu G, Fowler AJ, Bejan A.,1996).

Thus, this study presents a mathematical model that optimizes arrangements of staggered MH tank banks in forced convection according to different conditions. In the next sections, we give a detailed description of the mathematical model and results.

MATHEMATICAL FORMULATION

Figure 1 shows the arrangement bank of tanks and location in volume LxHxW. L, H and W are the length, height and width of the array, respectively. Tanks were assumed filled with $LaNi_5$ alloy. Reaction kinetics and thermophysical property data for $LaNi_5$ are readily available in literature. In the first step, the governing equations and a new approaching is presented for defining the optimum spacing between tanks according to different operating conditions. Analyses are carried out for various ambient temperatures (290 K, 300 K and 310 K), equilibrium pressures (60 kPa, 100 kPa and 120 kPa) and Reynolds Numbers (6000, 12000 and 30000). Forced convection heat transfer (q) occurs between the tank surfaces (Tw) and the surrounding fluid reservoir (T∞).

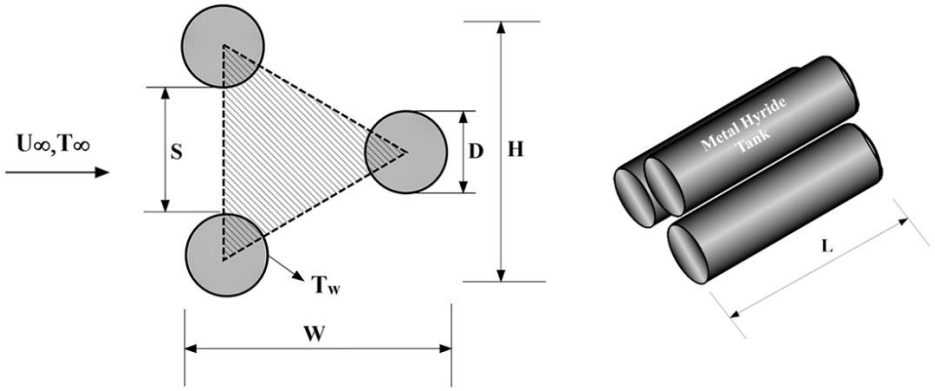

Figure 1. Configuration of the Horizontal Metal Hydride Tanks

In order to simplify the problem, the some assumptions made such as:

Both fluid flow and heat transfer are steady.
The fluid is single phase and incompressible.
Tank surface temperature is uniform.
All the surfaces of the tanks expose to surroundings except bottom and top of tanks.

The governing equations used in this study are described in the following. The equilibrium pressure of desorption is calculated using the van't Hoff relationship. The PCT of various representative AB_5 alloys are shown in Figure 2 (Sandrock 1996).

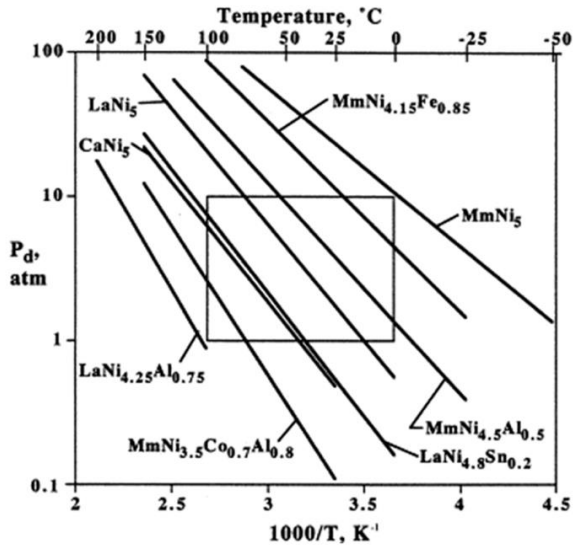

Figure 2. Van't Hoff Plots For Various AB_5 Hydrides

For the $LaNi_5$ hydrogen system, the evolution of the equilibrium pressure is given as a function of temperature.

$$\ln P_{eq} = A - \frac{B}{T} \qquad (1)$$

where A and B for Peqa are determined from the Hydride Material Listing Database as A = 17.608 and B =3704.60, and A and B for Peqd are determined as A = 17.478 and B =3704.60 [4].

The formulation consists of two steps . In the first step, we identify to extremes:

For large spacing, the heat transfer from one tank is

$$q_1 \cong \frac{k}{D} Nu_D \pi DL(T_w - T_\infty) \qquad (2)$$

Where Nusselt number is determined using the correlation due to Zukauskas (Incopera FP., 2007) :

$$Nu_D = 0{,}71 \cdot Re_D^{0{,}6} \cdot Pr^{0{,}36} \qquad Re_D \geq 10^3 \qquad (3)$$

Where Pr is the Prandtl number of the air stream, and The Reynolds number, Re_D, is determined as follows:

$$Re_D = \frac{U_{max}.D}{\nu} \;,\; U_{max} = \frac{(S+D)}{S}.U_\infty$$

Where is the maximum velocity for the staggered configuration and υ is the kinematic viscosity which is obtained depends on the film temperature ($T_f = (T_w - T_\infty)/2$).

The total number of tanks in the bank of cross- sectional area H x W is

$$n = \frac{H\,W}{(S+D)^2 \cos 30} \qquad (4)$$

According to Eq. (4), the total heat transfer from the bank of cross- sectional area H x W is

$$q_{large} = q_1 * n \quad (5)$$

$$q_{large} \cong 2{,}58 \frac{HLW}{(S+D)^2} k(T_w - T_\infty) \left\{ Re_D^{0,6} \cdot Pr^{0,36} \right\} \quad (6)$$

For small spacing, we are assuming tanks almost touch. The heat transfer from the array to air is, therefore, equal to the enthalpy gained by the air, which can be expressed by Eq. (7):

$$q_{small} = \dot{m}\, c_p (T_w - T_\infty) \quad (7)$$

where $\dot{m}$ is the mass flow rate through the L x W plane. The total heat transfer through the plane can be written now as:

$$q_{small} \cong \frac{1}{25} \rho . C_p . \nu . \frac{W.L}{H} . \mathrm{Re}_D^2 . \left(S/D \right)^3 . (T_w - T_\infty) \quad (8)$$

In the second step, we determine optimum spacing S_{opt} for maximum heat transfer by setting as follows. Eq. (6) is equated to Eq. (8) to get the optimum spacing:

$$q_{large} = q_{small}$$

As shown Figure 3, the idea of intersection of asymptotes was utilized to show the existence of an optimum spacing for maximum rate of heat transfer. This technique was used by Bejan et al. 1984 and by Sadeghipour and Pedram Razi, 2001.

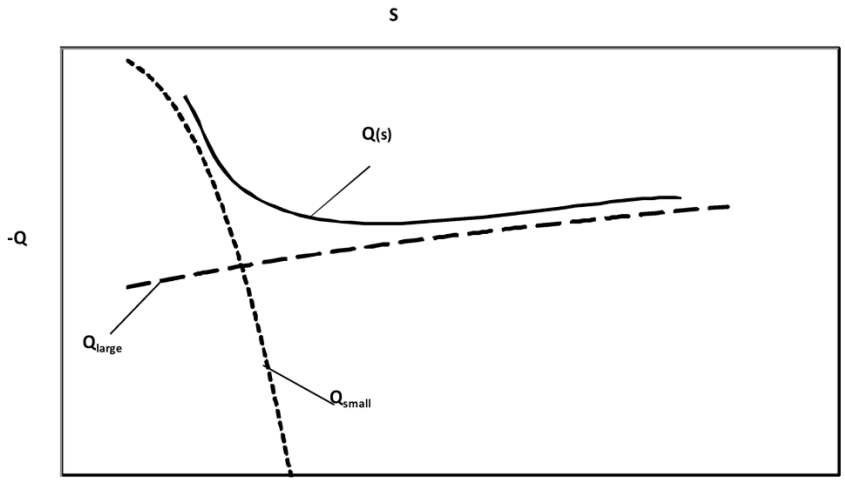

Figure 3. The Optimum Spacing As the Intersection of the Q_{large} and Q_{small} Asymptotes

The following optimum spacing formula is obtained:

$$\left(\frac{S_{opt}}{D} \right) \cong 4. \left(\frac{H}{H-D} \right)^{2/3} . \mathrm{Re}_D^{-1/2} . \mathrm{Pr}^{-1/5} \quad (9)$$

Maximum heat transfer rate can be obtained by substituting equation S_opt into equation (6) or equation (8).

RESULT AND DISCUSSION

In the present study, as shown in Figure 1, the diameter and length of tank for optimization procedure are 85 mm and 400 mm, respectively. The results obtained for MH tanks were presented at different equilibrium pressures varying from 60 to 120 kPa and different ambient temperatures varying from 290 to 310 K. Table 1 shows that maximum heat transfer and optimum spacing changes between ~0.09 and ~0.016 for different equilibrium pressure according to various ambient temperatures (290 K, 300 K and 310 K). As a result, by increasing Reynolds number, the optimal spacing will considerably decrease. It is noticed that, at Reynolds number of $3.0x10^4$ optimum spacing is the lowest. Furthermore, the optimal spacing is the same by decreasing the equilibrium pressure and increasing ambient temperature. Therefore, those variables cannot reduce the optimum spacing, significantly. Moreover, As the spacing (S) is bigger or less than optimum spacing, heat transfer decreases, therefore the optimum spacing improves the overall heat transfer between tanks and air stream.

Table 1. Maximum Heat Transfer and Optimum Spacing According to Reynolds Number and Equilibrium Pressure for Different Ambient Temperatures

(T_{amb}=290 K)							
P_{eq} (kPa)	T_w (K)	Re=6000		Re=12000		Re=30000	
		S_{opt} (m)	Q (W)	S_{opt} (m)	Q (W)	S_{opt} (m)	Q (W)
120	289.0	0.016	-60	0.012	-105	0.09	-209
100	284.9	0.016	-363	0.012	-631	0.09	-1255
60	274.1	0.016	-970	0.012	-1688	0.09	-3355
(T_{amb}=300 K)							
P_{eq} (kPa)	T_w (K)	Re=6000		Re=12000		Re=30000	
		S_{opt} (m)	Q (W)	S_{opt} (m)	Q (W)	S_{opt} (m)	Q (W)
120	289.0	0.016	-668	0.012	-1150	0.09	-2395
100	284.9	0.016	-970	0.012	-1680	0.09	-3441
60	274.1	0.016	-1615	0.012	-2786	0.09	-5542
(T_{amb}=310 K)							
P_{eq} (kPa)	T_w (K)	Re=6000		Re=12000		Re=30000	
		S_{opt} (m)	Q (W)	S_{opt} (m)	Q (W)	S_{opt} (m)	Q (W)
120	289.0	0.016	-1262	0.012	-2197	0.09	-4362
100	284.9	0.016	-1564	0.012	-2720	0.09	-5408
60	274.1	0.016	-2170	0.012	-3779	0.09	-7508

The results according to Reynolds number and ambient temperature are shown Figure 5 for Peq = 60, 100 and 120 kPa, respectively. It can be seen from these plots that the maximum heat transfer rate occurs at S=0.09, 0.012 and 0.016 mm. The fact

that the increase in T_{amb} effects the heat transfer rate an increase. It appears that the heat transfer rate increases monotonically with Reynolds number for all values. Figures show the existence of a local optimal spacing. As an example according to Figure 5 at Reynolds number of $3.0x10^4$, maximum heat transfer gain, in comparison with the arbitrary arrangement, was observed for optimal arrangement with S=0.09. From numerical results obtained in this study, it is important to stress that a heat transfer gain of up to 13 % was observed in the optimum arrangement with S=0.09, 0.012 and 0.016 m.

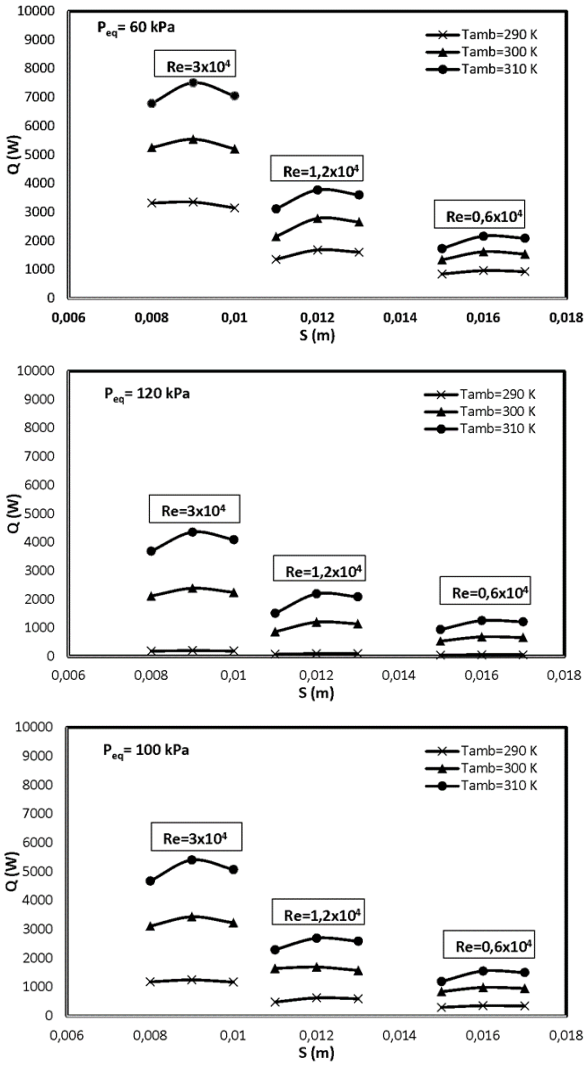

Figure 5. Variation of the Heat Transfer According to Re Number and Ambient Temperature for Peq

CONCLUSIONS

Metal hydride hydrogen storage systems are generally characterized by reaction kinetics of hydrogen absorption and desorption. Most important parameter of metal hydride is reaction enthalpy. This is strongly related to thermal management. Therefore, thermal management of these systems during reactions is a challenge.

This study reports fundamental results for the selection of the spacing between horizontal tanks in an array of defined volume in forced convection conditions. The optimal spacing formulated in equation (9) corresponds to the maximum heat transfer between the entire metal hydride tanks and surrounding fluid.

This study also presents that there exists a distance between the MH tanks for which the Heat transfer is maximum. Results show that the usage of optimum spacing can be a useful way to enhance the hydrogen flow rates of both absorption and desorption. By increasing the Reynolds number, the optimal spacing was reduced more than half. Moreover, the equilibrium pressure and ambient temperature were not affected with optimum spacing. The present results indicate the need of optimization and motivate the development of a general numerical model such that optimal arrangements of MH tanks could be searched according to different parameters simultaneously for maximum heat transfer. Such globally optimized configurations are expected to be of great importance for MH banks design and for the generation of optimal flow structures in general.

This simple model also offers the advantage of ease in manufacturing. However, a good heat exchanger design is not sufficient to enhance the hydrogen flow rates of both absorption and desorption. The model could be very effective for designing of metal hydride tank banks with higher Hydrogen capacity and faster kinetics. The optimization approach accounts for the other geometrical configuration. It is simple enough to apply to integrated hydride tank – fuel cell systems in order to develop control systems and strategies..

REFERENCES

Aldas K, Mat MD, Kaplan Y (2002) A three-dimensional mathematical model for absorption in a metal hydride bed. International Journal of Hydrogen Energy 27 (10):1049-1056. doi:http://dx.doi.org/10.1016/S0360-3199(02)00010-1.

Bao Z, Yang F, Wu Z, Nyallang Nyamsi S, Zhang Z (2013) Optimal design of metal hydride reactors based on CFD–Taguchi combined method. Energy Conversion and Management 65:322-330. doi:http://dx.doi.org/10.1016/j.enconman.2012.07.027.

Bejan A (1984) Convection Heat transfer. Wiley, New York.

Cho J-H, Yu S-S, Kim M-Y, Kang S-G, Lee Y-D, Ahn K-Y, Ji H-J (2013) Dynamic modeling and simulation of hydrogen supply capacity from a metal hydride tank.

International Journal of Hydrogen Energy 38 (21):8813-8828. doi:http://dx.doi.org/10.1016/j.ijhydene.2013.02.142

Dhaou H, Ben Khedher N, Mellouli S, Souahlia A, Askri F, Jemni A, Ben Nasrallah S (2011) Improvement of thermal performance of spiral heat exchanger on hydrogen storage by adding copper fins. International Journal of Thermal Sciences 50 (12):2536-2542. doi:http://dx.doi.org/10.1016/j.ijthermalsci.2011.05.016

Førde T, Eriksen J, Pettersen AG, Vie PJS, Ulleberg Ø (2009) Thermal integration of a metal hydride storage unit and a PEM fuel cell stack. International Journal of Hydrogen Energy 34 (16):6730-6739. doi:http://dx.doi.org/10.1016/j.ijhydene.2009.05.146

Hilali I (2015) Optimum Spacing Between Horizontal Metal Hydride (MH) Hydrogen Storage Tanks Integrated with Fuel Cell Power System in Natural Convection. Journal of Thermal Scienceand Technology 35 (2):129-136

Incropera FP (2007) Fundamentals of Heat and Mass Transfer. John Wiley & Sons, New York

Jemni A, Nasrallah SB (1995) Study of two-dimensional heat and mass transfer during absorption in a metal-hydrogen reactor. International Journal of Hydrogen Energy 20 (1):43-52. doi:http://dx.doi.org/10.1016/0360-3199(93)E0007-8.

Jiang Z, Dougal RA, Liu S, Gadre SA, Ebner AD, Ritter JA (2005) Simulation of a thermally coupled metal-hydride hydrogen storage and fuel cell system. Journal of Power Sources 142 (1-2):92-102. doi:10.1016/j.jpowsour.2004.09.029.

Ma J, Wang Y, Shi S, Yang F, Bao Z, Zhang Z (2014) Optimization of heat transfer device and analysis of heat & mass transfer on the finned multi-tubular metal hydride tank. International Journal of Hydrogen Energy 39 (25):13583-13595. doi:http://dx.doi.org/10.1016/j.ijhydene.2014.03.016.

MacDonald BD, Rowe AM (2006) Impacts of external heat transfer enhancements on metal hydride storage tanks. International Journal of Hydrogen Energy 31 (12):1721-1731. doi:http://dx.doi.org/10.1016/j.ijhydene.2006.01.007.

Minko KB, Artemov VI, Yan'kov GG (2014) Numerical simulation of sorption/desorption processes in metal-hydride systems for hydrogen storage and purification. Part I: Development of a mathematical model. International Journal of Heat and Mass Transfer 68:683-692. doi:http://dx.doi.org/10.1016/j.ijheatmasstransfer.2013.09.056.

Nakano A, Ito H, Bhogilla SS, Motyka T, Corgnale C, Greenway S, Hauback BC (2015) Research and development for a metal hydride tank with double coil type heat

exchanger below 1.0 MPa (G) operation. International Journal of Hydrogen Energy 40 (6):2663-2672. doi:http://dx.doi.org/10.1016/j.ijhydene.2014.12.051.

Raju M, Kumar S (2012) Optimization of heat exchanger designs in metal hydride based hydrogen storage systems. International Journal of Hydrogen Energy 37 (3):2767-2778. doi:http://dx.doi.org/10.1016/j.ijhydene.2011.06.120.

Rizzi P, Pinatel E, Luetto C, Florian P, Graizzaro A, Gagliano S, Baricco M (2015) Integration of a PEM fuel cell with a metal hydride tank for stationary applications. Journal of Alloys and Compounds 645, Supplement 1:S338-S342. doi:http://dx.doi.org/10.1016/j.jallcom.2014.12.145.

Sadeghipour MS, Razi YP (2001) Natural convection from a confined horizontal cylinder: the optimum distance between the confining walls. International Journal of Heat and Mass
Transfer 44 (2):367-374. doi:http://dx.doi.org/10.1016/S0017-9310(00)00110-1.

Sandrock G (1999) A panoramic overview of hydrogen storage alloys from a gas reaction point of view. Journal of Alloys and Compounds 293–295:877-888. doi:http://dx.doi.org/10.1016/S0925-8388(99)00384-9.

Satya Sekhar B, Lototskyy M, Kolesnikov A, Moropeng ML, Tarasov BP, Pollet BG (2015) Performance analysis of cylindrical metal hydride beds with various heat exchange options. Journal of Alloys and Compounds 645, Supplement 1:S89-S95. doi:http://dx.doi.org/10.1016/j.jallcom.2014.12.272.

Stanescu G, Fowler AJ, Bejan A (1996) The optimal spacing of cylinders in free-stream cross-flow forced convection. International Journal of Heat and Mass Transfer 39 (2):311-317. doi:http://dx.doi.org/10.1016/0017-9310(95)00122-P.

Tetuko AP, Shabani B, Andrews J (2016) Thermal coupling of PEM fuel cell and metal hydride hydrogen storage using heat pipes. International Journal of Hydrogen Energy 41 (7):4264-4277. doi:http://dx.doi.org/10.1016/j.ijhydene.2015.12.194.

NUMERICAL STUDY OF FLOW STRUCTURES WITHIN DIFFERENT CAVITIES USING LARGE EDDY SIMULATION

Rahim Hassanzadeh[1*], Nehir Tokgoz[2], Besir Sahin[3]

[1]Department of Mechanical Engineering, Urmia University of Technology, Urmia, Iran
2Department of Energy Systems Engineering, Osmaniye Korkut Ata University, Osmaniye, Turkey
[3]Faculty of Engineering and Architecture, Mechanical Engineering Department, Cukurova University, Adana, Turkey

r.hassanzadeh@uut.ac.ir, nehirtokgoz@osmaniye.edu.tr, bsahin@cu.edu.tr

ABSTRACT: Large eddy simulation using a classic Smagorinsky sub-grid scale is applied for predicting the vortical flow structures within cavities. Here, flow within three different cavities such as rectangular, semi-circular, and triangular shapes are studied in order to examine the shape effects on the flow behavior. The ratio of cavity length per cavity depth is L/D=2.0 for all cavity shapes. On the other hand, simulations are carried out at three different Reynolds numbers such as 10^3, 10^4, and 10^5 in order to understand the effects of Reynolds number on the wake structures within cavities. It is found that flow structures change as a function of Reynolds number and geometry of cavities. In addition, numerical predictions revealed that the rectangular cavity imposes a higher drag to fluid flow at Re=10^3 and 10^4 in comparison to semi-circular and triangular cavities. A pressure jump or kinetic energy reduction is realized for semi-circular cavity at Re=10^5. The present numerical results are in good agreement with previous data available in the literature.

Keywords: Cavity, Finite Volume Method, Large Eddy Simulation, Turbulence
*Corresponding author. Tel: +98-4433980233, E-mail: r.hassanzadeh@uut.ac.ir

INTRODUCTION

Flow within cavities is seen in a wide variety of engineering applications such as nuclear and combustion, energy and hydraulic systems, aerospace applications and many other industrial applications. On the other hand, cavities are the fundamental structures and are ideal for understanding of three-dimensional flows. In the past decade, several investigations were performed on the flow within cavities. In general, previous investigations were carried out, more, on two different categories such as lid-driven cavities [1-13] and thermally driven cavities [14-17], generally. In other words, the investigation of flow structures within different cavities without lid or thermal drives have a limited data in the open literature. For example, Ozalp et al.

[18] studied the flow behavior past cavities with rectangular, semi-circular, and triangular shapes, experimentally using particle image velocimetry for the cavity length to the cavity depth ratio of L/D=2. They stated that rectangular and triangular cavities have larger amplitudes of velocity fluctuations while semi-circular cavity has the smallest amplitudes in velocity fluctuations.

Some of previous conducted numerical research studies focused on the numerical approaches using different turbulence methods. For example, Saqr et al. [19] applied a modified k-ε turbulence method for prediction of shear-driven vortex flow in a cylindrical cavity. They stated that the results of the computations demonstrated good agreements with an experimental result. Saqr et al. [20] also conducted numerical work using Large Eddy simulation (LES) with similar flow geometry and they revealed that the flow in the vortex core was laminar, although in other regions (such as the separation region) it was fully turbulent flow. Ryu and Baik [21] used RNG k-ε for study on the flow and dispersion in an urban cubic cavity. It was stated that a primary and secondary vortices including end-wall vortices appear in the cavity. On the other hand, Zhang et al. [22] applied Lattice Boltzmann method for simulation of lid-driven flow in trapezoidal cavities for Reynolds number in the range of $100 \leq Re \leq 15{,}000$. Peng and Davidson [23] applied LES method for the simulation of turbulent buoyant flow in a confined cavity. Arumuga Perumal and Dass [24] implemented the Lattice Boltzmann method for flow simulation in the two-dimensional cavity. Chen et al. [25] used a LES-based Lattice Boltzmann model to the study of turbulent double-diffusive natural convection in a square cavity. Lawson and Barakos [26] presented a review on the numerical simulations for high-speed turbulent cavity flows. Salinas-Vazquez et al. [27] applied LES for a confined square cavity flow with natural convection based on compressible flow equations. Effects of wall model and mesh study on the partial cavities were performed by Goncalves and Decaix [28].

Examination of the previous works on the cavity flow indicates that the flow field within the cavities as a function of the cavity shape and the Reynolds number was not studied in details. In addition, the study of the flow field of cavity with infinite length in spanwise direction is unique in this investigation since the previous works are almost dealt with the lid-driven cavities with finite dimensions. On the other hand, application of LES in such flows is very limited since many different recent works [29-31] were performed using LES with different subgrid scale models. For this reason, this work aims to present the vortical flow structure within three different cavity shapes such as rectangular, semi-circular, and triangular cavities at various Reynolds numbers in the range of $10^3 \leq Re \leq 10^5$ using LES. It should be mentioned that examination of LES abilities in this study is a minor purpose, but the main goal of this work is to compute and present flow structures within the cavities as a function of the cavity shape and the Reynolds number. However, implementation of LES requires some additional considerations such as higher grid resolutions and CPU power. Our results show good agreements with previous numerical predictions and experimental results.

COMPUTATION DETAILS

Flow domain and boundary conditions

In the present study, a 3-D Newtonian fluid flow within three different cavities such as rectangular, semi-circular, and triangular shapes are simulated at three various Reynolds numbers such as 10^3, 10^4, and 10^5 with respect to cavity depth, D, and free-stream velocity, U_∞. The ratio of cavity length, L, per cavity depth, D, is identical for all shapes and is equal to 2.0. The flow domain with dimensions of the 20D in the streamwise direction ($0 \le x \le 20D$), 5D in vertical direction ($-D \le y \le 4D$), and 4D in spanwise direction ($-2D \le z \le -2D$) is defined for all cavity cases as illustrated in Figure 1. For inlet section, lower surface, and cavity walls the Dirichlet boundary conditions are applied while at the upper surface and outlet section of flow domain the Neumann boundary conditions are used. A uniform velocity is defined for incoming flow. It should be mentioned that in order to consider the infinite cavity length in spanwise direction, the Neumann boundary conditions are implemented for side walls. A multi-block grid system is constructed for each flow domain as indicated in Figure 2. For this reason, each flow domain divided into different blocks and after that, the non-uniform grids are defined for each block in which grids with higher resolutions are applied within cavities. The numbers of control volumes are 831,000, 716,000, and 818,000 for flow domains corresponding to rectangular, semi-circular, and triangular cavity cases, respectively in which the minimum grid size is 0.02D for all cases. The grids are stretched near the wall in both streamwise and vertical directions using 8-10 nodes clustered within $y^+ \le 10$. However, a uniform grid distribution is used in the streamwise direction. In fact, the constructed grid sizes provide a good compromise between accuracy and CPU time.

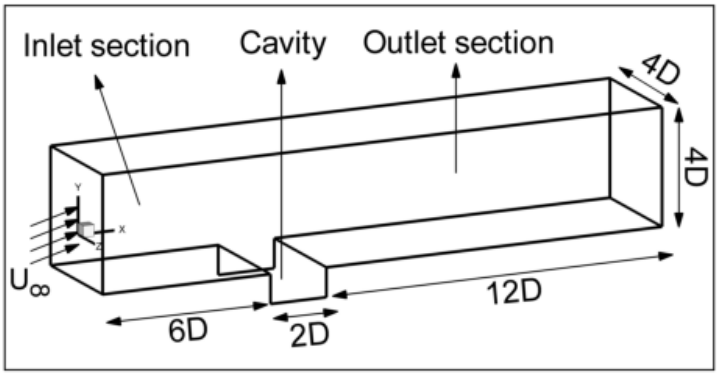

Figure 2. Schematic view of cavity, flow domain, and coordinates

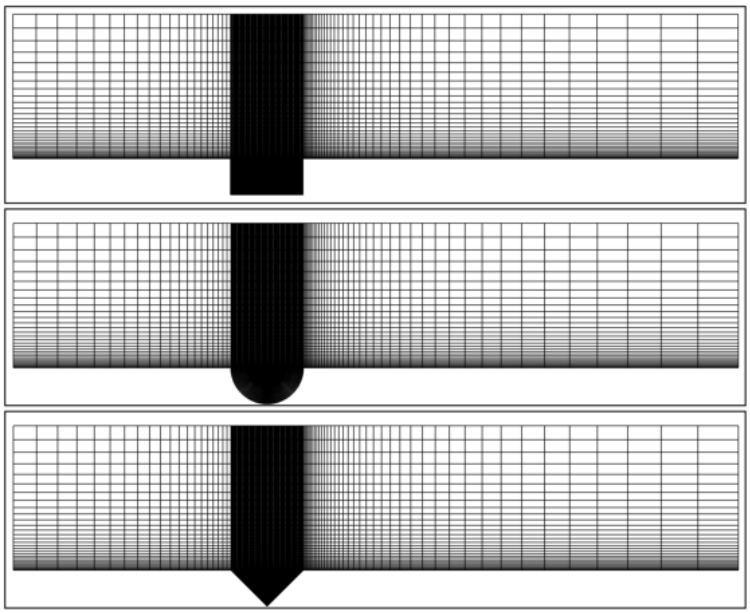

Figure 3. Multi-block non-uniform grid system

Governing equations and numerical procedure

The three-dimensional, Newtonian, and incompressible fluid flow can be modeled by

Continuity and momentum equations;

$$\frac{\partial u_i}{\partial x_i} = 0 \tag{1}$$

$$\rho \frac{\partial u_i}{\partial t} + \rho \frac{\partial}{\partial x_j}(u_j u_i) = -\frac{\partial p}{\partial x_i} + \mu \frac{\partial^2 u_i}{\partial x_j \partial x_i} \tag{2}$$

where u, ρ, p and τ are velocity, density, pressure and shear stress tensor, respectively. Here, for the simulation of vortical flow characteristics, LES is implemented and combined with Navier-Stokes equations. In LES, despite of RANS models, the small scale eddies are separated from the large scale eddies. After separation, while large scale eddies are resolved explicitly the small scale eddies are modeled like as RANS method by application of sub-grid scale (sgs) model. Separation between small scale eddies and large scale eddies become possible by introducing of a filter function. The filtering procedure is summarized as follows

$$\bar{f}(x) = \int_{-\infty}^{+\infty} f(x') G(x, x') dx', \; f'(x) = f(x) - \bar{f}(x) \tag{3}$$

In equation (3), $\bar{f}(x)$, $f(x')$, and $f'(x)$ are filtered component, unfiltered function, and sgs fluctuating part, respectively. Here, G(x, x') is the filter function and has the following property

$$\int_{-\infty}^{\infty} G(x, x') = 1 \tag{4}$$

Since there are different filtering functions for separating of eddies, in this study one of the simplest functions, which is box filter, is used. In this filtering scheme, the filter function, G(x, x'), is defined by means of local control volume size as follow:

$$G(x,x') = \begin{cases} 1/\Delta & if\ |x-x'| \le \overline{\Delta}/2 \\ 0 & otherwise \end{cases} \quad (5)$$

Here, Δ is the filter width, which is related to the local grid size by following equation:

$$\Delta = (\Delta V_{IJK})^{1/3} \quad (6)$$

where ΔV_{IJK} is the local control volume size. After application of the filtering process, the governing equations (1) and (2) can be written as;

$$\frac{\partial \bar{u}_i}{\partial x_i} = 0 \quad (7)$$

$$\frac{\partial \bar{u}_i}{\partial t} + \frac{\partial}{\partial x_j}\left(\bar{u}_i \bar{u}_j\right) = -\frac{1}{\rho}\frac{\partial \bar{p}}{\partial x_i} + \nu \frac{\partial^2 \bar{u}_i}{\partial x_j \partial x_j} - \frac{\partial \bar{\tau}_{ij}}{\partial x_j} \quad (8)$$

where the over-bared quantities are the filtered variables and τ_{ij} is the sgs stress tensor defined as;

$$\tau_{ij} = \overline{u_i u_j} - \bar{u}_i \bar{u}_j \quad (9)$$

There are some different sgs models, for instance, one of the old, simple, and more applicable ones is the model of Smagorinsky [32] that is used in the present study. The Smagorinsky sgs model was initially proposed in 1963 by Joseph Smagorinsky (1963) and used in the first time in the LES simulation by Deardorff [33]. Equations for this model, which are defined by means of eddy viscosity concept, are as follow;

$$\tau_{ij} - \frac{1}{3}\delta_{ij}\tau_{kk} = -2\upsilon_{sgs}\bar{s}_{ij} \quad (10)$$

$$\upsilon_{sgs} = (C_s\Delta)^2\sqrt{2\bar{s}_{ij}\bar{s}_{ij}} \equiv (C_s\Delta)^2|\bar{s}| \quad (11)$$

$$\bar{s}_{ij} = \frac{1}{2}\left(\frac{\partial \bar{u}_i}{\partial x_j} + \frac{\partial \bar{u}_j}{\partial x_i}\right) \quad (12)$$

Here, C_S is the model constant, which in the classic Smagorinsky sgs model is constant and it does not change with time and space.

In the present study, in order to discrete the convection terms in equation (8), the QUICK scheme is applied. On the other hand, for pressure-velocity coupling, the SIMPLE algorithm [34] is applied. The dimensionless physical time steps are set to $\Delta t=0.008\ D/U_\infty$, $\Delta t=0.06\ D/U_\infty$, and $\Delta t=0.08\ D/U_\infty$ at $Re=10^3$, 10^4, and 10^5, respectively. It was found that decreasing of physical time step in each simulation did not alter results. Moreover, each time step was consisted of 20 time iterations and computing was performed with 3000, 2600, and 6000 time steps for $Re=10^3$, 10^4, and 10^5, respectively. In addition, the convergence of the numerical 3-D velocity components is established at each time step by controlling the residuals of all equations, which are defined to be solved by setting their variations less than 10^{-8}.

Grid size independence

In order to study the grid size independence of results, different grid sizes are constructed and examined for each cavity shape at each Reynolds number, distinctly. The solution was ensured to be independent from the grid quality and cell size by performing a grid size independent study on different grid sizes and control volume numbers. The details of two last grids, which all of them were hexahedral structures, are given in table 1(a) that entitled by case 1 and case 2. The grid independence study reveals rather slight differences between the case 1 and case 2 for the value of y^+ as indicated in table 1(b)-(d). However, all results of this study are reported with respect to the case 2. Moreover, for validation of results, the obtained results in this study were compared with previous experimental results and numerical predictions.

Table 3. Grid size independence study (a) number of control volumes of case 1 and case 2, (b) maximum y^+ at $Re=10^3$, (c) maximum y^+ at $Re=10^4$, (d) maximum y^+ at $Re=10^5$ between case 1 and case 2

(a)	Rectangular	Semi-circular	Triangular
Case 1	740,000	660,000	736,800
Case 2	831,000	716,000	818,000

(b)	Rectangular	Semi-circular	Triangular
Case 1	2.678	2.679	2.677
Case 2	2.678	2.680	2.679

(c)	Rectangular	Semi-circular	Triangular
Case 1	11.888	11.885	11.873
Case 2	11.888	11.885	11.873

(d)	Rectangular	Semi-circular	Triangular
Case 1	73.197	75.006	73.185
Case 2	73.177	73.559	73.226

RESULTS AND DISCUSSIONS

Time-averaged flow data

In this sub-section, time-averaged flow patterns are presented. Figure 3(i) illustrates patterns of time-averaged streamlines, $\langle\psi\rangle$, within three different cavities such as rectangular, semi-circular, and triangular shapes at $Re=10^3$, 10^4, and 10^5. It is seen clearly that for the rectangular cavity at $Re=10^3$ three different vortices are developed. That is, a well-defined large-scale core vortex, V_1 which rotate clockwise and occupied the whole upper side of the cavity. In addition, a developing vortex, V_2, which rotate counter clockwise and located at the conjunction of upstream wall and lower wall of the cavity, is also evident. Finally, a small-scale corner vortex, V_3, which is located at the conjunction of downstream wall and lower wall of the cavity, is observed. As the Reynolds number increases to a value of 10^4, within the

rectangular cavity, developing and corner vortices, V_2 and V_3, become smaller while the large scale core vortex, V_1, dominates whole space of cavities. Finally, as seen, at $Re=10^5$, developing and corner vortices, V_2 and V_3, are vanished and the large-scale vortex, V_1, occupies whole rectangular space. In the semi-circular cavity, at $Re=10^3$, partially similar wake structures in the rectangular cavity are developed, but the corner vortex did not appear. A noticeable event about the semi-circular cavity is the elimination of developing vortex, V_2, at $Re=10^4$ which reveals that the semi-circular cavity is sensitive to the increment of Reynolds number compared with other shapes in the case of lower Reynolds number. At $Re=10^5$, no significant changes are realized for semi-circular cavity. Responses of the triangular cavity against the Reynolds number are completely gradual and systematic comparing to the rectangular and semi-circular cavities. In other words, at $Re=10^3$, a large-scale core vortex, V_1, and a developing vortex, V_2, appear within the triangular cavity. Once the Reynolds number increases, the size of developing vortex, V_2, gradually decreases as indicated in the right column of Figure 3. The obtained results for vortex mechanism within all three different cavities were compared with experimental data reported by Ozalp et al. [18] as illustrated in Figure 3(ii). It is known that, in experimental works reported by Ozalp et al. [18], close to the Plexiglas surface there is a reflection laser light which deteriorates experimental readings in close region of the cavity walls.

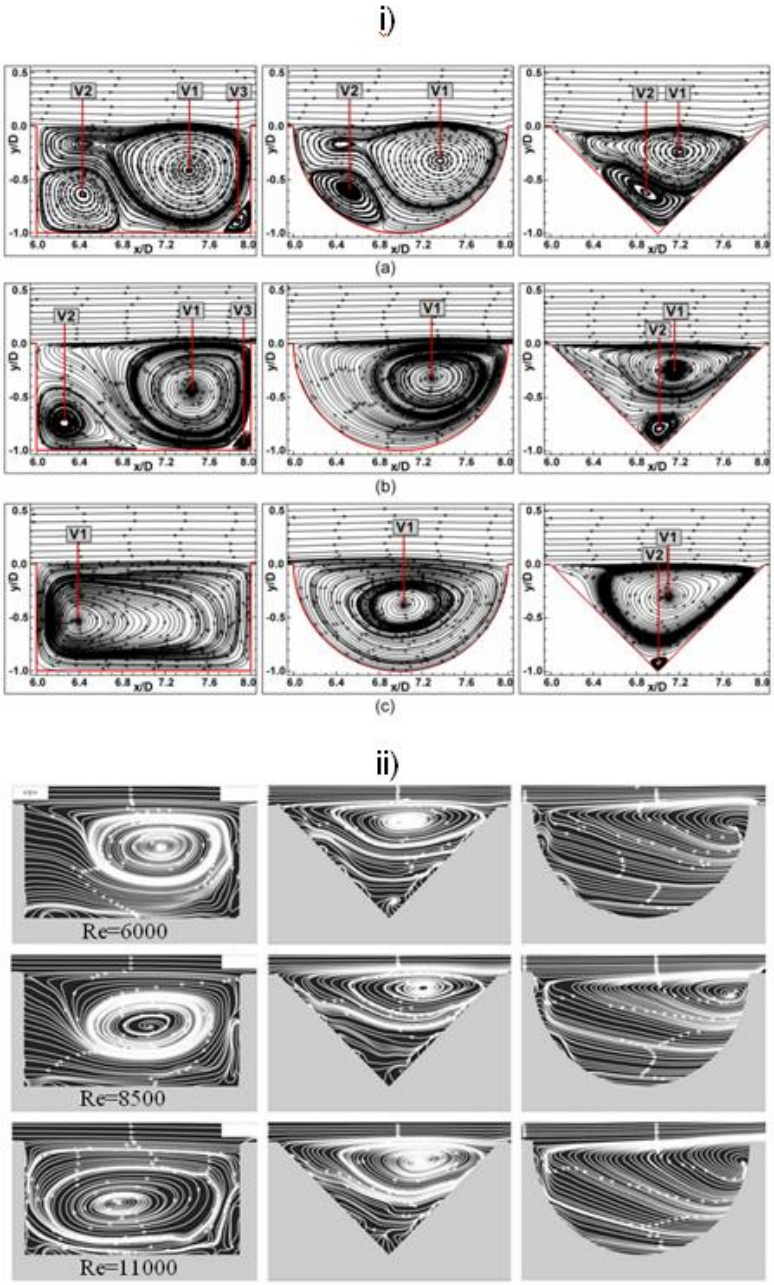

Figure 4. Time-averaged streamlines, <ψ>, patterns within three different cavities such as rectangular, semi-circular, and triangular cavities at (a) Re=10^3, (b) Re=10^4, (c)Re=10^5 (upper figure: present study and lower figure: experimental data reported by Ozalp et al., 2010)

Figure 4 shows the variation of time-averaged streamwise velocity, $<u/U_\infty>$, which is scaled by free-stream velocity, U_∞, along the arbitrary cross sectional line at S/L=0.2 within three different cavities such as rectangular, semi-circular, and triangular shapes at Re=10^3, 10^4, and10^5. Here, "S" is measured from the upstream tip of cavities towards the downstream side and "L" is the cavity length as illustrated in right hand side images of Figure 4. At Re=10^3, flow at S/L=0.2 experiences positive values of the streamwise velocity in the lower side and negative values at upper side for the rectangular and semi-circular cavities. At Re=10^4, the flow behavior does not change significantly for the rectangular cavity, but the velocity gradient decreases for the

semi-circular cavity indicating again that semi-circular cavity is more sensitive to the Reynolds number between 10^3 and 10^4 than the rectangular cavity as stated before in Figure 3. Examination of time-averaged streamwise velocity, $\langle u/U_\infty \rangle$, profile for S/L=0.2 at Re=10^5 reveals that at the upstream portion of the rectangular and semi-circular cavities negative streamwise velocity values dominate at the lower sides of cavities while positive values occur on upper sides of the cavities. This flow behavior states the existing of a clockwise recirculation pattern of flow within the rectangular and semi-circular cavities at higher Reynolds numbers. In addition, at S/L=0.2, Flow structures in the triangular cavity do not alter significantly by increasing the Reynolds number due to the very small streamwise velocity gradients as indicated in the last image of Figure 4.

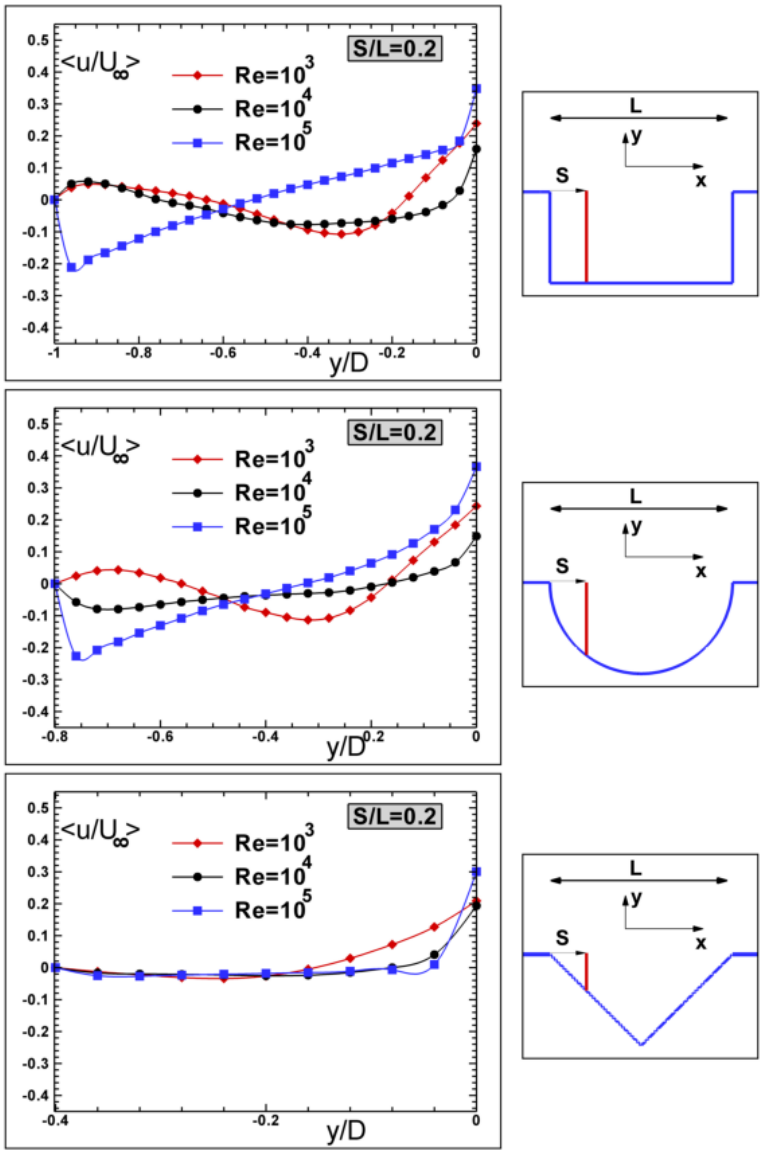

Figure 5. Time-averaged streamwise velocity, $\langle u/U_\infty \rangle$, distributions within the three different cavities such as rectangular, semi-circular, and triangular cavities along S/L=0.2 in which "S" is measured from the tip of cavity towards the downstream side and "L" is the cavity length at (a) Re=10^3, (b) Re=10^4, (c) Re=10^5

Variation of time-averaged streamwise velocity, $\langle u/U_\infty \rangle$, illustrated in Figure 5 along the cross sectional lines at the location of S/L=0.5 within three different cavities. Examination of first image reveals that, at S/L=0.5, within the rectangular and semi-circular cavities the negative streamwise velocity values dominate at the regions close to lower wall of cavities while the positive streamwise velocity values are mostly developed at higher elevations. In addition, once the Reynolds number increases, the velocity gradient increases within cavities. For S/L=0.5, flow in the triangular cavity experiences positive streamwise velocity values at lower elevations in the cases of $Re=10^3$ and 10^4. On the other hand, at $Re=10^5$, the negative streamwise velocity values are developed at the lower elevations in the triangular cavity along S/L=0.5 as demonstrated in the last image of Figure 5.

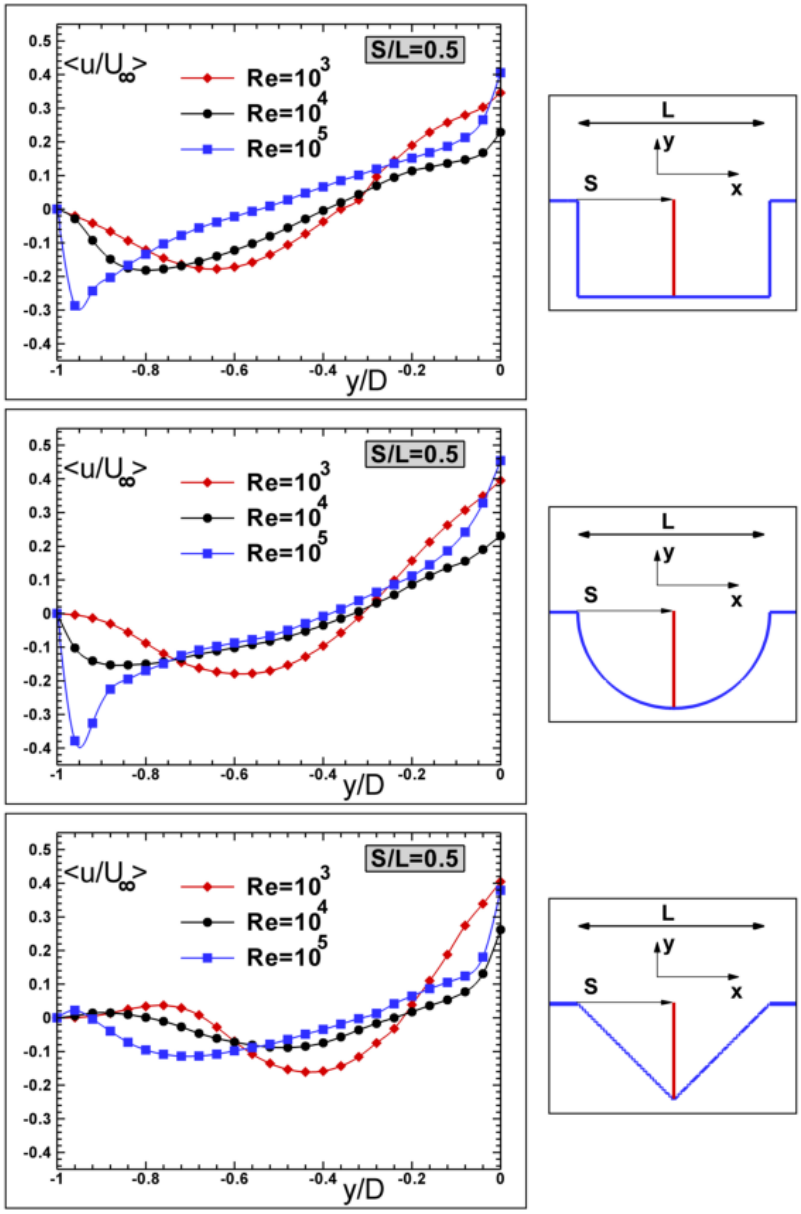

Figure 6. Time-averaged streamwise velocity, $\langle u/U\infty \rangle$, distributions within the three different cavities such as rectangular, semi-circular, and triangular cavities along S/L=0.5 in which "S" is measured from the tip of cavity towards the downstream side and "L" is the cavity length at (a) Re=103, (b) Re=104, (c) Re=105

Figure 6 illustrates the variation of time-averaged streamwise velocity component, $<u/U_\infty>$, along S/L=0.8 within all cases of cavities. Despite of the fact that, at S/L=0.8, the negative streamwise velocity values are dominated at lower elevations of three different cavity shapes for all Reynolds numbers however, flow structure within the triangular cavity did not alter significantly by increasing the Reynolds number as previously stated in Figure 3.

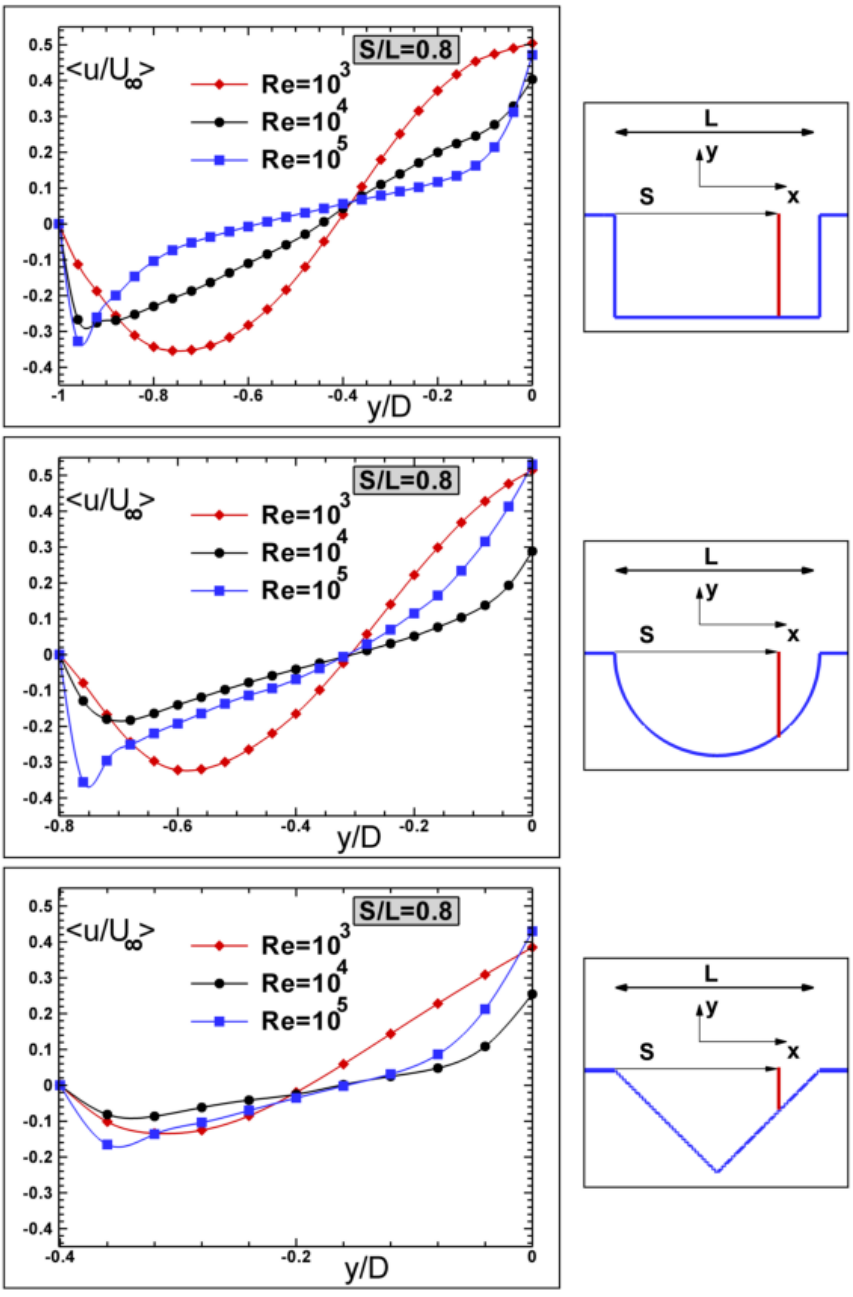

Figure 7. Time-averaged streamwise velocity, $<u/U\infty>$, distributions within the three different cavities such as rectangular, semi-circular, and triangular cavities along S/L=0.8 in which "S" is measured from the tip of cavity towards the downstream side and "L" is the cavity length at (a) Re=103, (b) Re=104, (c) Re=105

Figure 7 shows time-averaged static pressure,$<P_s/0.5\rho U^2_\infty>$, patterns which are scaled by dynamic pressure for all cases of cavities at $Re=10^3$, 10^4, and10^5. Examination of time-averaged static pressure, $<P_s/0.5\rho U^2_\infty>$, at $Re=10^3$ reveals that a

maximum negative pressure pocket is developed near the downstream side of all cavities. The value of time-averaged static pressure, $<P_s/0.5\rho U^2_\infty>$, for the triangular cavity is smaller compared with other cases. An increase of the Reynolds number, causes an extension on the negative pressure pocket within cavities at $Re=10^4$. Finally, the negative static pressure is observed in the entire volume of the cavities. Comparison of images in Figure 7 indicates an unexpected pressure jump in the semi-circular cavity at $Re=10^5$. This flow behavior of the semi-circular cavity states that the rates of momentum transfer and kinetic energy decrease in the higher Reynolds number. A systematic increase in momentum transfer with increasing of the Reynolds number is seen in the rectangular cavity as illustrated in Figure 7. Further examination of Figure 7 states that the triangular cavity imposes a smaller drag on the fluid flow in comparison to the rectangular and semi-circular cavities at all Reynolds numbers.

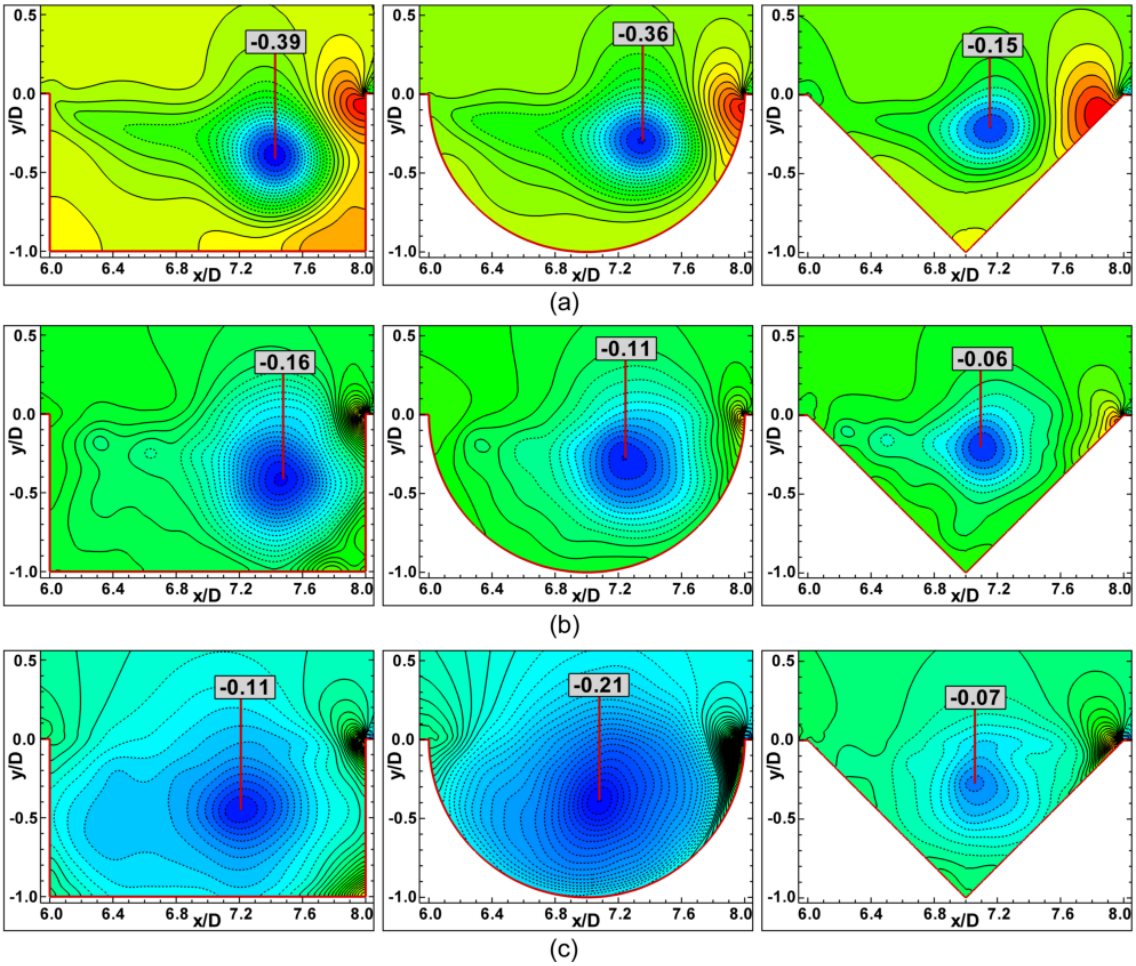

Figure 8. Time-averaged static pressure, $<P_s/0.5\rho U^2_\infty>$, patterns within three different cavities such as rectangular, semi-circular, and triangular cavities at (a) $Re=10^3$(contour increment: 0.0275), (b) $Re=10^4$ (contour increment: 0.01), (c) $Re=10^5$(contour increment: 0.01)

Patterns of root mean square of fluctuating pressure, $<P_{rms}/0.5\rho U^2_\infty>$, for all cavities at $Re=10^3$, 10^4, and10^5 are illustrated in Figure 8, which is made dimensionless by dynamic pressure. For each cavity, at $Re=10^3$, a peak value is detected near the

downstream wall. An interesting result is obtained as the Reynolds number increases. In other words, increasing the Reynolds number decreases the value of $<P_{rms}/0.5\rho U^2_\infty>$, within cavities revealing an increase on the turbulent kinetic energy. The minimum value of $<P_{rms}/0.5\rho U^2_\infty>$, which corresponds to the maximum turbulent kinetic energy are obtained within cavities once the Reynolds number reaches a value of 10^5. The root mean square of fluctuating pressure, $<P_{rms}/0.5\rho U^2_\infty>$, at $Re=10^5$ is higher within the semi-circular cavity case which corresponds to the lower turbulence intensity and turbulent kinetic energy compared with rectangular and triangular cavities.

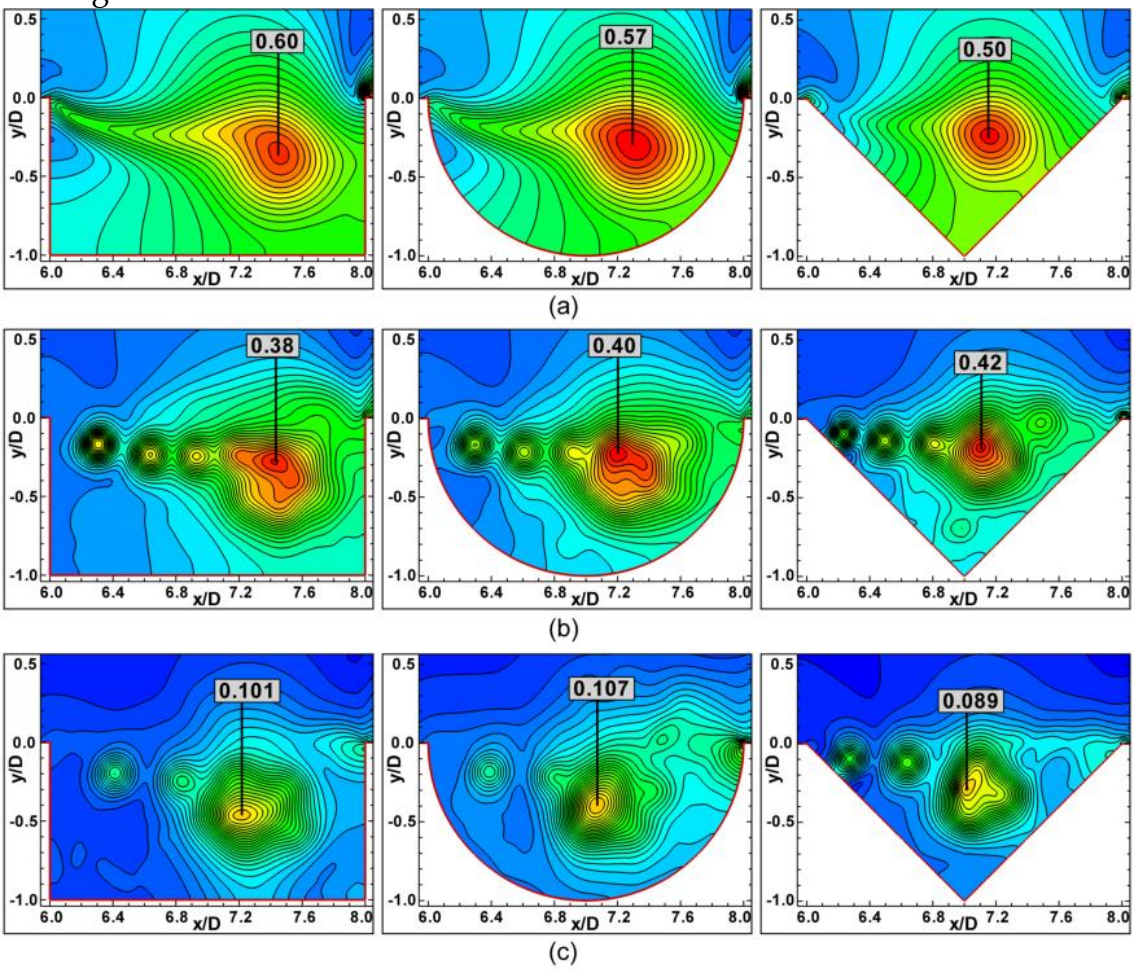

Figure 9. Time-averaged root mean square of fluctuating pressure, $<P_{rms}/0.5\rho U^2_\infty>$,patterns within three different cavities such as rectangular, semi-circular, and triangular cavities at (a) $Re=10^3$(contour increment: 0.025), (b) $Re=10^4$ (contour increment: 0.015), (c) $Re=10^5$(contour increment: 0.015)

Instantaneous flow data

It is known that the instantaneous flow data are useful and necessary for analysis of unsteady flows such as understanding of the physics of flow and statistical studies of turbulence in detail. Figure 9 illustrates patterns of the instantaneous streamlines, ψ, within all cases of cavities at $Re=10^3$, 10^4, and 10^5. Images of Figure 9 give useful information on the wake deformation with respect to the cavity shape and the Reynolds number. At $Re=10^3$, a systematic wake

deformation is recognized for all cases of cavities in this study. The size of the large-scale core vortex, V_1, becomes smaller gradually within the period of time while the developing vortex, V_2, shows a limited expansion within all three cavities. It is due to this fact that flow within cavities at $Re=10^3$, except at the separation points, is laminar. Having Reynolds number as $Re=10^4$, a wake deformation is seen within all cavities. The location of large-scale vortex changes within the cavities indicating occurrence of the higher flow recirculation within cavities while the large-scale and developing vortices, V_1 and V_2, keep their primary shapes more or less same. A noticeable and important results are obtained at $Re=10^5$. That is seen clearly in the last row of Figure 9, at $Re=10^5$, wake deformation becomes stronger in the rectangular and triangular cavities while within the semi-circular cavity, a large scale core vortex, V_1, shows a tendency to keep its primary shape more or less same. On the other hand, the small-scale vortices appear within the rectangular and triangular cavities which indicates the higher rate of turbulence at $Re=10^5$ within the rectangular and triangular cavities. In addition, the lower turbulence intensity in the semi-circular cavity is detected at high Reynolds numbers compared with other cases.

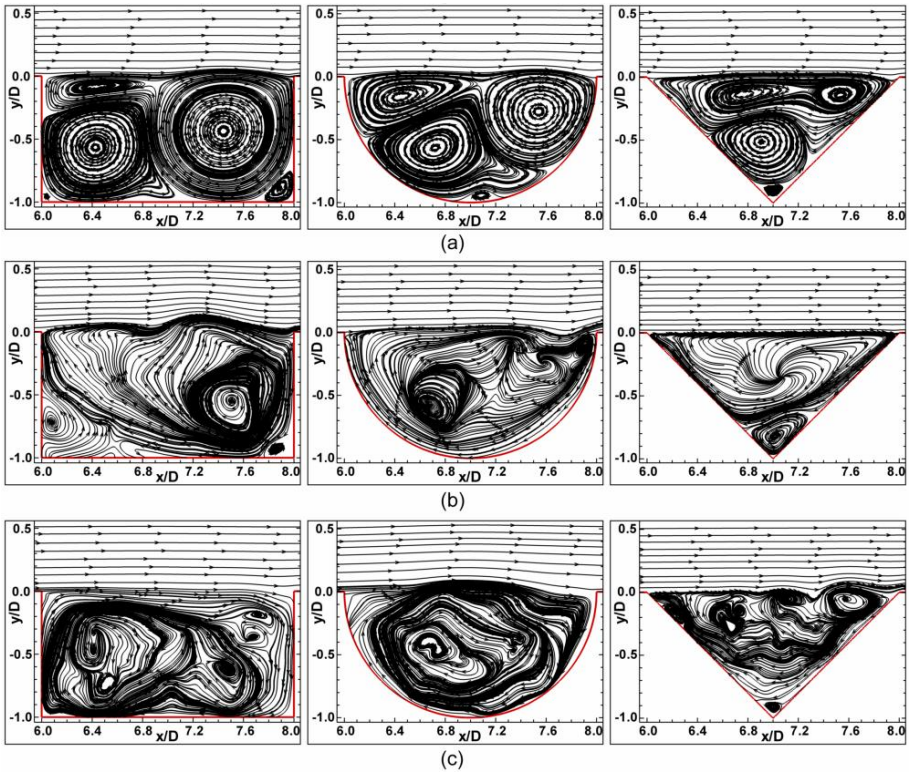

Figure 10. Instantaneous streamlines, ψ, patterns within three different cavities such as rectangular, semi-circular, and triangular cavities at (a) Re=103, (b) Re=104, (c) Re=105

Wakes deformation within different cavities at various Reynolds numbers are understood well by examination of vortical structures. Figure 10 demonstrates patterns of normalized vortical structure, $\omega_z D/U_\infty$, within the rectangular, semi-circular, and triangular cavities at $Re=10^3$, 10^4, and 10^5. It is seen clearly that at $Re=10^3$, the large-scale vortical structures are detected in all cases of cavities. By appearance of small scale eddies, at $Re=10^4$, flow entrainment increases and hence

kinetic energy of flow within the cavities increases as seen in Figure 10. Increasing the kinetic energy within the cavity develops a flow recirculation region near the cavity wall for all cases of cavities. This flow recirculation is more evident in the rectangular cavity than two other cases indicating the higher turbulence intensity. By increasing the Reynolds number up to Re=10^5, the appearance of small scale eddies becomes highly detectable. Furthermore, the turbulence intensity and the rate of flow entrainment within cavities increase. Finally, small scale eddies within cavities at higher Reynolds numbers increases the interaction between eddies. As a result, it is expected to increase the eddy viscosity as the Reynolds number increases.

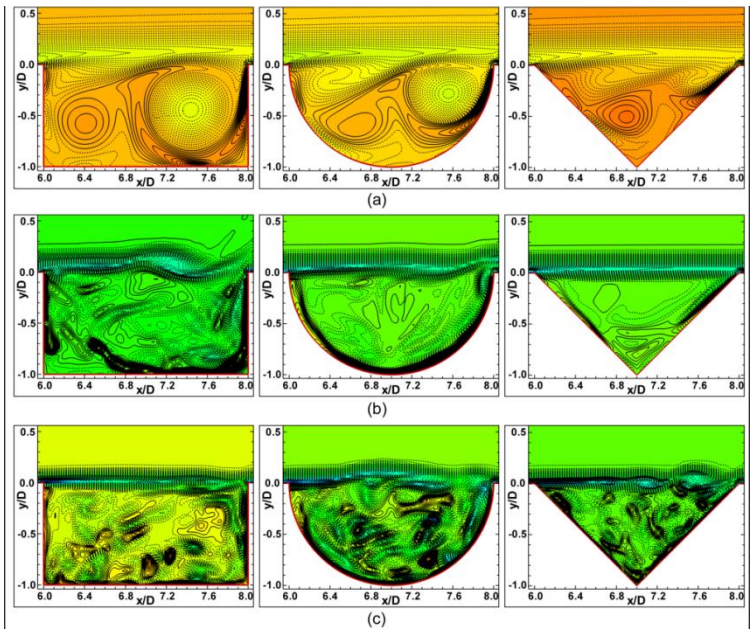

Figure 11. Instantaneous vortical structure, ωzD/U∞, patterns within three different cavities such as rectangular, semi-circular, and triangular cavities at (a) Re=103, (b) Re=104, (c) Re=105

Since the turbulent flow has a three-dimensional nature, one need to interpret the vortical flow structure in vertical direction, namely in the y-z plane. Figure 11 illustrates the numerical prediction of normalized instantaneous vortical structure $\omega_y D/U_\infty$ in y-z plane located at the centre of all cases of cavities. First and second rows of Figure 11 shows the patterns of $\omega_y D/U_\infty$ at Re=$10^4$and 10^5, respectively. Like as the previous figures, dashed lines indicate the negative values of vortical structures. The flow seems to have a coherent turbulent structure at Re=10^4 within the cavities. Increasing the Reynolds number up to 10^5 causes the large vortical structures to be broken into smaller structures as seen in the second row of Figure 11. As a result, flow entrainment and the rate of eddy viscosity will increase within the cavities at higher Reynolds numbers.

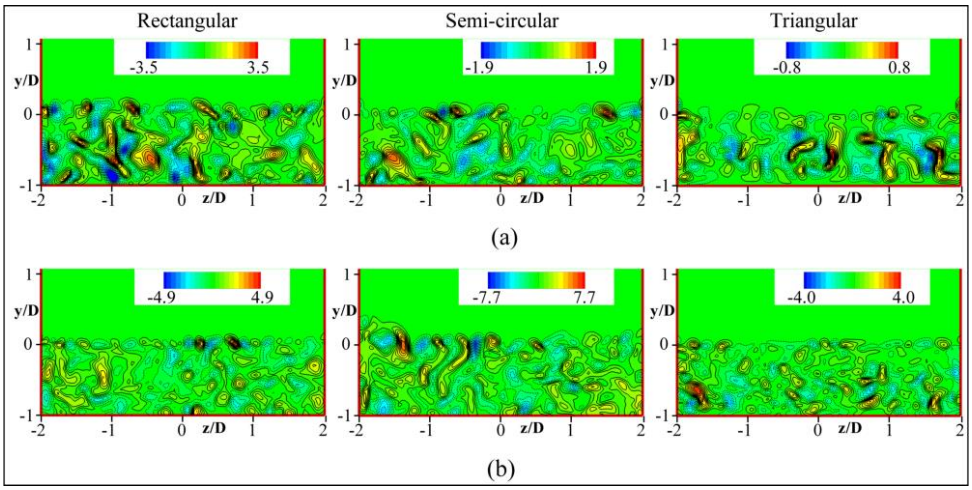

Figure 12. Instantaneous vortical structure, ωyD/U∞, patterns within three different cavities such as rectangular, semi-circular, and triangular cavities at (a) Re=104, (b) Re=105

Figure 12 demonstrates the iso-surface of vortical flow structures in all cases of cavities at $Re=10^3$, 10^4, and 10^5. In general, for all cavities the flow structure is unchanged in spanwise direction and flow can be assumed to be laminar within cavities at $R=10^3$. On the other hand, chaotic structures within cavities are developed and flow become three-dimensional when the Reynolds number increases to a value of $Re=10^4$. Increasing the Reynolds number to a value of 10^5, causes the larger scale eddies break into the smaller eddies resulting in the higher turbulence intensity, the higher eddy viscosity, and the higher flow entrainment within all cavities.

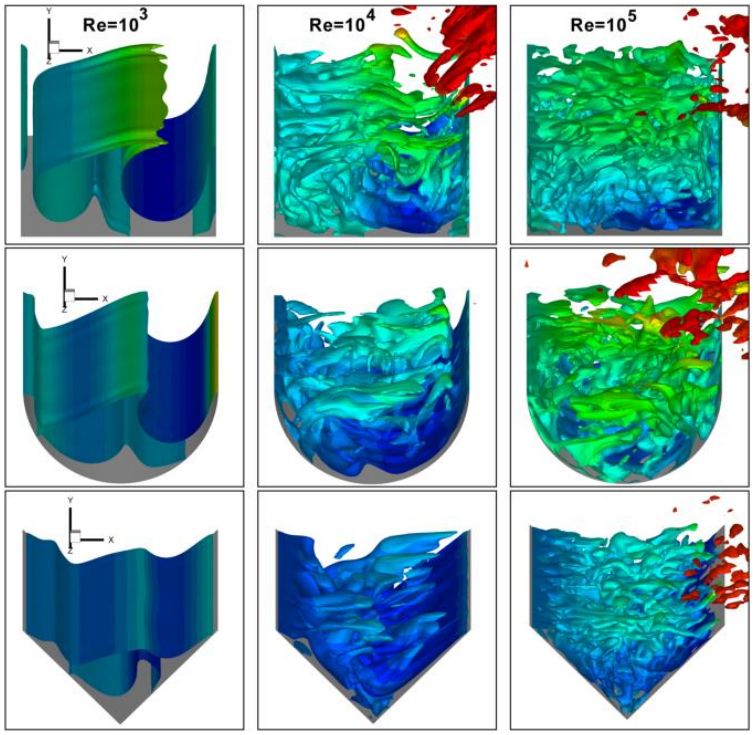

Figure 13. Instantaneous vortical structure iso-surfaces within three different cavities such as rectangular, semi-circular, and triangular cavities at (a) Re=103, (b) Re=104, (c) Re=105

CONCLUSION

Flow structures within the rectangular, semi-circular, and triangular cavities at Re=10^3, 10^4, and 10^5 is studied numerically using Large Eddy Simulation. It is observed that flow within the cavities alters as a function of the shape and the Reynolds number. At Re=10^3, flow within the cavities, except at separation points, is laminar and two-dimensional without changes of flow characteristics in the spanwise direction. In other words, at Re=10^3, some different vortical flow structures are detected within cavities in the flow direction, for example, the large scale core vortex, V_1, developing vortex, V_2, and corner vortex, V_3, within the rectangular cavity and the large scale core vortex, V_1, developing vortex, V_2, within the semi-circular and triangular cavities are developed. Once the Reynolds number increases to a value of 10^4, the semi-circular cavity affected substantially comparing to other cavities. For the high Reynolds number, Re=10^5, values of time-average static pressure and fluctuating static pressure are higher within the semi-circular cavity. In contrast, the momentum transfer and the turbulent kinetic energy are lower in comparison to the rectangular and triangular cavities.

Examination of instantaneous flow data stated that by increasing the Reynolds number the large scale eddies break into small scale eddies within all cases of cavities and flow becomes turbulent, completely. This situation increases the flow entrainment and eddy viscosity in cavities. In the continuations of the present work, namely as a future work, the following recommendations can be made. For example, investigation on the effects of cavity aspect ratio, as an effective parameter on the flow structure, on the heat and fluid flow behavior with various cavity shapes may be useful for heat exchanger applications with various types. Alternatively, applications of cavities with different shapes at very large Reynolds number, namely supersonic flow, can be recommended since they can be interested in aerodynamic applications.

ACKNOWLEDGMENTS

The authors would like to acknowledge the funding of the Research Projects Office of Cukurova University under contract No: MMF 2012D17.

REFERENCES

Chaing, T. P., Hwang, R. R., & Sheu, W. H. (1996). Finite volume analysis of spiral motion in a rectangular lid-driven cavity. International journal for numerical methods in fluids, 23(4), 325-346.

Chiang, T. P., Sheu, W. H., & Hwang, R. R. (1998). Effect of Reynolds number on the eddy structure in a lid-driven cavity. International journal for numerical methods in fluids, 26(5), 557-579.

Chiang, T. P., & Sheu, W. H. (1997). Numerical prediction of eddy structure in a shear-driven cavity. Computational Mechanics, 20(4), 379-396.

Albensoeder, S., Kuhlmann, H. C., & Rath, H. J. (2001). Multiplicity of steady two-dimensional flows in two-sided lid-driven cavities. Theoretical and Computational Fluid Dynamics, 14(4), 223-241.

Khanafer, K., & Vafai, K. (2002). Double-diffusive mixed convection in a lid-driven enclosure filled with a fluid-saturated porous medium. Numerical Heat Transfer: Part A: Applications, 42(5), 465-486.

Chen, C. L., & Cheng, C. H. (2004). Experimental and numerical study of mixed convection and flow pattern in a lid-driven arc-shape cavity. Heat and mass transfer, 41(1), 58-66.

Sun, K. H., Pyle, D. L., Baines, M. J., Hall-Taylor, N., & Fitt, A. D. (2006). Velocity profiles and frictional pressure drop for shear thinning materials in lid-driven cavities with fully developed axial flow. Chemical engineering science,61(14), 4697-4706.

Sørensen, J. N., Naumov, I., & Mikkelsen, R. (2006). Experimental investigation of three-dimensional flow instabilities in a rotating lid-driven cavity. Experiments in fluids, 41(3), 425-440.

Bouffanais, R., Deville, M. O., Fischer, P. F., Leriche, E., & Weill, D. (2006). Large-eddy simulation of the lid-driven cubic cavity flow by the spectral element method. Journal of Scientific Computing, 27(1), 151-162.

Noor, D. Z., Kanna, P. R., & Chern, M. J. (2009). Flow and heat transfer in a driven square cavity with double-sided oscillating lids in anti-phase.International Journal of Heat and Mass Transfer, 52(13), 3009-3023.

Mercan, H., & Atalık, K. (2009). Vortex formation in lid-driven arc-shape cavity flows at high Reynolds numbers. European Journal of Mechanics-B/Fluids,28(1), 61-71.

Oueslati, F., Beya, B. B., & Lili, T. (2011). Aspect ratio effects on three-dimensional incompressible flow in a two-sided non-facing lid-driven parallelepiped cavity. Comptes Rendus Mecanique, 339(10), 655-665.

Haque, S., Lashgari, I., Giannetti, F., & Brandt, L. (2012). Stability of fluids with shear-dependent viscosity in the lid-driven cavity. Journal of Non-Newtonian Fluid Mechanics, 173, 49-61.

Manca, O., Nardini, S., & Vafai, K. (2006). Experimental investigation of mixed convection in a channel with an open cavity. Experimental heat transfer, 19(1), 53-68.

Rauwoens, P., Vierendeels, J., & Merci, B. (2008). Numerical study of the flow in a three-dimensional thermally driven cavity. Journal of Computational and Applied Mathematics, 215(2), 538-546.

John, B., Gu, X. J., & Emerson, D. R. (2010). Investigation of heat and mass transfer in a lid-driven cavity under nonequilibrium flow conditions. Numerical Heat Transfer, Part B: Fundamentals, 58(5), 287-303.

Dos Santos, E. D., Piccoli, G. L., França, F. H. R., & Petry, A. P. (2011). Analysis of mixed convection in transient laminar and turbulent flows in driven cavities. International Journal of Heat and Mass Transfer, 54(21), 4585-4595.

Ozalp, C., Pinarbasi, A., & Sahin, B. (2010). Experimental measurement of flow past cavities of different shapes. Experimental Thermal and Fluid Science,34(5), 505-515.

Saqr, K. M., Aly, H. S., Kassem, H. I., Sies, M. M., & Wahid, M. A. (2010). Computations of shear driven vortex flow in a cylindrical cavity using a modified k-ε turbulence model. International Communications in Heat and Mass Transfer, 37(8), 1072-1077.

Saqr, K. M., Aly, H. S., Kassem, H. I., Sies, M. M., & Wahid, M. A. (2010, July). Large Eddy Simulation of shear-driven vortex flow in a cylindrical cavity. In Proceedings of the 2010 international conference on theoretical and applied mechanics, and 2010 international conference on Fluid mechanics and heat & mass transfer (pp. 84-87). World Scientific and Engineering Academy and Society (WSEAS).

Ryu, Y. H., & Baik, J. J. (2009). Flow and dispersion in an urban cubical cavity.Atmospheric Environment, 43(10), 1721-1729.

Zhang, T., Shi, B., & Chai, Z. (2010). Lattice Boltzmann simulation of lid-driven flow in trapezoidal cavities. Computers & Fluids, 39(10), 1977-1989.

Peng, S. H., & Davidson, L. (2001). Large eddy simulation for turbulent buoyant flow in a confined cavity. International Journal of Heat and Fluid Flow, 22(3), 323-331.
Perumal, D. A., & Dass, A. K. (2011). Multiplicity of steady solutions in two-dimensional lid-driven cavity flows by Lattice Boltzmann Method. Computers & Mathematics with Applications, 61(12), 3711-3721.

Chen, S., Liu, H., & Zheng, C. (2012). Numerical study of turbulent double-diffusive natural convection in a square cavity by LES-based lattice Boltzmann model. International Journal of Heat and Mass Transfer, 55(17), 4862-4870.

Lawson, S. J., & Barakos, G. N. (2011). Review of numerical simulations for high-speed, turbulent cavity flows. Progress in Aerospace Sciences, 47(3), 186-216.

Lawson, S. J., & Barakos, G. N. (2011). Review of numerical simulations for high-speed, turbulent cavity flows. Progress in Aerospace Sciences, 47(3), 186-216.

Salinas-Vazquez, M., Vicente, W., Martinez, E., & Barrios, E. (2011). Large eddy simulation of a confined square cavity with natural convection based on compressible flow equations. International Journal of Heat and Fluid Flow,32(5), 876-888.

Goncalvès, E., & Decaix, J. (2012). Wall model and mesh influence study for partial cavities. European Journal of Mechanics-B/Fluids, 31, 12-29.

Hassanzadeh, R., Sahin, B., & Ozgoren, M. (2011). Numerical investigation of flow structures around a sphere. International Journal of Computational Fluid Dynamics, 25(10), 535-545. Krajnović, S., Ringqvist, P., Nakade, K., & Basara, B. (2012). Large eddy simulation of the flow around a simplified train moving through a crosswind flow. Journal of Wind Engineering and Industrial Aerodynamics, 110, 86-99.

Smagorinsky, J. (1963). General circulation experiments with the primitive equations: I. the basic experiment*. Monthly weather review, 91(3), 99-164.

Deardorff, J. W. (1973). The use of subgrid transport equations in a three-dimensional model of atmospheric turbulence. Journal of Fluids Engineering,95(3), 429-438.

Patankar, S. (1980). Numerical heat transfer and fluid flow. CRC press.

SIMULATION OF FLOW WITHIN THE DIFFERENT CAVITIES USING SST K-Ω TURBULENCE MODEL

Nehir Tokgoz[1] , Rahim Hassanzadeh[2*], Besir Sahin[3],

[1]Department of Energy Systems Engineering, Osmaniye Korkut Ata University, Osmaniye,Turkey
[2]Department of Mechanical Engineering, Urmia University of Technology, Urmia, Iran
[3]Faculty of Engineering and Architecture, Mechanical Engineering Department, Cukurova University, Adana, Turkey
r.hassanzadeh@uut.ac.ir, nehirtokgoz@osmaniye.edu.tr, bsahin@cu.edu.tr

ABSTRACT: This work is a three-dimensional investigation about the flow structure within three different cavities such as rectangular, triangular and semi-circular shapes using computational fluid dynamics. The present study is performed based on the Reynolds numbers of 1,000. The aspect ratio of all under consideration cavities is L/D=2. In order to simulate and study the flow characteristics, SST K-ω model is combined with Navier-Stokes equations and applied on the non-uniform multi-block grid systems based on the finite volume technique. For enhanced visualization, different time-averaged and instantaneous flow patterns are presented. Within the cavities three different vortex mechanisms including of primary, developing and corner vortices are observed. Examination of instantaneous flow data revealed that the rate of unsteadiness within the rectangular cavity is higher than two other cavities. Finally, it is stated that at Re=1,000, flow is two-dimensional with respect to stream-wise and normal directions.

Keywords: Cavity, Computational Fluid Dynamics (CFD), Finite volume method, SST K-ω, Vortex flow

*Corresponding author. Tel: +98-4433980251, E-mail: r.hassanzadeh@uut.ac.ir

INTRODUCTION

The flow over cavities is of great interests due to very different applications in the science and engineering such as solar collectors, turbine blades, flow inside ribbed tubes and channels, flow over aircraft hulls, weapon bays and many other applications. In the past decade, several numerical and experimental investigations were performed on the heat and fluid flow within the cavities. In general, flow over and within the cavities may be divided into three different main groups including of lid-driven cavities (Zhang et al. [1], Povitsky [2], Oueslati et al. [3], Guermond et al. [4]), thermally-driven cavities (Vasseur [5]), and shear-driven cavities. However, some of the articles may be a combination of two or three mentioned groups

(Stefanovic and Stefan, [6]). With respect to the subject of this study, we present a history of previous works associated to shear-driven cavities. Various experimental and numerical researches were performed about the shear driven cavities. For example, Zdanski et al. [7] have numerically presented a physical analysis on the flow over cavities with large aspect ratio. They applied standard k-ε turbulence model at different Reynolds number corresponding to laminar and turbulent values. They have demonstrated that the vorticity shed at the upstream corner and stagnation region formed at the downstream vertical face has a major influence on vortices positioned inside the cavity. Saqr et al. [8] have computed the shear driven vortex flow in a cylindrical cavity using a modified k-ε turbulence model. They have compared their results with other measurements predicting the shear-driven vortex flow inside the cavity, successfully. Flow and heat transfer over rectangular shallow cavities at different aspect ratios have performed by Mesalhy et al. [9] using standard k-ε turbulence model. It has been demonstrated that based on the value of the cavity aspect ratio, the type of cavity flow changes from open cavity flow to close cavity flow. They also found that the critical aspect ratio at which this change occured was seven, approximately. On the other hand, an experimental measurement of flow past cavities of different shapes has conducted by Ozalp et al. [10]. In their research, three different cavity shapes including of rectangular, triangular, and semi-circular cavities were under consideration at three Reynolds numbers of 1230, 1460 and 1700. Their results have revealed that in addition to cavity shapes, changing of Reynolds number has some degree of influence on the structure of flow and turbulence quantities. They also have stated that maximum Reynolds stress and turbulence intensity values were observed in the lid section of the cavity at the centerline position and rectangular and triangular cavities cause much greater turbulence compared to the semi-circular cavity shape.

Most of investigations in open literature associated to square and/or rectangular cavities while there are many various applications in which the non-rectangular cavities such as triangular and semi-circular are used. This study is focused on the flow structure within the three different cavities such as rectangular, triangular, and semi-circular shapes using shear stress transport (SST) k-ω turbulence model. It is assumed that the length of cavities is infinite with respect to the spanwise direction. In the past decade, different numerical methods were used for simulation and solution of flow within the cavities (Ho and Lin [11], Wei et al. [12], Gupta and Kalita [13], Peng and Davidson [14], Zdanski et al. [7], Diang et al. [15]). For this reason, the validity of this turbulence model during the present case study is under consideration.

FLOW DOMAIN AND BOUNDARY CONDITIONS

In the present three-dimensional study, three different cavity shapes such as rectangular, triangular, and semi-circular cavities are under the consideration. The aspect ratios (ratio of the cavity length, L, to the cavity depth, D,) are identical and equal to 2.0. Figure 1 shows the details of the flow domain dimensions and the

applied grid systems. For simulation of flow structure a computational domain with dimensions in the range of 0≤x/L≤10 in the stream-wise direction, -1≤y/L≤1 in the normal direction and -0.5≤z/L≤2 in the span-wise direction were used. The value of the Reynolds number with respect to the cavity depth and free-stream velocity is 1,000 corresponding to inlet velocity of 0.02 m/s. In order to compute the flow data, the multi-block grid system was constructed on the flow domain. For performing this construction, firstly the flow domain was divided into different blocks. After that, different grid sizes were applied on the blocks in which the finer grids are associated to the regions inside the cavities and coarse grids are associated far from the cavities (free-stream flow). The total number of control volumes is indicated in table 1.

Table 1: Details of total grids used in the present study

	Number of control volumes	Minimum grid size*
Rectangular cavity	695,700	0.006D
Triangular cavity	654,450	0.006D
Semi-circular cavity	1,096,788	0.006D

* D is the cavity depth

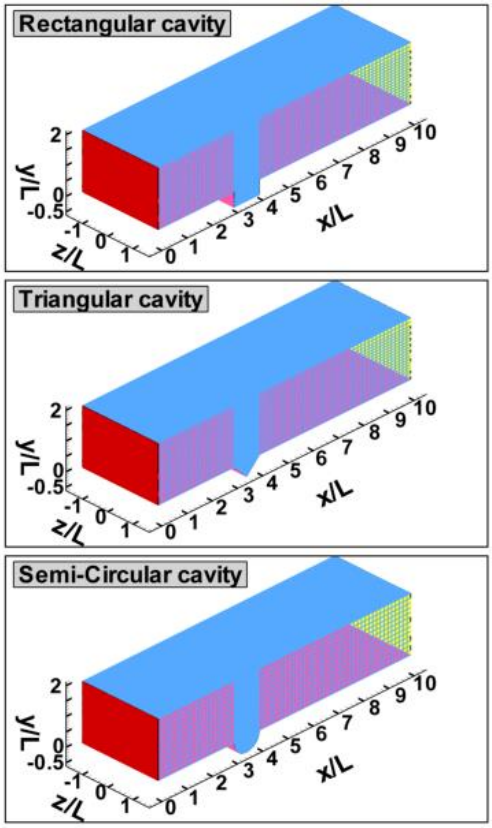

Figure 14. Details of Flow Domain And Applied Multi-Grids Topology

GOVERNING EQUATIONS AND NUMERICAL METHOD

Conservation of mass and momentum

The governing equations for incompressible and Newtonian fluid used in this study are summarized as following:
Conservation of mass:

$$\frac{\partial u_i}{\partial x_i} = 0 \tag{1}$$

Conservation of momentum:

$$\frac{\partial u_i}{\partial t} + \frac{\partial}{\partial x_j}\left(u_i u_j\right) = -\frac{1}{\rho}\frac{\partial p}{\partial x_i} + \nu \frac{\partial u_i}{\partial x_j \partial x_j} \tag{2}$$

where x_i=(x, y, z), u_i=(u, v, w), p and t are the coordinate space, velocity, pressure and time, respectively.

The shear stress transport (SST) k-ω turbulence model; an overview

The CFD model used in the present work is the Reynolds-averaged Navier-Stokes equations (RANS) model according to shear stress transport (SST) k-ω turbulence closure model developed by Menter [16]. The SST k-ω model is similar to the standard k-ω model, but includes three refinements. These refinements are; i-) This model incorporates a damped cross-diffusion derivative term in the ω equation, ii-) The definition of the turbulent viscosity is modified to account the transport of the turbulent shear stress and iii-) The model constants are different. There is no need for a special treatment for the viscosity affected wall region because of the low-Reynolds correction in the k-ω and k-ω SST models. The transport equations for k and ω may be written as (Dewan [17]):

$$\frac{\partial k}{\partial t} + \bar{u}_j \frac{\partial k}{\partial x_j} = \frac{\partial}{\partial x_j}\left[\left(\nu + \sigma_k \nu_t\right)\frac{\partial k}{\partial x_j}\right] + P_k - \beta^* k\omega \tag{3}$$

$$\frac{\partial \omega}{\partial t} + \bar{u}_j \frac{\partial \omega}{\partial x_j} = \frac{\gamma P_k}{\rho \nu_t} - \beta\omega^2 + \frac{\partial}{\partial x_j}\left[\left(\nu + \sigma_{\omega 2}\nu_t\right)\frac{\partial \omega}{\partial x_j}\right] + 2\left(1 - F_1\right)\sigma_{\omega 2}\frac{1}{\omega}\frac{\partial k}{\partial x_j}\frac{\partial \omega}{\partial x_j} \tag{4}$$

The eddy viscosity is written as (Dewan [17]):

$$\nu_t = \frac{a_1 k}{\max\left(a_1\omega, SF_2\right)} \tag{5}$$

The auxiliary relations and the model constant can be written as (Dewan [17]):

$$F_1 = \tanh\left(\left\{\min\left[\max\left(\frac{\sqrt{k}}{\beta^*\omega y}, \frac{500\nu}{y^2\omega}\right), \frac{4\sigma_{\omega 2}k}{CD_{k\omega}y^2}\right]\right\}^4\right) \tag{6}$$

$$F_2 = \tanh\left(\max\left(\frac{2\sqrt{k}}{\beta^*\omega y}, \frac{500\nu}{y^2\omega}\right)^2\right) \tag{7}$$

$$P_k = \min\left(\tau_{ij}\frac{\partial \bar{u}_i}{\partial x_j}, 10\beta^* k\omega\right) \tag{8}$$

$$CD_{k\omega} = \max\left(2\rho\sigma_{\omega 2}\frac{1}{\omega}\frac{\partial k}{\partial x_i}\frac{\partial \omega}{\partial x_i}, 10^{-20}\right) \tag{9}$$

The constants for example Φ are blended using the relation (Dewan [17]):

$$\phi = \phi_1 F_1 + \phi_2 (1 - F_1) \tag{10}$$

$$\gamma_1 = \frac{\beta_1}{\beta^*} - \frac{\sigma_{\omega 1} k^2}{\sqrt{\beta^*}}, \qquad \gamma_1 = \frac{\beta_2}{\beta^*} - \frac{\sigma_{\omega 2} k^2}{\sqrt{\beta^*}}$$
$$\beta_1 = 3/40, \quad \beta_2 = 0.0828, \quad \beta^* = 9/100, \quad \sigma_{k1} = 0.85, \quad \sigma_{k2} = 1 \tag{11}$$
$$a_1 = 0.31, \quad \sigma_{\omega 1} = 0.5, \quad \sigma_{\omega 2} = 0.856$$

Solution procedure

A three-dimensional finite volume code was applied to discrete the 3D flow domain through a second order scheme. In order to discrete the convective terms, QUICK scheme was applied. Moreover, the SIMPLE algorithm was used to achieve the mass conservation between the pressure and velocity terms in the discretized momentum equation. On the other hand, for discretization of time a second order implicit method was employed. For inlet section and lower wall Dirichlet boundary conditions were applied while for outlet section as well as upper and side walls the Neumann boundary conditions were employed. Applications of symmetric conditions on the side walls indicate the infinite cavity size in the span-wise direction. In order to study the grid size independency of results different grid numbers were used ranging from 95,058, 90,987 and 89,792 for rectangular, triangular and semi-circular cavities, respectively to the final control volume numbers indicated in the table 1 and it was observed that results did not change using the final control volumes indicated in table 1. The non-dimensional physical time step during the solution was 0.004 D/U_∞ in which D and U_∞ are the cavity depth and free-stream velocity (which is equal to inlet velocity), respectively. Independency of the results regarding the time step size was also under consideration. For this reason, three different physical time steps were applied for solution including of 0.04 D/U_∞, 0.008 D/U_∞ and 0.004 D/U_∞ while the value of stream-wise velocity, u, inside the shear layer within the cavities was under consideration. It should be noted that the independency of results from grid size as well as time step was studied for each cavities, distinctly. The grid size and time step independency studies revealed rather slight differences for stream-wise velocity values. Thus, the last grid sizes (indicated in the table 1) and time step of 0.004 D/U_∞ were adopted during the present study. The convergence of the numerical 3D velocity field was established by controlling the residuals by setting its variation less than 10^{-7}. Each time steps are consisted of at least 20 time intervals and totally 3,000 time steps (60,000 iterations) are performed during the solution.

RESULTS AND DISCUSSION

Time-averaged flow patterns within the cavities

Figure 2 illustrates time-averaged streamlines, $\langle\psi\rangle$, patterns and velocity vector, $\langle V\rangle$, colored with time-averaged stream-wise velocity values within the cavities at

Re=1,000. For each cavity such as rectangular, triangular and semi-circular shapes, three different vortical structures are developed. Firstly, primary large-scale vortex (V1) is concentrated in the upper side between the upstream and downstream walls of the cavities. Secondly, a developing vortex (V2) is developed upstream side of primary vortex. Thirdly, a small corner vortex (V3) is concentrated very close to the downstream wall of cavities. Developing of the primary and developing vortices is due to flow separation from the tip of cavity. For all three shapes, the primary large-scale vortex (V1) occupied the whole upper side of the cavity. A similar result for primary large scale have reported in the experimental study of Ozlap et al. [10]. Comparison between the images of the Figure 2 reveals that due to higher rate of fluid entrainment in the region near the upstream cavity wall, the developing vortex (V2) is larger for rectangular shape, relatively. However, some investigations such as Luo et al.[18] have stated that for very large Reynolds number (supersonic flow) the developing vortex disappears for all three cavity shapes. Further examination of the Figure 2 indicates that a corner vortex (V3) is developed for different cavity shapes under consideration in this study. This corner vortex (V3) is developed at the vicinity of downstream and lower walls of rectangular cavity while for triangular cavity this corner vortex is concentrated on the lower side of the primary vortex and very close to the developing vortex. On the other hand, the results revealed no significant corner vortex (V3) for semi-circular cavity in comparison to the other cases. Despite the fact that the concentration of secondary and corner vortices may increase the heat transfer rate within the cavity, they will impose more drag on the fluid flow.

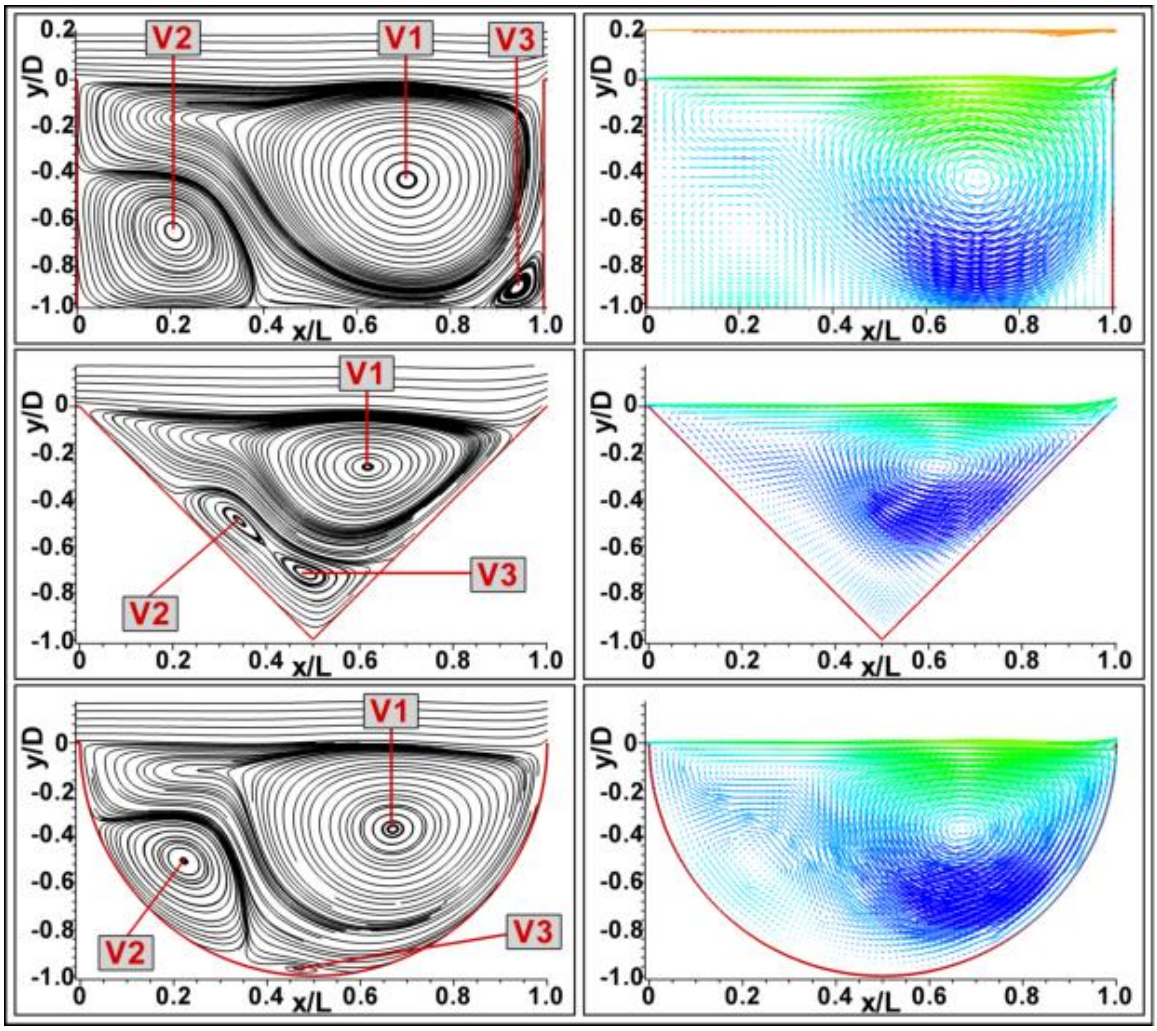

Figure 15. Time-averaged streamlines, <ψ>, patterns and velocity vector, <v>, colored with time-averaged streamwise velocity

Distributions of time-averaged stream-wise and normal velocity components, $\langle u/U_\infty \rangle$ and $\langle v/U_\infty \rangle$, are shown on the left and right hand sides of Figure 3, respectively. The values of the images in Figure 3 are normalized by free-stream velocity value as a reference velocity. It should be noted that the dashed lines indicate the negative velocity values. It can be seen clearly that a maximum negative packet of stream-wise velocity is developed for all cavity shapes. The center of mentioned pocket is approached to the downstream wall for all shapes indicating the higher rate of momentum transfer at those points in the opposite direction of free-stream motion. Comparison of the images located on the left hand side also reveals that the values of negative stream-wise velocity, $\langle u/U_\infty \rangle$, are higher for rectangular, semi-circular and triangular cavities, respectively stating the lower stream-wise fluctuating velocity within the triangular cavity. On the other hand, examination of time-averaged normal velocity, $\langle v/U_\infty \rangle$, images located at the right hand side of Figure 3 demonstrates that for all cases a pair of maximum values is concentrated within the cavity. The maximum positive part is developed at the center of cavity while the maximum negative part is approached to downstream side of the cavity. Like as the stream-wise velocity distributions, the maximum positive and negative values of normal velocity, $\langle v/U_\infty \rangle$, are higher for rectangular, semi-circular and

triangular cavities, respectively indicating the lower normal fluctuating velocity concentration for triangular cavity.

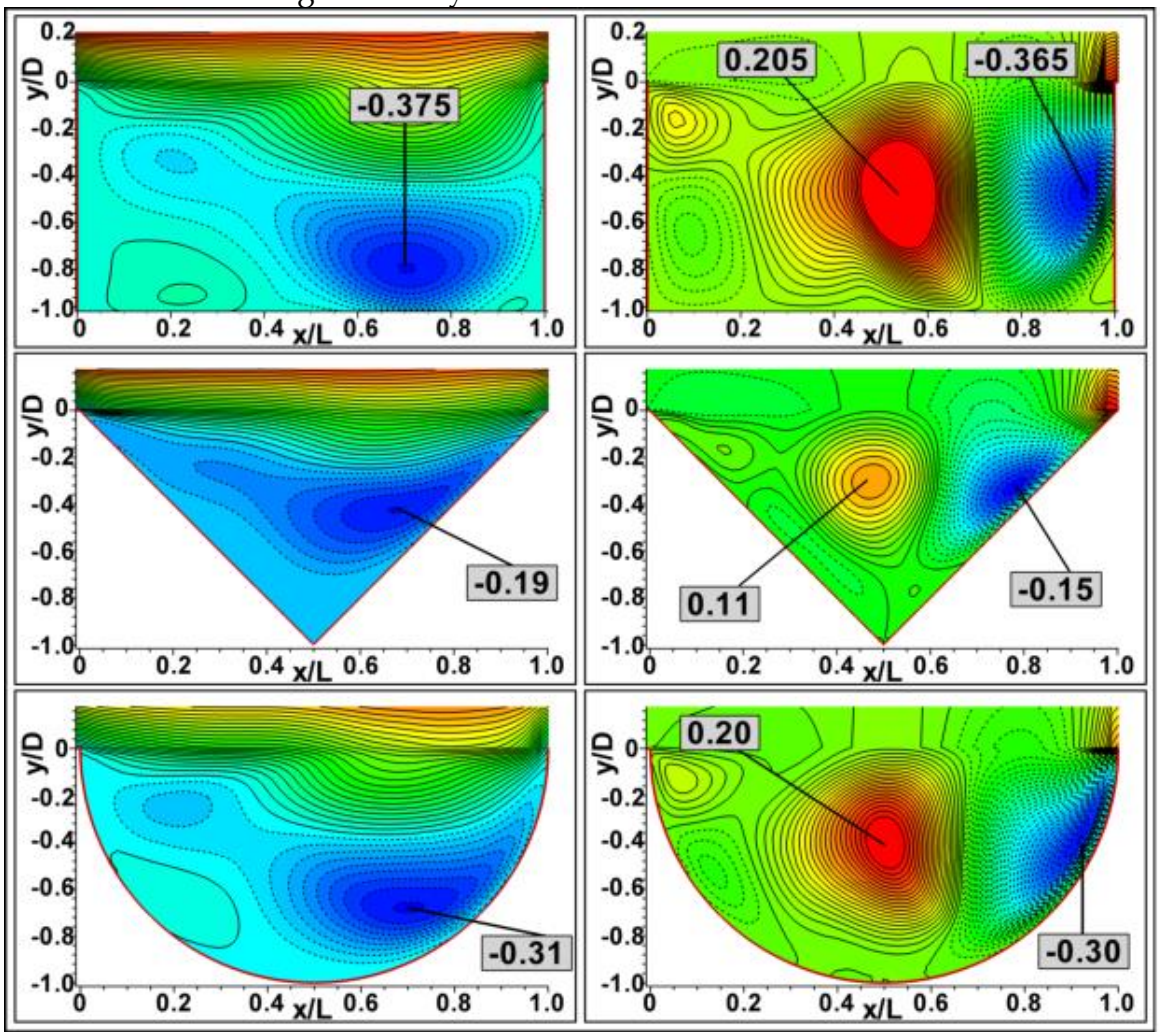

Figure 16. Distributions of time-averaged streamwise velocity component, <u/u∞> (left hand side, <δu/u∞>=0.035) and time-averaged normal velocity component, <v/u∞> (right hand side, <δv/u∞>=0.01)

In order to understand the velocity distribution within the cavities in detail, variation of stream-wise and normal velocities at different locations within the cavities are plotted in Figures 4 and 5, respectively according to the top image of Figure 4 in which the "S" is measured from the tip of cavity and "L" is the cavity length. Here, the upper row, middle row and lower row are associated with rectangular, triangular and semi-circular cavities, respectively in both Figures 4 and 5. According to the images of Figure 4 at the location of S/L=0.2, the stream-wise velocity gradient for rectangular and semi-circular cavities is higher in comparison to the triangular cavity. It is due to passing of this location across the developing vortex (V2) which rotates counter-clockwise and after that across the primary vortex (V1) which rotates clockwise for rectangular and semi-circular cavities. On the other hand, this location is completely cited inside the primary vortex (V1) for triangular case. Due to this fact, the demonstration of developing vortex (V2) for rectangular and semi-circular cavities is more significant relatively to the triangular cavity with respect to its size and effect level. At S/L=0.4, due to passing of this location from the boundary of

primary and developing vortices (V1,V2) for all three cavities, the variations of stream-wise velocity are similar for all cases. Furthermore, at the locations of S/L=0.6 and 0.8, due to passing of this location across center of the negative stream-wise velocity pocket, as indicated in the left hand side images of Figure 3, the velocity gradients are high for all cases. However, this variation is relatively low for triangular cavity.

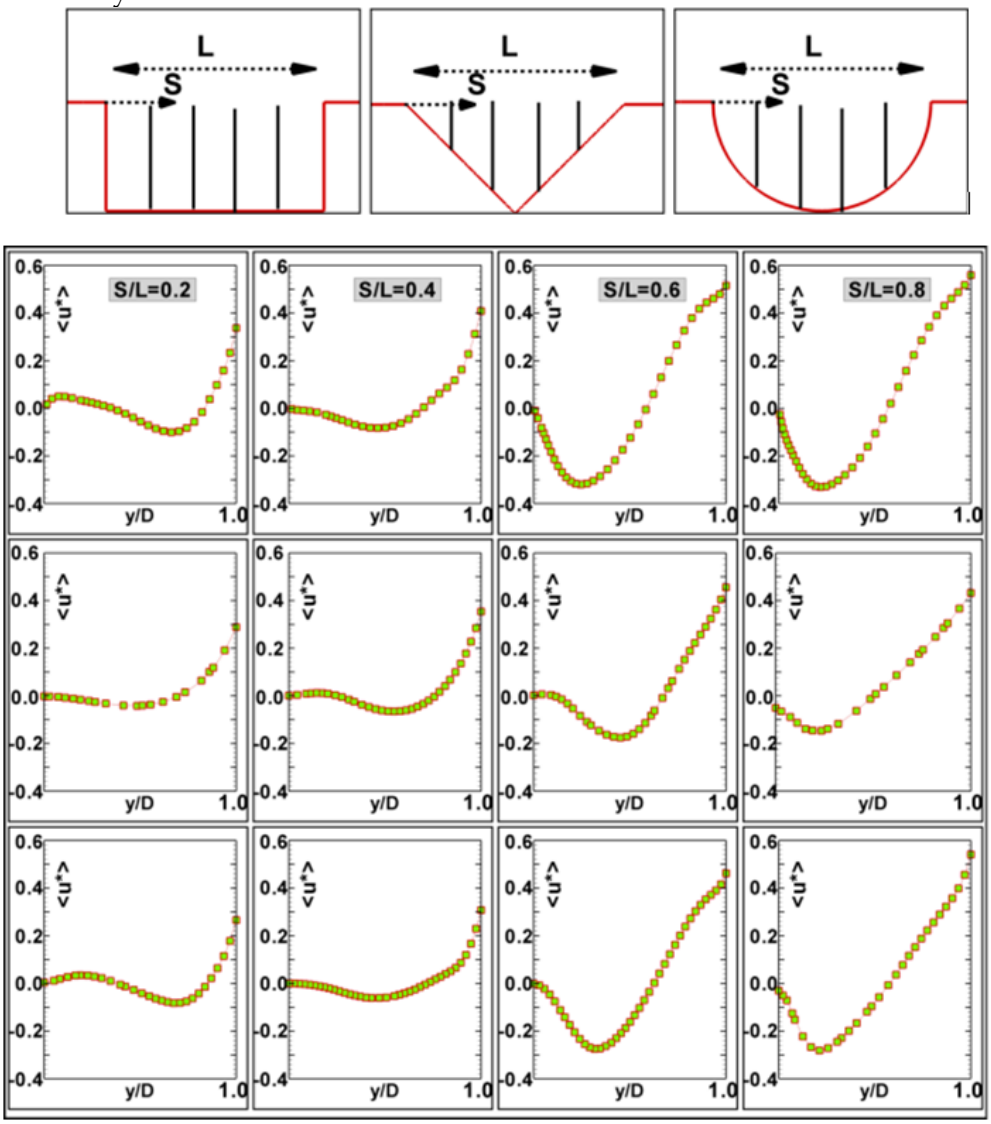

Figure 17. Variations of time-averaged streamwise velocity, <u*>= <u/u∞> at different vertical location such as s/l=0.2, 0.4, 0.6 and 0.8 inside the cavities according to the top image (first row: rectangular cavity, second row: triangular cavity, third row: semi-circular cavity)

Comparison of normal velocity, <v/U∞>, variations for three different cavities at the location of S/L=0.2 indicates no significant variations. However, at S/L=0.4 the variation of normal velocity, <v/U∞>, increases for all cavity shapes. It is due to passing of this location across the closed region to the maximum positive normal velocity zone as indicated in the right hand side images of Figure 3. At S/L=0.6, the normal velocity variation is higher and completely positive for rectangular and semi-circular cavities while there is no significant variation for triangular cavity due

to passing across boundary of the maximum positive and maximum negative zones for the triangular case. Finally, due to passing across the closed region to the maximum negative zone of normal velocity, $\langle v/U_\infty \rangle$, at S/L=0.8 the higher negative velocity variations are demonstrated for all cases.

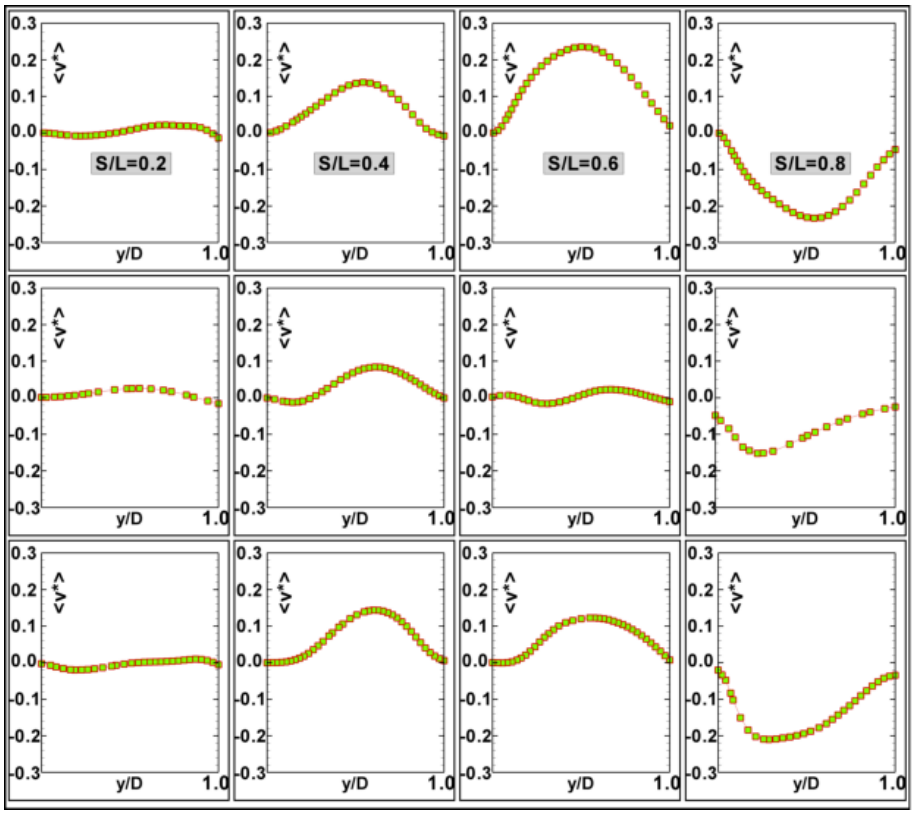

Figure 18. Variations of time-averaged normal velocity, $\langle v^* \rangle = \langle v/U_\infty \rangle$, at different vertical location such as S/L=0.2, 0.4, 0.6 and 0.8 inside the cavities according to the top image of Fig. 4 (first row: rectangular cavity, second row: triangular cavity, third row: semi-circular cavity)

One of the encountered problem about the flow within cavities is the imposed drag on the fluid motion by cavities. At the end of this subsection, we will consider the static pressure distribution within the three different cavities. Figure 6 demonstrates time-averaged non-dimensional pressure, $\langle P_s/0.5\rho U^2_\infty \rangle$, within all cases of cavity in which the P_s is the dimensionless static pressure that has been scaled by dynamic pressure, $0.5\rho U^2_\infty$. Examination of the indicated images reveals that for each case a pair of maximum and minimum pressure is developed between the center of cavity and its downstream wall for all cases. The maximum positive pressure zone is very close to the trail of cavities. The significant appearance of the positive pressure is due to separation of flow at the trailing edge of cavities as well as the large difference between the velocities of free-stream and within the cavities. Upstream of the positive zone, the maximum negative zone of pressure is developed for all cavity shapes. The concentrated negative pressure zone is more significant than its positive zone. This negative zone is the main cause for drag imposing. Further examination reveals that the value of maximum negative pressure for triangular cavity is less than the other cases which indicates the less drag imposing on the flow. After the

triangular cavity, semi-circular cavity has lower value of maximum negative pressure in comparison to rectangular cavity.

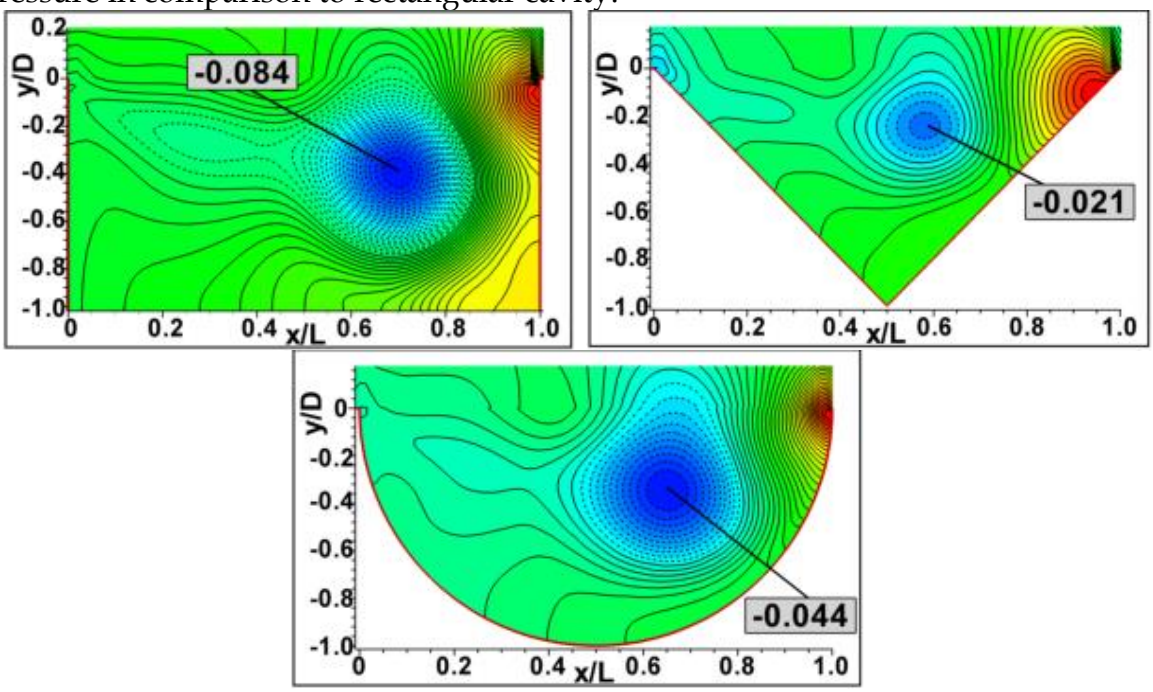

Figure 19. Distributions of time-averaged non-dimensional static pressure, $<p_s/0.5\rho u^2_\infty>$ ($<\delta p_s/0.5\rho u^2_\infty>$=0.004)

Instantaneous flow patterns within the cavities

It is known that time-averaged flow data do not provide the details of flow behavior. For this reason, one can study and analyze the flow characteristics by instantaneous flow data. We have provided the instantaneous flow patterns in Figure 7 in order to reveal the flow behavior in details.

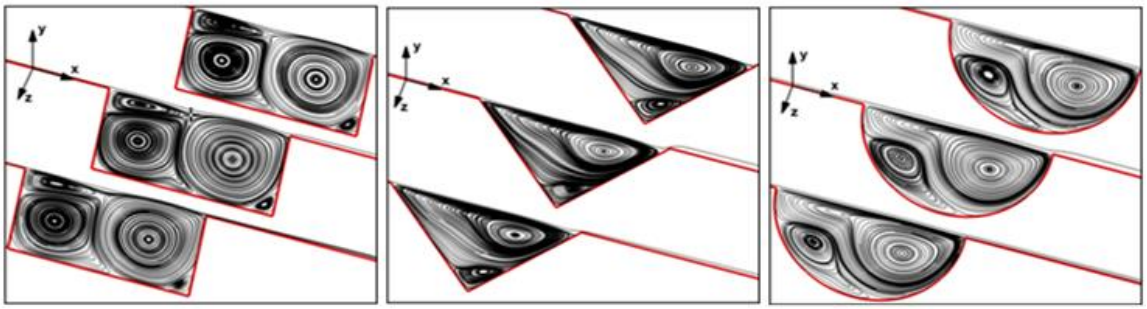

Figure 20. Instantaneous streamlines, ψ, patterns at three different spanwise sections

This Figure illustrates the instantaneous streamlines, ψ, patterns at three different span-wise sections at the same time. Explanation of images of Figure 7 may be provided at two following steps:

Examination of the images of Figure 7 states that within the rectangular cavity the developing vortex (V2) gradually becomes larger for a certain period of time. This periodic appearance reveals a similar time-averaged pattern indicated in the first image of Figure 2. However, the existing of corner vortex (V3) is fixed. Within the triangular cavity, the developing vortex (V2) disappears time to time and forces the

corner vortex (V3) to approach to the downstream wall. On the other hand, flow behavior within the circular cavity does not change significantly. Further examination of flow behavior by numerical animation indicates that the rate of unsteadiness within the cavity at Re=1,000 is low for semi-circular, triangular and rectangular cavities, respectively. However, the rate of this unsteadiness may be changed by varying the Reynolds number or aspect ratio of cavities.
Examination of flow patterns within the three span-wise section states that due to the same flow pattern at different span-wise direction and unchanged flow data, flow is completely two-dimensional. In another words, flow characteristics change in stream-wise and normal directions and they do not change in the span-wise direction. It is because of long length of cavities in the span-wise direction, symmetrical boundary conditions assumption for sides of cavity and relatively lower Reynolds number.

CONCLUSION

Numerical computations of shear driven vortex flow within the three different cavities such as rectangular, triangular and semi-circular shapes were investigated using SST k-ω turbulence model at Re=1,000. Examination of time-averaged flow patterns revealed that three different vortex mechanisms dominate for all under consideration cavities. The primary vortex (V1) which is the larger one dominates between the upstream and downstream walls of cavities. Secondary or developing vortex (V2) is developed in the upstream side of the primary vortex at the region very close to the upstream wall of cavities. Finally, a small corner vortex (V3) is developed at the vicinity of downstream and lower wall of cavities. It is found that rate of unsteadiness within the rectangular cavity is more than triangular and semi-circular cavities. Furthermore, rectangular cavity imposes more drag on the fluid motion. On the other hand, using of SST k-ω turbulence model satisfies the previous results that have used the other turbulence models. Finally, it is obtained that flow within the rectangular, triangular and semi-circular cavities with infinite length in span-wise direction, is two-dimensional in stream-wise and normal directions at Re=1,000.

ACKNOWLEDGMENTS

The authors would like to acknowledge the funding of the Research Projects Office of Cukurova University under contract No: MMF 2012D17.

REFERENCES

Zhang, T., Shi, B., Chai, Z.: Lattice Boltzmann simulation of lid-driven flow in trapezoidal cavities. J. Computers and Fluids. 39, 1977-1989 (2010).

Povitsky, A.: Three-dimensional flow in cavity at yaw. J. Nonlinear Analysis. 63, 1573-1584, 2005.

Oueslati, F., Ben Beya, B., Lili, T.: Aspect ratio effects on three-dimensional incompressible flow in a two-sided non-facing lid-driven parallelepiped cavity. J. Comptes Rendus Mecanique. 339, 655-665, 2011.

Guermond, J.L., Migeon, C., Pineau, G., Quartapelle, L.: Start-up flows in a three-dimensional rectangular driven cavity of aspect ratio 1:1:2 at Re = 1000. J. Fluid Mechanics. 450: 169-199, 2002.
Vasseur, P., Robillard, L., Anochiravani, I.: Natural convection in a shallow porous cavity heated from the side with a uniform heat flux. J. Chemical Engineering Communications. 46: 129-146, 1986.

Stefanovic, D.L., Stefan, H.G.: Simulation of transient cavity flows driven by buoyancy and shear. J. of Hydraulic research. 38, 181-195, 2011.

Zdanski, P.S.B., Ortega, M.A., Fico Jr, N.G.C.R.: On the flow over cavities of large aspect ratio: A physical analysis. J. International Communications in Heat and Mass Transfer. 33, 458- 466, 2006.

Saqr, K.M., Aly, H.S., Kassem, H.I., Mohsin, M.S., Wahid, M.A.: Computational of shear driven vortex flow in a cylindrical cavity using a modified k-ε turbulent model. J. International Communications in Heat and Mass Transfer. 37, 1072-1077, 2010.

Mesalhy, O.M., Abdel Aziz, S.S., El-Sayed, M.: Flow and heat transfer over shallow cavities. J. Thermal Science. 49, 514- 521, 2010.

Ozalp, C., Pinarbasi, A., Sahin, B.: Experimental measurement of flow past cvities of different shapes. J. Experimental Thermal and Fluid Science. 34, 505- 515, 2010.

Ho, C.J., Lin, F.H.: Numerical simulation of three-dimensional incompressible flow by a new formulation. Int. J. for Numerical Methods in Fluids. 23, 1073–1084, 1996.

Wei, J.J., Yu, B., Tao, W.Q., Kawaguchi, Y., Wang, H.S.: A new high-order-accurate and bounded scheme for incompressible flow. Numerical Heat Transfer, Part B: Fundamentals. 43, 19–41, 2003.

Gupta, M.M., Kalita, J.C.: New paradigm continued: further computations with streamfunction-velocity formulations for solving Navier–Stokes equations. Communications in Applied Analysis. 10, 461–490, 2006.

Peng, S.H., Davidson,L.: Large eddy simulation for turbulent buoyant flow in a confined cavity. Int. J. Heat and Fluid Flow. 22, 323-331, 2001.

Diang, H., Shu, C., Yeo, K.S., Xu, D.: Numerical computation of three-dimensional ncompressible viscous flows in the primitive variable form by local multiquadric differential quadrature method. Computer Methods in Applied Mechanics and Engineering. 195, 516–533, 2006.

Menter, F.R.: Two-Equation Eddy-Viscosity Turbulence Models for Engineering Applications. AIAA Journal. 32, 1598-1605,1994.

Dewan, A.: Tackling Turbulent Flows in Engineering. Springer, Verlag Berlin Heidelberg, 2011.

Luo, S.B., Huang, W., Liu, J. Wang, Z.G.: Drag force investigation of cavities with different geometric configurations in supersonic flow. Science China Technological Science. 54(5), 1345-1350, 2011.